Diss. ETH No. 18978, 2010

Cells and Currents

A dissertation submitted to the
SWISS FEDERAL INSTITUTE OF TECHNOLOGY
ZURICH

for the degree of
Doctor of Sciences

presented by
MICHAEL GABI
Dipl. Werkstoff-Ing. ETH
born July 1, 1976
citizen of Niederbipp BE

accepted on the recommendation of
Prof. Dr. Janos Vörös, examiner
Prof. Dr. Simon Philipp Hoerstrup, co-examiner
Dr. Petra Schulte, co-examiner

2010

A day without sunshine
is like a meal without wine

Acknowledgements

First of all, I would like to thank the people who have contributed to my work and helped me to realize this thesis over the last years. Most of all I would like express my sincere gratitude to my supervisor Prof. Dr. Vörös. Thank you Janos for giving me the opportunity, the trust in me and the research freedom to achieve my goals. Not many PhD students have the chance to work in such a stimulating environment. I would also like to thank, Prof. Dr. Simon. P. Hoerstrup and Dr. Petra Schulte that to be part of my board of co-referees and the time to review this thesis.

Thanks to Michael Bullen, Dr. Irina Agarkova, Dr. Dörthe Schmidt for his fruitful collaboration with the *in vivo* studies, as well to Prof. Brigitte Von Rechenberg, Katarina Kempf, Dr. Monika Hilbe from the University of Zürich, Switzerland for their help with the rat histology. Thanks to Prof. Paul Rouxhet, Universite Catholique de Louvain, Belgium for the fruitful discussions on proton diffusion in Barcelona.It has been pleasure to supervise the students Manjunath Puttaswamy, Alexandre Larmagnac and Danijela Lukic who all contributed successfully to at least one publication on their project(s). Thanks to my colleagues Dr. Takumi Sannomiya for diffusion modelling and many interesting but luckless fishing hours at the lake of Zürich. Thanks to Orane Guillaume-Gentil for the help with the OWLS measurement and countless outdoor discussions. Thanks to Raphael Zahn for the QCM-D modelling. Many permanent ETH employees helped me to realize the experiments with their expertise and friendly support, therefore many thanks to our technical staff Martin Lanz, Stephen Wheeler, Paul Lüthi, Aldo Rossi, Claudio Maccio and our always helpful secretary Esther Singer.

Thanks to all the members of the LBB for creating such a nice environment to work and giving support whenever needed.

Special thanks to Dr. Tomaso Zambelli the co-inventor of the FluidFM technology in les Diablerets, Switzerland 2006. He was then the driving force for the FluidFM research and it has been always a pleasure to work with him and being around his cheering personality. Thanks to Pascal Behr for his contributions to our research, the time spent on the template of this thesis and taking the risk to found Cytosurge with me. I really enjoyed to work with my old friend Dr.med. Lukas Hefermehl and his assistant medical doctor Dr.med. Daniel Eberli on the electrical catheter project.

Herzlichen Dank an meine Eltern Maja und Andreas, sowie meinen Grosseltern Marta und Peter für ihre Unterstützung während meines Studiums.

Un grazie particolare a Silvia che mi ha supportato per tutto il tempo e che mi ha reso una persona migliore. Grazie mille ad Aldo, Oriana e Nona che mi hanno trattato come un figlio e per tutte le esperienze che ho potuto vivere in Italia .

Abstract

In the late 18th century, Luigi Galvani presented his experiments with frog legs and the newly observed form of electricity in animals. It took almost one and a half centuries until researchers began to understand how cells generate and transmit electric potentials, starting the phase of modern electrophysiological research. This discovery, and further technical developments, led to the use of electric currents in everyday clinical therapeutics; for example pacemakers, which drastically improved quality of life and life expectation of patients with cardiac problems. Scientists and engineers dream of compensating disabilities with prostheses that are directly linked to the brain, allowing feedback signals to be sent back to the brain (e.g. position of an arm prosthesis, temperature or weight of a grabbed object). The same technology could be used to reconnect broken nerve connections with an electric circuit and regain normal functionality of paralyzed limbs or organs. Moreover, brain functions could be realized on a chip, or another sense could be added to our five existing physiological perception possibilities (sight, sound, taste, smell and touch). All the science-fiction approaches we can imagine are in principle the same - they connect an electric circuit with living cells through an interface of dead and living matter. Thereby the implanted, non-degradable material provokes a foreign body reaction, leading to encapsulation by connective tissue and loss of implant functionality. If the interface also acts as an electrode for electrical cell stimulation, the applied currents induce electrochemical reactions, which create locally unfavorable conditions for the resident living cells. In this thesis, we focus on the effects of applying currents through electrodes to cells *in vitro* and *in vivo*, and we present ways to use such electric currents to control the adhesion, growth and migration of cells on electrodes.

In chapter 4, we present a high-resolution optical method to measure the pH change due to electrochemical reactions close to an ITO electrode using confocal laser scanning microscopy. This technique further allowed us to study and model pH changes in physiological solutions, where the extent of the effect is within the hundred micrometer range. Based on the predictions of our model, we were able to connect the electrochemically-induced pH changes with the observed behavior of cultured myoblasts directly grown on the electrode surface. Current densities above a certain threshold led to the uptake of a membrane impermeable dye, indicating membrane pore formation. Cells showed exactly the same effect upon exposure to low pH solutions. Based on our model, we could attribute this to the change in local pH, although we could not exclude the effects of other electrochemically created reactive molecules.

We developed a neurochip to control the adhesion and outgrowth of individual neurons by electrochemically removing protein-repellant molecules from transparent electrodes in chapter 5. The neurochip architecture is based on three parallel

indium-tin-oxide (ITO) electrodes on a SiO_2 substrate. A photoresist structure forms a landing spot for the neuron soma and two lateral outgrowth pathways for the neurites. The whole surface was turned protein and cell repellant with PLL-*g*-PEG before enabling neuron soma adhesion by selective PLL-*g*-PEG removal. After the neuron adhered, a potential was applied to the pathway electrodes, permitting neurite outgrowth along the pathways formed by the SU8 structure. We also show the possibility to control cell migration with small pulsed currents. Myoblasts were seeded on a chemical pattern of cell-adhesive PLL and cell-resistant PLL-*g*-PEG. The PLL-*g*-PEG was then electrochemically removed from the electrodes to permit migration onto the cell-free electrodes. While electrodes without applied current were confluently overgrown within 24 hrs, a small pulsed current was able to inhibit cell growth on the bare ITO electrode for more than 72 hrs. With both techniques, cell adhesion, growth, and migration can be controlled dynamically after cells start to grow on the substrate. This opens new possibilities: we believe the key to control the development of neuron networks with well-defined topology, or more complex co-cultures, is the combination of passive surface modifications and active control over the surface properties at any time during the experiment.

Based on the findings of the previous chapters, we present in chapter 6 an implantable pulse generator, which we used to study the effects of small pulsed currents on the viability of rat aortic derived cells (ROAC) *in vitro*. The chosen pulsed currents were large enough to inhibit normal cell adhesion on the active platinum surface. The cells only formed a small adhesion patch on the active surface, while keeping their globular shape, and underwent apoptosis within 24 hrs, as indicated by the positive staining for cleaved caspase-3. Inspired by these findings, we studied the effect of these currents *in vivo*, by implanting the pulse generator subcutaneously in a rat model. Although the electrode|tissue interface histology revealed no difference between the active platinum surface and the neighboring control surface, we have found a large impedance difference at high frequencies between electrodes that remained functional during the entire experiment and the ones that stopped working due to a broken connection with the function generator. 21 days after implantation, the non-working electrodes showed an increase in impedance at higher frequencies, whereas the working electrodes maintained the same impedance the entire time. This indicates that applied currents can indeed reduce the impedance of implanted electrodes and suggests an altered encapsulation process.

In the form of a feasibility study in chapter 7, we present a novel approach to prevent bacterial adhesion, colonization and encrustation of Foley catheters and urethral stent surfaces. *Proteus mirabilis* was chosen as a model for the most common bacteria to colonize such surfaces. Minutes after inserting a catheter, deposition of host urinary components starts on the catheter surface and leads to the formation of a conditioning film. Such films play an active role in the bacterial adhesion process. In artificial urine, we tried to avoid such naturally-formed conditioning films by applying different current densities to platinum electrodes. The

results were quantified using highly mass-sensitive techniques. The bacterial adhesion could be reduced significantly compared to platinum surfaces without applied currents.

Overall, in this thesis the influence of applied currents to viable cells was investigated and used to control cell adhesion, growth and migration.

Zusammenfassung

Im späten 18. Jahrhundert publizierte Luigi Galvani seine Experimente mit Froschschenkeln und die dabei neu beobachtete Form tierischer Elektrizität. Es dauerte danach fast eineinhalb Jahrhunderte bis Wissenschaftler zu verstehen begannen, wie Zellen elektrische Potenziale generieren und übertragen können. Die Phase der modernen elektrophysiologischen Forschung wurde damit eingeläutet. Diese Entdeckungen, sowie weitere technische Entwicklungen haben dazu geführt, dass elektrische Ströme heute im klinischen Alltag nicht wegzudenken sind und die Lebensdauer / Lebensqualität vieler Patienten massiv erhöhen (z.B. appliziert durch Herzschrittmacher). Der Wunschtraum vieler Wissenschaftler und Ingenieure jedoch wäre, sämtliche körperlichen Beeinträchtigungen mittels Prothesen beheben zu können. Die Steuerung könnte direkt vom Gehirn aus erfolgen, wobei auch sensorische Rückmeldungen ans Gehirn möglich wären (z.B. Position der Prothese, Temperatur oder Gewicht eines angefassten Gegenstandes). Mit derselben Technologie könnten durchtrennte Nervenfasern mit einem elektrischen Schaltkreis überbrückt und gelähmte Gliedmassen / Organe neu innerviert werden, um so ihre ursprüngliche Funktionalität wieder zu gewährleisten. Darüber hinaus könnte man Aufgaben des Gehirns auf einen Chip auslagern oder unseren fünf Sinnen (Sehen, Hören, Schmecken, Riechen und Fühlen) weitere Wahrnehmungsmöglichkeiten hinzufügen. Egal welche phantasievollen, zukünftigen Anwendungen wir uns noch vorstellen können, im Prinzip wird immer eine elektronische Schaltung mit lebenden Zellen verbunden und zwar über eine Grenzfläche aus toter und lebender Materie.

Durch die Implantierung eines körperfremden Materials wird eine Fremdkörperreaktion des Immunsystems provoziert. Rund um das nicht abbaubare Material bildet der Körper eine Bindegewebskapsel und schlussendlich führt dies zu einer reduzierten Funktionalität des Implantates. Wird diese Grenzfläche gleichzeitig für die elektrische Stimulation von Zellen verwendet, induzieren die applizierten Ströme elektrochemische Reaktionen. Für die dort angesiedelten lebenden Zellen werden durch diese Reaktionen lokal lebensfeindliche Bedingungen geschaffen.

In dieser Doktorarbeit untersuchen wir die Auswirkungen solcher Ströme *in vitro* und *in vivo* und präsentieren Möglichkeiten diese Effekte zur Kontrolle von Zelladhäsion, -wachstum und -migration zu nutzen.

In Kapitel 4 entwickelten wir eine hochauflösende Methode, um elektrochemisch induzierte pH-Änderungen in der Nähe einer ITO-Elektrode mittels konfokaler Laser-Scanning-Mikroskopie sichtbar zu machen. Dies erlaubte uns pH-Änderungen in physiologischen Lösungen innerhalb eines Bereiches von 100 μm zu studieren und modellieren. Basierend auf diesem Modell konnten wir die elektrochemisch induzierten pH-Änderungen mit dem beobachteten Verhalten von Myoblasten, die direkt auf der Elektrodenoberfläche gewachsen sind, in Verbindung bringen. Stromdichten ab einem bestimmten Schwellenwert führten bei diesen Zellen zur Aufnahme

eines membranimpermeablen Farbstoffes, welcher dabei als Hinweis zur Bildung von Poren in der Zellmembran diente. Auch beim Eintauchen in Lösungen mit tiefem pH-Wert zeigten die Zellen dieselben Reaktionen. Unser Modell ermöglichte es uns, diese Beobachtungen dem tiefen pH-Wert zuzuschreiben, wobei die Wirkung anderer elektrochemisch generierter Moleküle nicht ausgeschlossen werden konnte.

In Kapitel 5 entwickelten wir einen Neurochip, um die Adhesion und das Auswachsen einzelnener Neuronen mittels elektrochemischer Entfernung proteinresistenter Moleküle von einer transparenten Oberfläche kontrollieren zu können. Die Chiparchitektur basiert auf drei parallel angeordneten Indium-Zinn-Oxid Elektroden. Diese befinden sich auf einem Glassubstrat mit einer Fotolackstruktur als Landeplatz für den Neuronenkörper mit seitlichen Kanälen für das Neuritenwachstum. Die Oberfläche wurde vollständig mit protein- und zellresistentem PLL-*g*-PEG beschichtet, bevor der Platz für den Neuronenkörper mit Hilfe eines Potentials an der darunterliegenden Elektrode freigeschaltet wurde. Nach erfolgter Adhesion der Zelle konnten auch die Kanäle für das Neuritenwachstum freigelegt werden. Des Weiteren zeigen wir auch eine Möglichkeit die Zellmigration unter Nutzung kleiner gepulster Ströme zu verhindern. Myoblasten wurden daher auf einer chemisch strukturierten Oberfläche gezüchtet. Dabei konnten die Zellen nur auf dem Glassubstrat aber nicht auf den ITO-Elektroden adhärieren. Nach elektrochemischer Freischaltung der Elektrodenflächen konnten die Zellen die Oberflächen innerhalb von 24 Stunden konfluent überwachsen. Im Gegensatz dazu, mittels einem kleinen gepulsterten Strom, konnte die Migration der Zellen für > 72 Stunden erfolgreich verhindert werden. Mit diesen beiden Techniken können Zelladhäsion sowie Wachstum und Migration dynamisch kontrolliert werden, auch wenn die Zellen bereits auf das Substrat aufgebracht wurden.

Basierend auf den Ergebnissen der vorangegangenen Kapiteln entwickelten wir in Kapitel 6 einen implantierbaren elektrischen Pulsgenerator. *In vitro* Tests mit Aortazellen zeigten, dass die gewählten Stromdichten gross genug waren, um eine normale Zelladhäsion zu verhindern. Die Zellen bildeten nur eine kleine Kontaktfläche mit der Platinelektrode und behielten ihre Kugelgestalt. Innerhalb von 24 Stunden wurden sämtliche Zellen apoptotisch, was mit Anti-Caspase-3-Antikörpern gezeigt werden konnte. Inspiriert durch diese Beobachtungen, untersuchten wir die Auswirkungen dieser Ströme *in vivo*. Dabei wurde der Impulsgenerator subkutan in Ratten implantiert. Zwar ergab die histologische Untersuchung der Elektroden|Gewebe-Grenzfläche keinen Unterschied zwischen einer aktiven Platinoberfläche und der benachbarten Kontrolloberfläche ohne angelegtem Strom. Die Impedanz bei höheren Frequenzen war jedoch für Elektroden tiefer, die während des ganzen Experimentes Strompulse abgaben, als für Elektroden, die während des Experimentes ihre Funktion einbüssten. Dies wies darauf hin, dass die Einkapselung in einer abgeänderten Form erfolgte.

In Form einer Machbarkeitsstudie in Kapitel 7 präsentieren wir einen neuartigen Ansatz zur Bekämpfung bakterieller Adhäsion, Kolonisation und deren darauffol-

genden Verkrustungen von Foley-Kathetern und Harnleiter-Stents Flächen. *Proteus mirabilis* wurde als Modell-Bakterium für urologisch wichtige Bakterien gewählt. Normalerweise bilden sich nach dem Einführen eines Katheters sofort Ablagerung von Urinkomponenten auf der Katheter Oberfläche, die zur Bildung eines sogenannten Conditioning-Film führen. Diese Ablagerungen spielen eine aktive Rolle beim Adhäsionsprozess von Bakterien. In künstlichem Urin haben wir versucht, die Bildung solcher Filme durch Anlegen verschiedener Stromdichten auf Platinelektroden zu verhindern und mit hochsensitiven Methoden zu quantifizieren. Die bakterielle Adhäsion konnte im Vergleich zu einer Platinoberfläche ohne Strom signifikant reduziert werden.

In der vorliegenden Dissertation wurde der Einfluss elektrischer Ströme auf lebende Zellen untersucht und deren Auswirkungen zur Kontrolle von Zelladhäsion, -wachstum und -migration verwendet.

Contents

List of Figures

1. Introduction

Everyone has at least once felt the electric shock by accidentally touching a voltage source, such as; while plugging in a electric cord with a finger between the two poles (my first childhood memory), touching the electric fence used to deter cattle, or sensing the prickle on your tongue while licking simultaneously the copper plates of a 4.5 V battery. Even though the intensity may differ, these sensations are all caused by electric currents. It is not yet completely understood in detail, what is really happening to living tissue when external electric field is applied or why the tissue itself is creating electric fields [1]. The most convenient and controlled way to study these effects are cell cultures as used in many fields including biology, pharmacology, medicine and biomedical engineering. It is crucial to maintain the cells in healthy condition and keep the environmental factors as controlled as possible, especially important is to provide a surface for cell adhesion necessary for the cells to realize many natural functions such as growth, proliferation and differentiation. The cells interactions with its environment are in focus to study cellular biology. Upon exposing surfaces to culture medium or body fluids, various proteins adsorb on the surface and providing adhesion sites for cells as described in the sections 1.1, 1.2. Synthetic molecules and biocompatible materials were designed to achieve precise control over the surface having predefined cell adhesive or protein repulsive properties.

The combination of both cell adhesive/repulsive properties on the same surface, so called "patterned surfaces", have been applied to cell arrays or co-culture systems to study interactions between cells and between cell and extracellular matrix. So far passive pattering was often used for producing such surfaces prior to an experiment with the disadvantage, that the surface properties can not be altered after initiating the experiment. The different methods and examples are described in section 1.3.1. But researches asking for more control over the surface properties during the experiment nowadays, leading to the development of active surface patterning methods, so called "stimuli responsive" surfaces (Section 1.3.2), where the properties can be switched dynamically at any stage of the experiment e.g. by photons, enzymes or electric potentials. Such developments help to realize new experiments such as controlling the wiring of neurons in culture, studying the dynamics of basic neuron networks and providing an essential step towards understanding how the brain performs functions such as memorizing and learning. The focus in the sections 1.3.1,1.3.2 lies therefore more in how to control actively the growth of neurons in culture. If the surface is switched electrically also electrochemical reactions oc-

curring at the electrode interface and have to be taken in account above a certain electrode potential as introduced for NaCl solution in section 1.5.

Electric currents and potentials are already applied in medicine in e.g. cardiac pacemakers, cochlear implants and brain implants. A short historical and application overview is given in section 1.4. Long-term complications occur upon implantation of any material implanted in the human body resulting in loss of recording or stimulating capabilities due to the host tissue reaction leading to encapsulation of the electrode material. Also high currents or potentials applied, can harm the surrounding tissue or lead to corrosion of the electrode surface due to electrochemical reactions at the interface. An introduction to this topic is given in section 1.4.2.

1.1. Protein adhesion to surfaces

Proteins or polypeptides are linear chains of amino acids as building blocks. Depending on the amino acid sequence and its length, the proteins are fold into 3D structures (conformation) and participate, alone or in protein complex, in almost every process within cells and between cells. Proteins are amphiphatic (hydrophilic and hydrophobic properties) molecules making them intrinsically surface active. The accumulation of proteins at interfaces can be both advantageous or problematic. On the one hand it is necessary for the development of biosensors, immunological tests, biomedical implants etc., whereas on the other hand in many cases the formation of protein- or biofilms can be a disadvantage and elicit host reactions such as severe immunological response, blood coagulation or bacterial adhesion. On the other hand, cells only bind to surfaces with specific protein binding sites. Proteins interact through different intermolecular forces (Coulombic, van der Waals, Lewis acid-base) with surfaces. Because of their long linear design, they also interact through entropically based effects such as hydrophilic/hydrophobic interactions and conformational entropy. Upon adsorption on the surface, the protein might also alter its conformation and loose its biological functionality due to intramolecular forces. This is also reason for the different kinetics behavior of proteins in adsorption and desorption or even showing apparent irreversibility of the adsorption process [2].

In order to study protein adsorption and protein cell interactions, well defined surfaces are needed and brought up the concept of using self assembling monolayers (SAMs). SAMs are spontaneously organized assemblies of molecules formed by adsorption from a solution or from a gas phase. The engineered amphiphilic molecules have a head group that binds to the substrate and alkyl chain connecting to a functional end group at its tail. The molecules start to assemble in a crystalline structure in order to cover the whole surface in a single monolayer presenting their end group. The end group could be small goups such as -OH, -NH_3, -COOH to turn the surface hydrophilic or peptides to study protein interactions [3].

The most benefit using SAMs, compared to methods using adsorbed protein films is the control over the exact composition. In other cases it is preferred to turn surfaces protein repulsive "non-fouling", so the SAM end group can be a ethylene glycol (EG) or poly(ethylen glycol) (PEG) [4], which present a water like interface and due to steric repulsion proteins are excluded from approaching the surface. So the surface resists non-specific (physical) protein binding.

Another type of molecules often used for surface modifications are polyelectrolytes. The molecules electrostatically interact with an oppositely charged surface due to an ionizable group along the backbone chain. Kenausis et al. presented a protein resistant polycationic polyelectrolyte, poly(L-lysine)-*grafted*-poly(ethylene glycol) presented in methods and materials section 3.7.2 and used in this thesis.

1.2. Cell-matrix interactions

In vivo, mammalian cells express multiple adhesion molecules on their surface to adhere and spread on a biological matrix called the extracellular matrix (ECM). The major cell adhesion molecule classes enabling cell to adhere are: (i)Immunoglobulin superfamily members playing the major role in the immune system in animals, including immunoglobulines, cell surface antigen receptors and antigen presentation in lymphocytes. (ii) Cadherins are calcium dependent adhesion molecules ensuring cell to cell adhesion in tissue. (iii) Selectins are a family of cell adhesion molecules (CAMs) able to bind to sugar moieties or sugar polymers. (iv) Integrins are receptors to bind and mediate between cell and its surrounding translating the information from the extracellular matrix (ECM) as well translate information about the status of the cell to the outside. The ligands regulate cellular processes including adhesion, migration, growth, secretion, gene expression and apoptosis, wich are controlled or triggered by the ECM. Many important adhesive proteins (e.g. fibronectin, laminin, vitronectin, fibrinogen, collagen) contain an Arg-Gly-Asp (RGD) sequence, which is the key to many integrins and allows the cell to adhere to such proteins. Without adhering to a surface via integrins, the cell typically commits suicide (apoptosis) [5]. In vitro, synthetic molecules with the peptid sequence RGD are used to adress specific cell binding and elicit specific cell responses [6–8]. Another sequence Ile-Lys-Val-Ala-Val (IKVAV) was indentified from laminin and is also synthetically produced to promote cell adhesion, spreading, migration and neuron outgrowth [9, 10].

Prokaryotes (bacteria and archea) produce multiple adherence molecules called adhesins. The adhesins are expressed on the bacteria pili, flagellae or on the bacteria surface. The bacteria *Proteus mirabilis* used in this thesis, is a common cause of catheter-associated urinary tract infections and attaches to catheter surfaces with a greater affinity than other gram-negative bacteria. The swarming behavior is a distinct characteristic of this bacteria and it has been shown that *Proteus*

mirabilis can attach to every catheter material, such as ethylene, propylene, sulfonated polystyrene, silicone [11]. Many adhesins are thought to bind to these surfaces and the conditioning film formed by host urinary components minutes after insertion. Wherefrom, the pili and hemagglutinins are thought play the most important role in the colonization of the catheter surfaces and urinary tract [11].

1.3. Surface patterning to control cell adhesion, growth and migration

1.3.1. Passive surface patterning

Experimental techniques in biomedical engineering often involve the use of patterned substrates to study fundamental cellular processes. The patterned surfaces are engineered to specifically influence cell adhesion, outgrowth, migration, organization and tissue development by providing alternating surface properties, cell adhesive and repulsive, in the micrometer range. In principle the cells are seeded on prefabricated substrates patterned either with different materials e.g. metals, metal oxides or organic molecules which preferably do not change their properties during the experiment. Such passive substrates are patterned by normal photolithography techniques for spatial arrangements of different solid materials [12], protein-aqueous materials [12–16], polyelectrolytes [17, 18] or self-assembled monolayers (SAMs)(Fig.1.1, A), [19, 20]. Photolithography in combination with laser ablation [21] was also reported. Another method, μ-contact printing developed by Whitesides et al., uses a microstructured elastomeric stamp made of poly-(dimethylsiloxane) (PDMS) (Fig.1.1, B, C), [22]. This printing technique is mostly used to transfer patterns of poly(L-lysine) (PLL) [23–28] or extracellular matrix proteins such as laminin, fibronectin to a flat substrate. Instead of proteins, synthetic molecules (e.g. SAMs or polyelectrolytes) consisting of substrate binding sites and specific cell-adhesive peptide sequences (e.g. RGD, IKVAV, etc.) can be printed onto solid materials [29–31]. Another approach for patterning cells is to provide a 3D structure on a surface were cells can attach and grow inside or along the structure. Merz and Fromherz used lithographically patterned SU8 polyester structures to guide individual snail neurons (Fig.1.2, A), [32, 33].

Topographical effects of smaller structures such as silicon pillars and micron sized holes on neuron growth were also investigated [35, 36]. There were also attempts to culture neurons in microfluidic platforms allowing directed growth of neurites from their cell bodies [37] or pattern them at low densities for further differentiation [38]. It has also been tried to trap the neurons mechanically in parylene cages positioned on electrode sites of a multielectrode array (MEA) chip. The cell body is hold in place by the cage, while the neurites are free to grow into the surrounding area (Fig.1.2, B), [34].

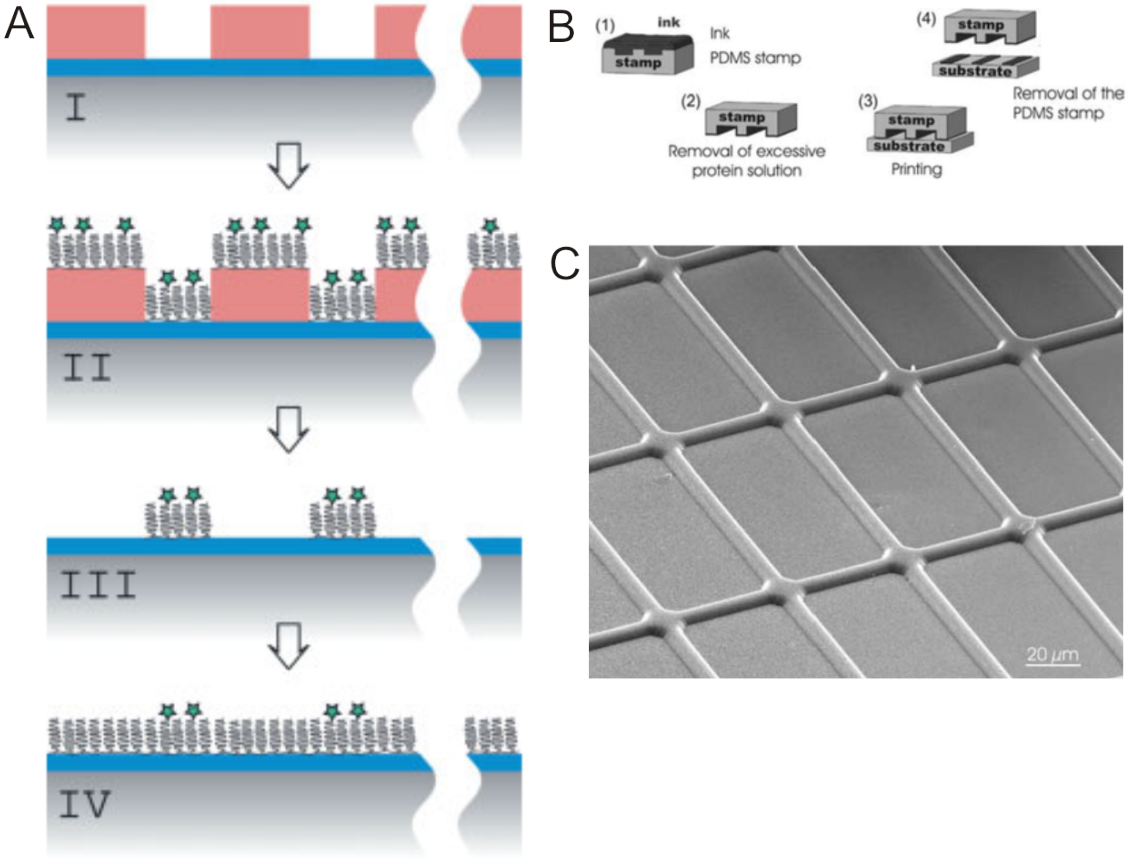

Figure 1.1.: (A) Molecular-assembly patterning by lift-off (MAPL). A photoresist pattern (Stage I) is dipped into solution of surface adhesive and functionalized molecules (Stage II). The photo resist is removed (Stage III) with an organic solvent and the remaining free surface is backfilled with another surface adhesive molecule (Stage IV), [12]. (B) μ-contact printing involving an elastomeric stamp (1) is soaked in ink solution containing biomolecules and then is dried in a stream of N_2 (2) leaving back a thin layer on the stamp surface. The stamp is pressed against to surface (3), leaving back the biomolecules (4) at the position of the raised structures of the stamp shown in figure (C) [23].

1.3.2. Active surface patterning

All these methods provide a prefabricated passive patterned surface for cell cultures. Nowadays, the challenge shifts towards more complex structures built of different cell types [3] or to build topographically controlled neuron networks towards further understanding how the brain works or to study the effects of neuron active drugs [39] *in vitro*. It is therefore crucial to develop more versatile patterned surfaces with

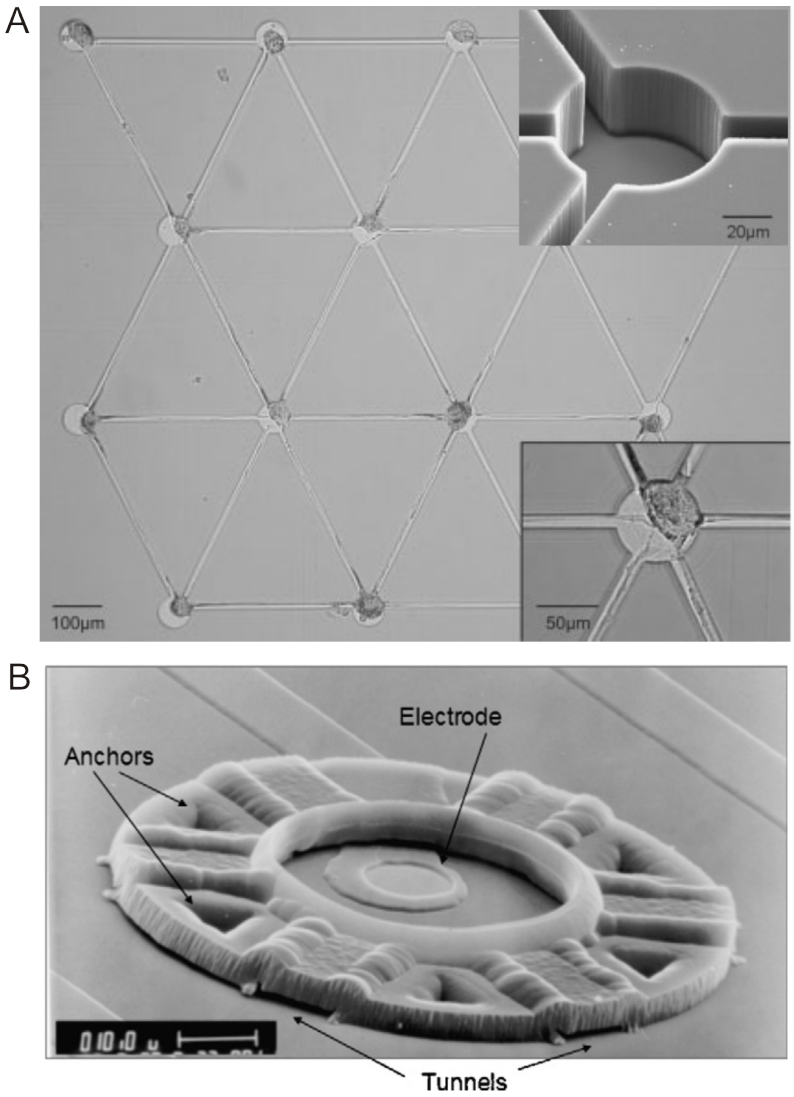

Figure 1.2.: (A) Silicon chip with a polyester structure to control snail neuron network growth. Top inset shows a scanning electron image of the guidance structure. Bottom inset shows a neuron soma and neurite extensions inside a topographic structure [33]. (B) SEM of a parylene neurocage design, where a neuron is placed in the center and dendrites are free to grow through the channels and connect with other neurons sitting in other cages (scale bar 10 μm) [34].

active control over the surface properties at any point in time of the experiment. These so called stimuli responsive surfaces [40] switch their surface properties triggered by photons, enzymes, temperature or electric potentials. Sarig-Nadir et al. used a laser to change the local properties of a PEGylated fibrinogen hydrogel to

allow the outgrowth of a neuron in the desired direction [41]. Another way to realize a dynamic control over the surface during cell culturing was introduced by Yeo and Mrksich. They used alkane-thiol SAMs on a gold surface exposing cell adhesive RGD ligands attached to an electroactive group [42]. Upon applying an electric potential the electroactive group with the ligand is released resulting in the detachment of adherent fibroblasts from the surface. Kaji et al. described a method using a conductive probe to generate an HBrO (oxidizing agent) from the Br^- containing solution in the vicinity of an albumin coated surface [43, 44]. Locally, the albumin was turned cell-adhesive and permitted the cells to grow along the trace of the conductive probe. Zhao et al. showed that protein- and cell- repulsive (EG)-terminated SAMs become cell-adhesive upon exposure to electro-generated Br_2 [45]. Fan et al. used pluronic polymer coated electrodes and was able to control the protein adsorption by tuning the voltage bias on the microelectrodes [46]. Li et al. described a method to pattern cells by prior electrochemical desorption of SAMs in localized areas defined by a microfluidic system [47]. Cells could also be patterned by simple electrochemical desorption of PEG silane SAMs from gold [48] or ITO electrodes [49].

1.4. Electrodes in biology

1.4.1. "Animal electricity" then and electrophysiology today

Officially, Luigi Galvani presented 1791 in "De viribus electricitatis in motu muscolari commentarius" his experiments with frog legs and the finding of new form of electricity "animal electricity". His discovery provoked criticism of Alessandro Volta, the future inventor of the battery. Galvani believed that the animal electricity comes from the muscle, while Volta believed that the animal electricity was a physical phenomenon. After the death of Galvani and due to the success of the battery, "animal electricity" disappeared from the science community. Reymond Du Bois, clarified some of Galvani's experiments and wrote into the introduction that "animal electricity" has not been taken in consideration other than Voltaic electricity. The modern phase of electrophysiological research started in Cambridge around 1943 [50]. Researchers began to understand how potentials are produced in animal cells and how action potentials are transmitted between cells, how muscles contract and how photon signals are translated into electric signals and sent to the brain, but so far without understanding the whole complexity of a brain or even smaller neuron networks. However, currents and potentials are already applied to many human organs including the brain. Special electrodes are typically used for stimulating or recording of electrically excitable tissues e.g. cardiac pacemakers [51], cochlear implants [52], deep brain stimulation as a treatment for patients with severe movements disorders (Parkinsons disease), essential tremor,

dystonia or even obsessive-compulsive disorders [53], retinal implants [54], brain machine interfaces [55], neural interface for selective recording and stimulation of nerve fibers [52, 56, 57].

1.4.2. Bioelectrodes and tissue reactions

In the above mentioned applications, the electrical stimulation parameters are set not to harm the surrounding tissue or the electrode itself. To avoid tissue harm, the electric pulses are of short duration (micro- or milliseconds) and the pulses are applied in so called charge balanced waveforms to reduce/avoid Faradaic reactions (see section 1.5) occurring at high total charge delivery with longer monophasic pulses. Shannon et al proposed an expression for the maximum level for safe stimulation by relating the charge density per phase versus the charge per phase for surface electrodes on the cortex [58] based on empirical data [59, 60]. Besides the tissue damage, electrical stimulation in the unsafe region can lead to electrode corrosion. The mechanisms for stimulation induced tissue damage are not well understood, but two mechanisms are proposed: (i) either overstimulation of the central nervous system (CNS) leads to biological misbalance of the involved neurotransmitters, glucose; or (ii) ions or the creation of intolerable high amount of toxic products by Faradaic reactions at the electrode tissue interface [61]. Even if currents are applied in the safe region, all intracorporally implanted materials e.g. electrodes or biosensors provoke a foreign body reaction [62, 63]. The foreign material is encapsulated by e.g. microglia, astrocytes, endothelia, fibroblasts depending on the place of implantation, a problem that has not been solved to date. These encapsulating cells and extracellular matrix shield the electrode from the tissue of interest [64] and limit the functionality of implanted biosensor devices e.g. glucose sensors [65]. Due to encapsulation, the resistivity of the tissue increases with time [66], resulting in loss of neuronal recording or, lower stimulation capability and subsequent higher power consumption of the stimulation device. A lot of research has focused on material coating strategies to avoid this encapsulation [67–69]. In addition, a fully electrical solution was also proposed to prolong the signal-to-noise-ratio during the lifetime of chronically implanted electrodes. During this so called rejuvenation, a 1.5 V DC bias is applied to an iridium electrode for 4 s. This was able to reduce the impedance at 1 kHz for a few days enhancing the signal-to-noise ratio of the recording [70]. The reasons for this phenomenon are not yet clear, but conductivity pathways might be formed through the shielding tissue. Other long pulsed current densities (0.57 A/m^2) have shown to kill cells on ITO microelectrodes within 2 min of exposure (see chapter 4). With higher frequency (2.5 V, 40 kHz, up to 30 s), cells are killed deliberately, as shown in the wound healing assay described by Keese et al. [71]. Cell death in biology may occur in different ways: Necrotic cells die by irreversible membrane rupturing and release their content inducing an inflammatory response in the surrounding tissue. In contrast, apoptotic cells undergo

a more physiological (programmed) cell death involving the activation of caspases, the central executioners of the apoptotic pathway [72]. These cells are then cleanly removed by macrophages and subsequent intracellular digestion without provoking an inflammatory response [73]. This also makes the apoptotic pathways favorable for anti cancer therapy [74, 75]. Higher voltage short pulsed currents (from 10 s to several ms) are used in electroporation for DNA transfection and drug delivery [76, 77]. Studies have shown such pulses used for electroporation induce both necrosis and apoptosis [78, 79], whereas lower voltage (7.5 V/mm) and long duration pulses (100 ms) can reduce necrotic cell damage [80]. Lower voltages have been used to electrically improve wound healing with direct currents to reduce bacterial colonization [81]. Electrically induced apoptosis has been observed in direct current treatment against a leukemic cell line [82]. It has been shown that even small galvanic currents (4 V/m, 5 A) arising from different metal alloys used in tooth restoration can induce apoptosis in the oral mucosa [83]. Mild unfavorable conditions produced with long pulsed (s), small current (0.38 A/m^2) inhibit the migration of cells onto microelectrodes (Chapter 5). These effects were limited in time (only while current was applied) and in space, since neighboring cells were not affected. The origin of the observed phenomena is based on the interface between electrode and adsorbed protein aqueous layer on which cells can adhere. The next section is introducing therefore the electrostatic interactions of ions with the charged surface (Section 1.5.1) and the electrochemical reactions induced upon applied electric currents (Section 1.5.2).

1.5. Basic electrochemistry

1.5.1. Electrical double layer

A freshly plasma treated or cleaved surface presents presents severed chemical bonds of the solid material. In case of strongly polar compounds (e.g. SiO_2, indium tin oxide) the surface is chemisorbing water vapour immediately after exposing to ambient air. The H_2O molecules are chemisorbed (forming hydrogen bonds) or hydroxyl group forming a covalent bond after H_2O dissociation. If the surface now is brought in contact with a liquid, the surface can acquire a charge at the interface depending on the specific adsorption/desorption of ionic species from the solution or via an external electric field applied. The adsorption of anions will lead to a negative and cations to a positive surface charge. The surface charge density and zeta potentials of oxides are dependent on the solutions pH and ionic strength. Surfaces in pH lower than the point of zero charge become positively charged.

If such a charged surface comes in contact with other charged species in solution, the oppositely charged species are attracted and form a layer to compensate the electric charge of the surface. This layer has a different composition from the

bulk solution and is known as electric double layer. A first theory to describe this electric double layer was proposed by Helmholtz treating the double layer as a simple capacitor. The Guoy and Chapman improved the model by introducing a diffuse model of the electric double layer with exponentially decreasing electric potential away from the surface to the bulk solution. The most commonly used model is the combined Guoy-Chapman-Stern model, assuming a "plane of closest approach" and a portion of excess ions remain and attach to a "diffuse layer" [84].

In this thesis the spontaneous adsorption of the polyelectrolytes PLL, PLL-g-PEG (Section 3.7.2) was used to modify surfaces. At physiological pH (pH 7.4) these polyelectrolytes are positively charged and the used substrates (SiO_2, indium tin oxide) are negatively charged. It should be noted that the electrostatic interaction is dependent on pH and ionic strength of the solution.

1.5.2. Electrolysis in aqueous NaCl solution

All body fluids, culture medium and physiological buffers contain a certain amount of NaCl to adapt to the inner osmotic pressure of mammalian cells. If potentials or currrents are applied by electrodes to such solutions, electrochemical reactions might occur above certain potentials. The main reactions are: (i) at the cathode H_2O (Reaction 1.1) is more easily reduced than sodium ions (Reaction 1.2), which is reflected in their different standard reduction potentials E° vs. normal hydrogen electrode (NHE). (ii) at the anode oxidation of Cl^- ions and H_2O molecules may occur. Even though the oxidation of H_2O (Reaction 1.3) is thermodynamically favored due to its lower standard reduction potential at equilibrium situation compared to chloride (Reaction 1.4), chloride formation is kinetically favored [85]. The net current generated by the reduction or oxidation of substances at the working electrode are called Faradaic currents. In this thesis anodic potentials and currents were applied to the working electrode and therefore the reaction 1.3 to low pH and toxic amounts of hypochloric acid (Reaction 1.4, 4.1) were taken into account in the discussion sections of the relative chapter.

(i)Reactions at the cathode in aqueous NaCl solution

$$2H_2O + 2e^- \longleftrightarrow H_2 + 2OH^- \qquad E^\circ = -0.83\, V vs.\ NHE \tag{1.1}$$

$$Na^+ + 1e^- \longleftrightarrow Na \qquad E^\circ = -2.71\, V vs.\ NHE \tag{1.2}$$

(ii) Reactions at the anode in aqueous NaCl solution

$$2H_2O \longleftrightarrow O_2 + 4H^+ + 4e^- \qquad E^\circ = 1.23\, V vs.\ NHE \tag{1.3}$$

$$2Cl^- \longleftrightarrow Cl_2 + 2e^- \qquad E^\circ = 1.36\, V vs.\ NHE \tag{1.4}$$

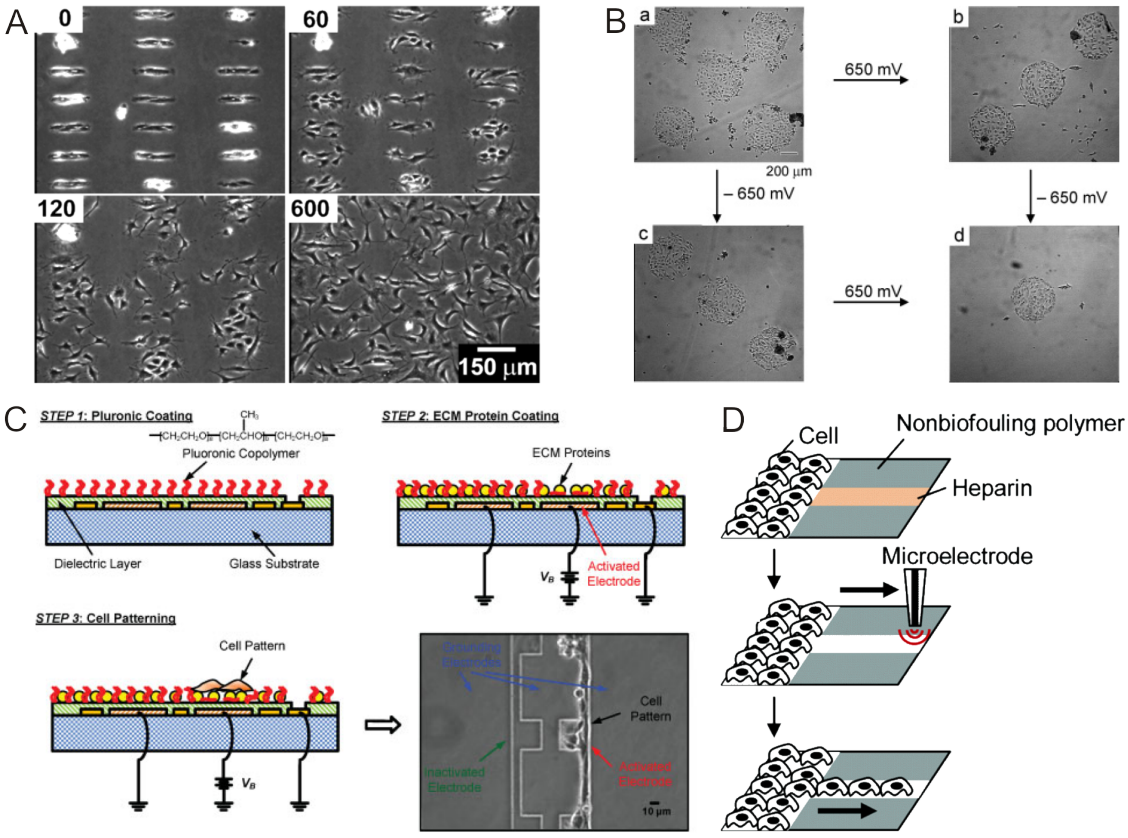

Figure 1.3.: (A) Endothelial cells attached on protein adsorbing SAM pattern surrounded by protein resistant (EG)-terminated SAM molecules. Upon applying -1.2 V for 30 s the EG-terminated were desorbed from the surface and cells started to spread from microislands to the now cell adhesive surface. The numbers indicate the elapsed time (in minutes) after the voltage pulse [48]. (B) Fibroblasts adhered only to regions presenting RGD ligands. The ligands were chemically bound in two different ways to the surface binding molecule, allowing the release of the RGD ligand by applying a positive (b) or a negative (c) potential of 650 mV [42]. (C) (STEP 1) Insulated surface electrodes are coated with pluronics polymer that is presenting the protein repulsive hydrophilic PEG chains at low density, at which proteins can adsorb to the surface but not cells (STEP 2) due to the steric repulsion of the side chains. By applying a 60 V bias (STEP 3), the pluronics polymers properties were changed to cell adhesive allowing adhesion and outgrowth of cells [46]. (D) A cell repulsive polymer is patterned by μ-contact printing and the free surfaces are coated with PEI/Heparin complexes. A micropipette, containing Br_2 ions was brought in close contact with the heparin surface and a potential is applied between the inside of the pipette and solution. The electrochemically produced HBrO and its oxidative action caused the PEI/heparin complex to desorb allowing other protein adsorb and permit the outgrowth of HeLa cells.

2. Scope of the thesis

The introduction provided an overview about cell adhesion to surfaces and the importance of patterned surfaces. Especially interesting are patterned surfaces, which allow to alter the surface properties actively at any time of the experiment, so called stimuli responsive surfaces. Such active surface patterning techniques enable unprecedent biological experiments, such as the built of topologically controlled neurons networks. The most convenient way to realize an active control over a surface is realized by electronic control, since modern microfabrication technology allows the integration of circuits in the nanometer range in mass production. We also highlighted the applications of bioelectrodes in modern medicine and their intrinsic long-term drawbacks were discussed. In this thesis, the focus is on finding new ways of changing surface properties by applying electric potentials or currents to enable cell growth or inhibit cell adhesion *in vitro* and *in vivo*, and we tried to find a method to avoid long-term effects on implanted electrodes.

In chapter 4, we focus on the development of a fast high-resolution method tho measure the pH change due to electrochemical reactions close to a electrode using confocal laser scanning microscopy. Such a method would allow to study and model pH changes in physiological solutions within a hundred micrometer range, where no other pH measurement can bring the necessary velocity and resolution. Visualizing such local pH changes is highly interesting for thin film applications and electrochemistry. Using a simple diffusion model, we connected the electrochemically induced pH changes with the observed behavior of cultured myoblasts directly grown on the electrode surface after applying different current densities.

In chapter 5, we explored a novel way to electrically control the adhesion of neurons and electrically enable the outgrowth of neurites inside a polymeric 3D structure. A neurochip was developed with the requirements of having a transparent electrode substrate for light microscopic observation and having a 3D structure mechanically supporting neuron cells. The whole neurochip surface was turned protein and cell resistant before enabling neuron adhesion and neurite outgrowth by selective electric switching of the surface properties. We also investigated a possibility to control cell migration without the use of any surface modifying molecules and use only small pulsed currents.

Previous experiments have shown, that small pulsed electric currents inhibit cell

adhesion and migration *in vitro*, in chapter 6 we investigated this effects *in vivo*. Therefore, we built an implantable pulse generator and studied the effects of small pulsed currents on the viability on rat aortic derived cells *in vitro*, first. Then, we implanted the electric pulse generator into rats to study the effects on living tissue within a time period of 21 days and tried to relate the observed impedance changes over time of the implanted electrodes with the histological data.

In chapter 7, the idea of preventing mammalian cell adhesion and migration on surfaces by electric means was extended on bacteria in an attempt to solve a clinical issue on ureteral stents. Despite the material developments and surface coatings, such urogenital catheters encounter bacterial colonization in long-term use, which lead to infections and require the administration of antibiotics to the patient. We tried to avoid bacterial adhesion by applying different current densities to platinum electrodes as a possible catheter coating material in artificial urine.

This thesis ends with a summary of the most important findings and an outlook to the remaining challenges and possibilities.

3. Methods and materials

This chapter describes the different imaging and quantification techniques, buffers, solutions, synthetic molecules, surface preparation, cell culture and implantation protocols. Furthermore the fabrication process steps and assembly of the electrode containing substrates and implantable pulse generator are explained and illustrated. At the end of the chapter, a diffusion model is presented and used to fit different parameters allowing the prediction of pH values between an electrode and an adherent cell after electrically inducing a pH change. More detailed information about the particular experimental techniques is given in the experimental section of each chapter 4, 5, 6, 7.

3.1. Imaging techniques

3.1.1. Fluoresence microscopy

Fluorescence is a quantum effect and occurs when a molecule, atom or nanostructure relaxes to its ground state after being electrically excited. In fluorescence microscopy, the specimen is mostly labeled with fluorescent molecules (e.g. fluorescein, rhodamine etc.) and some specimen might even show autofluorescent behavior. Illuminating the specimen with light of a specific wavelength(s)causes fluorophores to emit light of longer wavelengths. In the microscopy light path, emitted fluorescence is separated from the excitation light using emission filters. The fluorescence can then be seen by eye or detected with a CCD camera for imaging. Due to long exposure times fluorophores can loose their fluorescence properties (photobleaching). Some fluorophores are pH sensitive and can therefore be used as pH probes e.g. to measure intracellular pH.

3.1.2. Confocal laser scanning microscopy

The confocal laser scanning microscope (CLSM) is a more advanced fluorescence microscope. Instead of illuminating the entire specimen with light, a focused laser of a specific wavelength(s) is scanning the area of interest and can achieve higher excitation power than a normal fluorescence microscope. The image is made pixel-by-pixel by collecting any fluorescent light from the illuminated volume. As in normal fluorescence microscopy, the fluorescence light is separated from the laser

light by emission filters and using a pinhole in the light path. Fluorescence from out-of-focus volume can be suppressed, which results in much sharper images along with the defined depth of the specimen. This allows obtaining images in various horizontal focal planes within the sample and the reconstruction of 3 dimensional images (z-stacks).

In this thesis, a Zeiss LSM 510 equipped with a oil 63x/1.4 NA M27 plan-apochromat objective was used for high resolution confocal laser scanning microscopy.

3.2. Material adsorption quantification techniques

3.2.1. Electrochemical optical waveguide lightmode spectroscopy (EC-OWLS)

Optical waveguide lightmode spectroscopy (OWLS) is a surface sensitive technique to quantify the adsorption of biomolecules on surfaces. The quantification principle is based on measuring the incoupling angle of laser light into a planar waveguide with a diffraction grating. By varying the angle of the incident laser beam, transverse electric (TE) and transverse magnetic modes can be excited (TM). The produced evanescent field along the waveguide surface extends up to 200 nm above the waveguide and is then sensing in the optical properties (refractive index) of the adsorbed media at the waveguide/media interface and the incoupling angle is changing accordingly [86–88]. The adsorbed mass per unit area M (Eq.3.1) is calculated using de Feijter's formula:

$$M = d_A(n_A - n_C)/\frac{dn}{dc} \tag{3.1}$$

- M: mass per unit area
- d_A: thickness of the adsorbed layer
- n_A: refractive index of the adlayer (dn/dc=0.18 for proteins [89])
- n_C: the refractive index of the medium
- dn/dc: refractive index increment

Electrochemical-OWLS (EC-OWLS) is an extension of this technique, which makes it possible to study the adsorption of charged analytes onto an ITO coated waveguide under applied potentials. This allows for the study of electrochemical surface reactions as well as the measurement of the effect of applied potential on polyelectrolyte adsorption. The instrument includes an electrochemical flow cell

with a ITO coated working electrode which is the sensor (OW 2400c, 50 nm ITO) at the same time, and a silver reference electrode and platinum counter electrode [90]. All parts were purchased from MicroVacuum, Hungary. The waveguides were ultrasonically cleaned in isopropanol for 10 min and in H_2O for 10 min, then extensively rinsed with H_2O and blow dried with N_2, followed by oxygen-plasma cleaning for 2 min.

3.2.2. Electrochemical quartz crystal microbalance with dissipation monitoring (EC-QCM-D)

Quartz crystal microbalance (QCM) was developed to quantify thin film deposition using a QCM sensor made of a thin quartz disc sandwiched between two electrodes. By applying an alternating voltage across the quartz crystal, a mechanical oscillation is induced. If the film is strongly coupled to the resonator, the adsorbed mass can be calculated according to Sauerbreys equation [91].

$$\Delta m = -C\Delta f/n \tag{3.2}$$

- m: adsorbed mass per unit area
- C: mass sensitivity constant
- Δf: frequency shift
- n: overtone number $n \epsilon$ [1,2,..]

An improvement of the QCM technique is the simultaneous measurement of the energy dissipation (QCM-D) together with the resonance frequency. In many cases an adsorbed film can not be simply described by this rigid model. In case of our films, some deviation from the Sauerbrey relationship was measured, due to the visco-elastic nature of the adsorbed film and its water content. By assuming a Voight model, using the 3th, 5th, 7th, 9th overtones according to Voinova et. al [92] and the software package Q-Tools (Q-Sense, Sweden), it was possible to estimate the mass density during the current applications. We studied the film formation under an applied current in an electrochemical cell (EC-QCM-D) using a QE 401 instrument with a QEM 401 electrochemical cell with platinum coated crystal QSX 314, all purchased from Q-Sense, Sweden.

3.2.3. Atomic force microscopy (AFM)

The atomic force microscope (AFM) is collecting surface information by scanning a small probe over a surface. The probe is mechanically attached at the end of a cantilever with defined stiffness. If the probe senses attractive or repulsive forces

from the surface, the cantilever is bent and this can be registered by e.g. measuring the deflection of a laser beam reflected on the backside of the cantilever. The probe can be moved by piezoelectric actuators over the surface in different modes. In contact mode (static) the cantilever deflection is kept constant wheres in non-contact tapping mode (dynamic) the cantilever is oscillated at or close to its fundamental resonance frequencies. Interacting forces between probe and surface change the oscillation behavior and provide information about the surface forces. The AFM is even "gentle" enough to visualize soft material such as living cells, lipid bilayers or polyelectrolytes. Under optimal conditions (vacuum, low temperature) resolutions in the fractions of nanometer can be achieved with AFM technology. We investigated our films with a NanoWizard 1 BioAFM (JPK, Germany) and using Mikromasch CSC38/noAl cantilevers.

3.3. Potential and current control devices

3.3.1. Potentiostat and galvanostat

Potentiostats are electronic power supplies delivering precisely constant voltage used for electrochemical experiments. The potential is controlled at the working electrode (WE) relative to a reference electrode (RE). The current needed to maintain the preset potential is passed through the counter electrode (CE) and is measured to get information about changes of the electrochemical system. Short circuiting RE and CE allows to use the potentiostat as two electrode voltage source (galvanostat). The galvanostat controls the applied current precisely between WE and the two short-circuited RE-CE. In this thesis two different potentiostat models were used: AMEL 2053 (AMEL electrochemistry, Italy) and Autolab PGSTAT302N (Metrohm Ag, Switzerland). Depending on the experiment the working electrode was an indium tin oxide or platinum electrode. In three electrode configuration, a chlorinated silver wire was used as RE and a platinum wire or surface as CE. In two electrode configuration, the short-circuited RE-CE was a platinum wire or surface.

Cyclic voltammetry is an electrochemical experiment, where the potential is linearly cycled (ramped) between two preset potentials. The measured current is then plotted vs. potential to get the cyclic voltammogram. The inset in figure 4.5 was made using a Autolab PGSTAT302N potentiostat and the potential was cycled between 0 - 2.2 V.

Impedance Spectroscopy is a tool to characterize the electrical properties of electrode materials and its interface. In principle, the impedance is measured by applying an alternating potential and gives the resistance as a function of the frequency. The analysis provides static information about the system such as dielectric coefficients, properties of the interface system and dynamic information due to charge

transfer or adsorption phenomena. In section 6.2 the impedance spectra of the implanted electrodes were measured with an Autolab PGSTAT302N potentiostat and the Frequency Response Analyzer Software v.4.9.007 from Eco Chemie (Utrecht, Netherlands). The spectra were measured with an amplitude of 50 mV between 0.2 Hz and 1 MHz.

3.3.2. Implantable electric current pulse generator

An electric current pulse generator was built with prospect for implantation using a low power astable multivibrator HEF4047BT from Philips (Distrelec, Switzerland) powered by a 3 V, 25 mAh coin cell lithium ion battery (Energizer CR1216, France). Ohmic resistor (10 MΩ) and capacitor (220 nF) were used to set the period of the current pulses. This way the pulse generator delivers two differently pulsed direct current (DC) square wave signals at different ports (2.5 s current, 2.5 s pause referred to hereafter as electrode 1); (5 s current, 5 s pause electrode 2) and the third port served to close the circuit. Another ohmic resistor (2 MΩ) was connected in series to each output as a voltage/current convertor according to Ohms law, producing a current I = 1.5 μA per electrode of 0.37 A/m^2, whereby the ohmic resistance of the culture media is negligible. The electronic circuit and battery were mounted on a printed circuit board (11 x 11 x 0.8 mm). Inside custom built Teflon molds, the whole circuit was embedded in EPOTEK-320M and cured at 60°C for 6 h. The dimensions of the pulse generator implant without electrodes were 19 x 19 x 7 mm (Fig. 3.1).

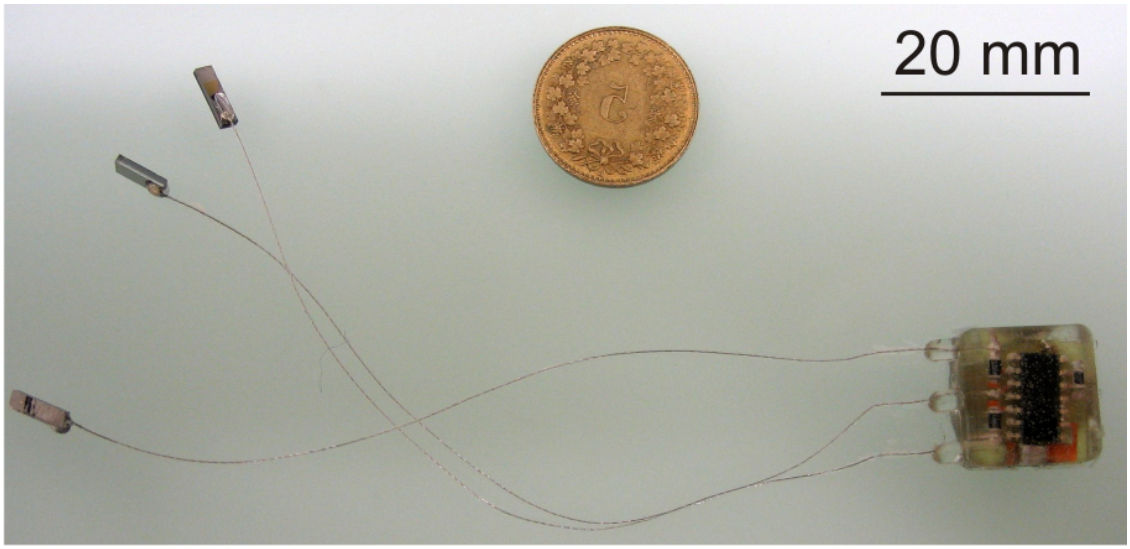

Figure 3.1.: Photograph of the whole implant consisting of the pulse generator (electric circuit and battery) embedded in epoxy resin and the three electrodes in comparison with a 5 cent Swiss coin.

3.4. Chip and substrate fabrication

3.4.1. Indium tin oxide substrates

Microscopy cover slides (24 x 24 x 0.17mm) were sputter coated with 50 nm indium tin oxide (ITO) layer at the Institute of Microtechnology, University of Neuchâtel, Switzerland. A wet etching mask was produced by common photolithography, with Shipley S1805 photoresist (Rohm & Haas, Germany) in a Karl Süss X380 mask aligner, on the ITO cover slide before etching in 3M HCl. After etching, the photoresist was removed by immersion in pure acetone for 5 min, followed by rinsing in isopropanol, ethanol and H_2O. The production process remained the same for all ITO substrates except using different masks (Appendix A.1, A.4). Polymer masks were fabricated at our institute and chromium masks were custom made at Delta Mask, NL.

Neurochip fabrication and assembly

The cover slide with the etched ITO electrodes was put on a heating plate at 150°C for 20 min to remove adsorbed water and improve the SU8 adhesion. Then, an SU8 layer (GM1040, Gersteltec, Switzerland) was spin coated in two steps onto the substrate to achieve a more homogenous thickness. The first layer was 4 μm thick (1000 rpm, 40 s) and the second layer 10 μm thick (400 rpm, 40 s), whereby each layer was consequently soft baked (10 min, 65°C; ramped to 95°C (ΔC=2°C / min); 30 min, 95°C). The combined SU8 layers were exposed for 32 s through a chromium mask (Appendix A.4) and post baked with the same temperature profile as used for the soft baking. The SU8 structure was developed in 2-methoxy-1-methylethyl acetate (PGMA) for 2 min, rinsed with isopropanol and dried at ambient air, before hard baking the SU8 at 135°C for 2 h on a hot plate (Fig. 5.1). The neurochip used for the experiment was assembled from different parts to form a whole unit providing a liquid chamber for cell culturing and macroscopic electrical contacts (Fig. 3.2). The ITO electrodes were therefore connected with silver epoxy resin to corresponding copper paths on a printed circuit board (PCB) (Appendix A.3). To form the liquid chamber, a poly(methyl methacrylate) (PMMA) ring was glued with polydimethylsiloxane (PDMS) to the PCB top side. After curing the silver epoxy and PDMS at 90°C for 3 h, remaining gaps between neurochip and PCB were sealed with PDMS and cured again.

3.4.2. Platinum electrodes

Electrodes for implantable electric pulse generator

The electrodes were fabricated on common microscopy glass slides that were coated with platinum and an insulating SiO_2 films as follows: the glass slides were consecu-

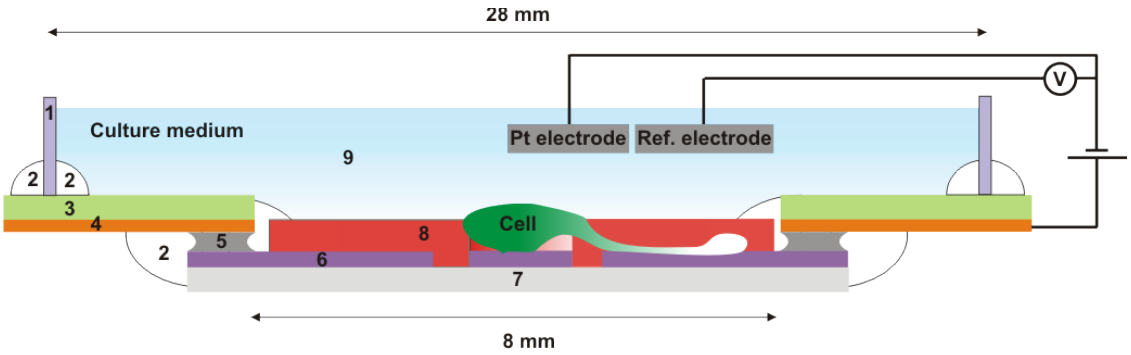

Figure 3.2.: Schematic drawing of the assembled neurochip unit. PMMA ring (1) is glued with PDMS (2) to the printed circuit board (3) to form a liquid chamber for the cell culturing. PCB copper paths (4) are electrically connected with silver epoxy resin (5) to the ITO structure (6) on the SiO_2 substrate (7). PDMS (2) seals the remaining gaps between epoxy silver glue (5) and SU8 structure (8). Platinum and chlorinated silver wires immersed in the culture media serve as counter and reference electrodes, respectively.

tively cleaned in pure acetone, isopropanol, ethanol, water, blow dried with N_2 and then coated with a 10 nm Ti layer as an adhesion promoter followed by a 40 nm Pt layer in an electron beam evaporator (Pfeiffer Classic 500, Wetzler, Germany). One coated slide was then cut into 7 x 2 mm pieces to be used as counter electrodes. The other coated slide was partly protected with Kapton tape (Distrelec, Switzerland), so that the following physical vapor deposition (PVD) SiO_2 coating formed an electrically insulating, 3 mm wide and 100 nm thick SiO_2 strip after removal of the tape. The slide was cut with a diamond saw into individual electrodes. Biocompatible Teflon-coated stainless steel wires (AS632; Cooner Wire, Chatsworth, CA) were connected to the platinum region with silver epoxy glue and cured at 80°C for 1 h. The connection was then coated with EPOTEK-320M (Epoxy Technology, Billerica MA, USA) and cured at 60°C for 6 h to ensure full biocompatibility and electrical insulation of the connection (Fig. 3.3).

Electrodes to test bacterial adhesion under applied currents

The substrate was designed to contain six equal electrodes inside the flow chamber (Appendix A.1). The substrate was fabricated using a microscopy cover slide, that was cleaned for 5 min with Piranha solution (mixture of H_2SO_4 and H_2O_2, used to clean organic residues off substrates), then rinsed with H_2O and blow dried with N_2. The slide was heated on a hot plate at 200°C for 20 min, immediately cooled down to room temperature and then spin coated with ma-N400 photo resist (micro resist, Germany) at 3000 rpm for 30 sec. The slide pre-baked on a hot plate at 100°C

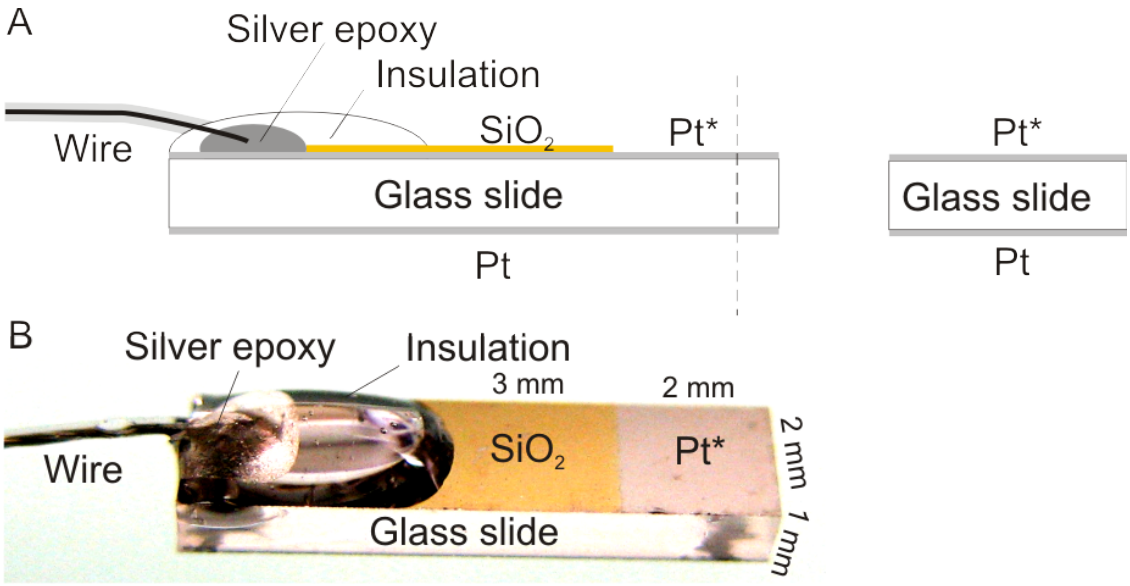

Figure 3.3.: A) Schematics of the electrode and its cross section through the active Pt* electrode. The Pt film on the lower side is not connected to the pulse generator and serves as control Pt surface. B) Photograph of the working electrode connected to the Teflon coated wire leading to the pulse generator.

for 2 min before exposing for 2 min in a Karl Süss X380 mask aligner through a polymer mask. The photoresist was developed in ma-D533/S solution (micro resist, Germany) for 30 sec and rinsed in H_2O. The slide was etched in oxygen plasma for 3 min to remove any polymer residues after the rinsing step and increase the adhesion of the following metal deposition. A thin film of Ti (30 nm) and Pt (40 nm) were deposited subsequently on the slide by physical vapor deposition (PVD) (Pfeiffer Classic 500, Wetzler, Germany). After deposition, the photoresist lift-off was performed in n-methyl-2-pyrrolidone (NMP) and then the slide was cleaned with acetone, isopropanol and blow dried with N_2. A layer of Shipley S1818 photoresist was spin coated over the electrodes to insulate the electrode leads to present a defined 0.2 x 1 mm Pt surface to the artificial urine.

3.5. Cell culturing and staining

3.5.1. C2C12 myoblasts

Cell culture

The myoblasts were cultured in culture media containing D-MEM with 10% FBS and 1% penicillin-streptomycin solution all purchased from Invitrogen (Switzer-

land). The experiments and the cell culturing were performed in the incubator at 37°C and 7% CO_2.

Staining

Dead cells or cells with membrane rupture were stained for 20 min with 2.5 μg propidium iodide (PBS-PI) (Promega, Switzerland) in phosphate buffered saline (PBS, pH 7.4) (Invitrogen, Switzerland), hereafter called PBS-PI. Then cells were fixated in 4% formaldehyde in PBS and counterstained with DAPI (Promega, Switzerland) in order to calculate the percentage of PI positive cells.

Cell exposure to different pH solutions

The following experiment was performed in order to compare the effects on cells of an applied currents and the exposure to different pH solutions. Therefore, different isotonic solutions were made by mixing H_2O and 1 M HCl, both with a physiological amount of NaCl (150 mM), to achieve solutions with pH between 1.2 and 7. M2C12 myoblasts were cultured for 24 h in 24-well polystyrene dishes (NUNC^{TM}) prior to the cell experiment. Then the cells were exposed for 2 min to either the pure pH solutions or the pH solution containing 2.5 μg/ml propidium iodide. Then the cells were treated the same way as explained in the current experiment. The pH solutions with PI were directly incubated in PBS-PI for 20 min before fixation while the cells in pure pH solution had the chance to recover in growth media for 30 min before the PBS-PI incubation and fixation. After the formaldehyde fixation the cells were also stained with DAPI.

3.5.2. NG108 neurons

Cell culture

NG108 neuroblastoma cells (LGC, France) were cultured in a growth medium (DMEM without pyruvate, 10% fetal bovine serum, HAT supplement) at normal cell growth conditions (37°C, 5% CO_2). Once the neurons adhered to the neurochip the culture medium was exchanged to serum free differentiation media (DMEM without pyruvate, HAT supplement, 500 μM dibutyryl cAMP). In all cell culture medium 1% penicillin-streptomycin was used to avoid bacterial growth. All cell culture medium and supplements were bought from Invitrogen, Switzerland.

Staining

At the desired time point of an experiment the cells were fixed with 4% formaldehyde in PBS for 30 min and permeated in PBS (1% BSA, 0.1% Triton X-100) for

30 min. The cells were then stained in 0.13 μg /ml phalloidin for 1 h followed by extensive PBS rinsing.

3.5.3. Rat aortic derived cells

Cell culture

Rat aortic derived cells (RAOC) (kindly provided by Jens Kelm USZ) were proliferated under standard incubator conditions (37°C, 5% CO_2) in endothelial basal medium (EBMTM-2; Cambrex, Walkersville, MD) containing growth factors and supplements, namely vascular endothelial growth factor (VEGF), human fibroblasts growth factor (hFGF), human recombinant long-insulin-like growth factor-1 (R-3-IGF-1), human epidermal growth factor (hEGF), gentamycin and amphotericin (GA-1000), hydrocortisone, heparin, ascorbic acid, and 2% fetal bovine serum (FBS).

Cell viability assay staining

The number of dead cells on the electrodes was visualized by propidium iodide staining (Molecular Probes Inc., Eugene, OR) which is permeant only to dead cells. Hoechst 33342 (Molecular Probes) was used to count the total number of cells as it stains the condensed chromatin of all cells irrespective of membrane integrity.

Caspase-3 and vinculin staining

The type of cell death and the cell adhesion contact size was investigated with immunochemical staining: after exposing the RAOCs to electric current for 24 h, the electrodes were washed in physiological phosphate buffered saline (PBS) solution, then blocked with 0.1 M glycine in PBS for 5 min and permeated for 10 min. in PBS containing 0.2% Triton X-100. After blocking with 5% normal (pre-immune) goat serum and 1% bovine serum albumin in PBS for 30 min, primary antibodies polyclonal cleaved caspase-3 (Asp175), (Cell Signalling Technology, MA) or anti-human vinculin-1 (Sigma, Switzerland) - were added and incubated for 1 h at room temperature then washed in PBS. Fluorescence-labeled secondary antibodies Cy3 anti-mouse or Cy2 anti-rabbit IgG (both from Jackson Immunochemicals, PA) - were diluted in 1% bovine serum albumin (BSA) containing Tris-buffered saline (TBS; 20 mM Tris base, 155 mM NaCl, 2mM ethylene glycol tetra acetic acid, 2 mM magnesium chloride) and sequentially incubated for 1 h at room temperature. All samples were counter stained with DAPI (Molecular Probes Inc., OR) for nuclear localization. Finally, the cells were washed in PBS and mounted in 0.1 M Tris-HCl, pH 9.5, a 3:7 mixture of 0.1 M Tris-HCl (pH 9.5) and glycerol supplemented with 50 mg/ml n-propyl gallate as an anti-fading reagent.

3.5.4. Bacteria

Proteus mirabilis

A concentraded (5x) stock solution was prepared according to Griffith et. al [93] and accordingly diluted in H_2O before starting the QCM-D experiment. Before the flow cell experiment, an aliquot of *Proteus mirabilis* was diluted in 500 ml sterile artificial urine 3.7.3. The aliquot was made by scratching the bacteria from the culture media and suspending in 10 ml phosphate buffered saline (PBS) pH 7.4. The aliquots of 0.5 ml were stored at -20°C.

Life / Dead staining

The life/dead staining solution was a mixture of 16 μg/ml fluorescein diacetate (FDA) and 2 μg/ml propidium iodide solved in PBS. After the experimental time, the flow cell was rinsed with the staining solution for about 5 min before rinsing with PBS and 10 min sample fixation with 1% formaldehyde in PBS. The substrate was blow dried with N_2 and the electrode side was embedded in O.C.T^{TM}Tissue Tek between a cover slide.

3.6. In vivo Experiments

3.6.1. Implantation

A single implant consisting of the pulse generator and three electrodes (Fig. 3.4, A) was implanted in each of the 20 Sprague-Dawley rats obtained from Harlan Laboratories (Horst, Netherlands). All procedures were performed in a laminar flow cabinet under sterile conditions using sterile equipment and standard surgical techniques. Anesthesia was induced by 2.5-5% isofluorane inhalation with 1 l/min oxygen in an enclosed induction box. Once the rat was sufficiently anaesthetized, it was laid in a prone position. Sterile ophthalmic ointment was applied to the eyes of all animals. A custom-made mask was applied to supply continuous oxygen (1 l/min) and isofluorane (2.5-5%) as necessary to maintain adequate anesthesia throughout the procedure. The level of anesthesia was monitored by observing breathing rate, heart rate and color of mucous membranes. The dorsal implantation area was prepared for surgery by shaving off all fur from the nape of the neck to the mid back, and the skin disinfected with Kodan. A dorsal, midline, transcutaneous incision was then made to allow implantation of the electrodes (Fig. 3.4, B-D) show the three electrodes placed approximately 5 mm apart in distended pockets in the fascial plane created by blunt dissection and individually secured with a single stay suture (6.0 gauge polyamide, Ethicon). The counter electrode in each system was implanted between the two working anodes, and the pulse generator

was placed a minimum of 5 cm away from the electrodes. The incision was then closed (Fig.3.4, D) with non-absorbable sutures (4.0 gauge polyamide, Braun). 0.05 mg/kg Buprenorphine (Temgesic) for post-operative analgesia was routinely given subcutaneously at the end of each procedure. A second dose was administered 12 h later as clinically needed. The rats were then placed individually in clean cages with a heat pad for post-operative monitoring and allowed to recover. All rats tolerated the surgery well and were monitored daily until the study endpoint.

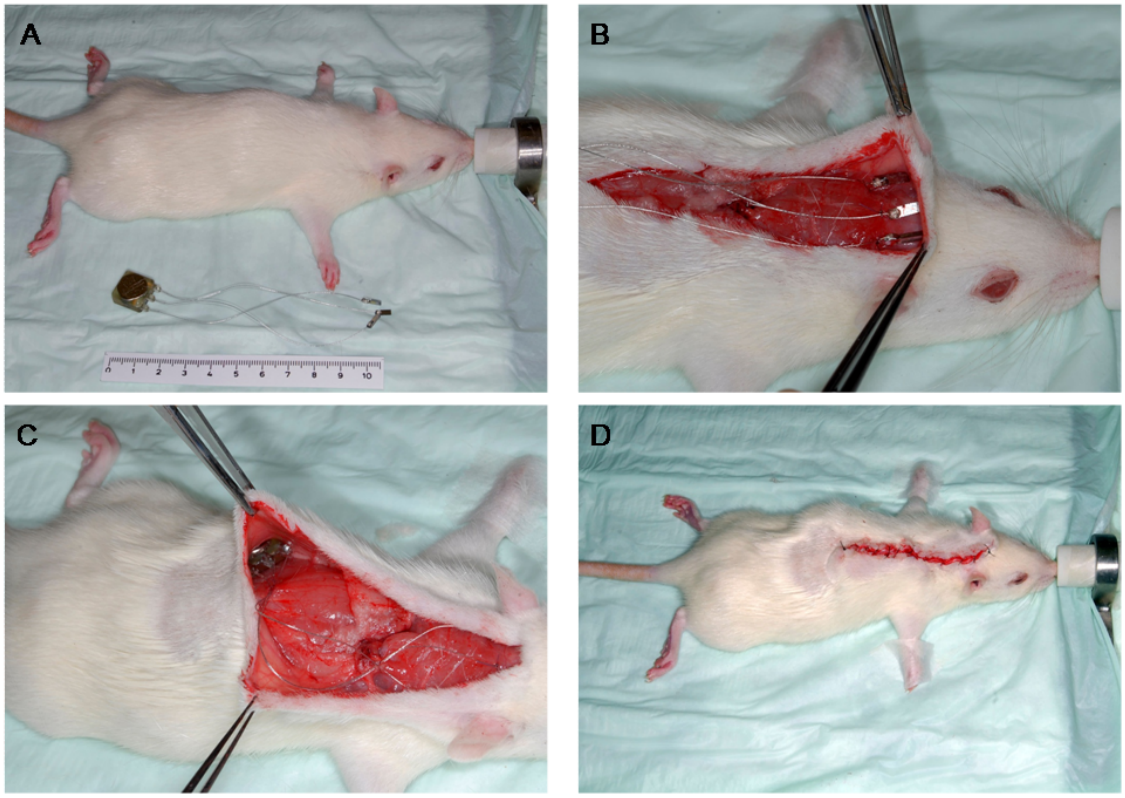

Figure 3.4.: (A) Operative procedure to subcutaneously implant electrodes and current pulse generator in a rat. The relative size and position of the implant is shown. (B) A dorsal transcutaneous incision and distended pockets were made to allow implantation. The electrodes were secured in position by a stay suture around 5 mm apart. (C) The pulse generator was placed subcutaneously at least 5 cm away from the electrodes. (D) The wound was closed by non-absorbable sutures.

3.6.2. Histology and staining

The rat heads with the implanted electrodes were put in 4% formaldehyde for fixation at 4°C. The solution was exchanged daily during one week. After x-ray imaging to assure the position of the electrodes, the skull was separated from the neck with the electrodes to minimize the tissue amount for embedding. The neck was then rinsed with H_2O 3 x for 30 min. The tissue was dehydrated in a watery solution with increasing ethanol content 50% 90 min, 70% 24 h, 80% 24 h, 90% 12 h, 96% 12 h, 100% 96 h, then the sample was stored in Xylene for 4 days. Then the tissue was embedded in PMMA by placing the sample into a small Tupperware container and filled with the PMMA precursor mixture 89.5% methyl methacrylate MMA (Fluka Chemie, Switzerland), 10% dibutyl phthalate DBP (Merck, Germany), 0.5% di(4-tert-butylcyclohexyl) peroxydicarbonate Perkadox 16 (Dr. Grogg Chemie, Switzerland). The polymerization in a vacuum at 4°C to avoid any bubble formation was finished after 7 days. The block was then cut into 0.6 mm slices with a saw microtome Leica SP1600 and glued on acrylic glass carrier for polishing on a Planopol V (Struers, Denmark) with decreasing grain size. The polished slice was then 4 min etched in 0.7% formic acid and blow dried before staining for 20 min in 1% toluidine blue solution.

3.7. Buffers and solutions

3.7.1. Fluorescent measurement and standard solutions for pH measurement

The pH sensitivity of fluorescent dyes is known and can be used to visualize local pH changes [94]. The following protocol has been optimized for measurements in the range between pH 2-7. An indicator stock solution was made from 20 μmol 5(6)-carboxyeosin (CE) and 20 μmol fluorescein sodium salt (FITC) in a mixture of 500 μl H_2O and 500 μl dimethyl sulfoxide, all purchased from Sigma-Aldrich (Switzerland). The stock solution was diluted 1:2000 to a final concentration of 10 μM CE and 10 μM FITC for all measurements. The electrochemically induced pH change was measured only in H_2O, whereby the ohmic resistance was lowered by adding NaCl to a final concentration of 150 mM. 0.2 M $Na_2HPO_4 \bullet 2H_2O$ and 0.1 M citric acid solutions were made according to the mixing table proposed by McIlvaine [95] in order to get a buffered standard solutions.

3.7.2. PLL-g-PEG, PLL coating solutions

The protein and cell resistant coating solution was made by dissolving 0.1 mg/ml poly(L-lysine)-*grafted*-poly(ethylene glycol), PLL(20)-$_g$[3.5]-PEG(2), (Surface Solutions, Switzerland) in 10 mM HEPES buffer, pH 7.4 with 150 mM NaCl [96].

The annotation PLL(20)-*g*[3.5]-PEG(2)) refers to poly(L-lysine) backbone of molecular weight 20 kDa, a grafting ratio of lysine-mer/PEG side-chain of 3.5 and poly(ethylene glycol) side chains of molecular weight of 2 kDa. PLL-*g*-PEG, a polycationic copolymer adsorbs spontaneously from aqueous solutions onto negatively charged surfaces [96]. It forms a monolayer on the surface with densely packed PEG chains, which is repulsive for any proteins that normally adsorb onto surfaces. Besides providing a stable protein resistant coating it can be removed electrically by applying a potential [90, 97, 98].

The cell adhesive coating was made by dissolving 0.1 mg/ml poly(L-lysine) (PLL) $M_w > 70kDa$ (Sigma Aldrich, Switzerland) in 10 mM HEPES buffer, pH 7.4, 150 mM NaCl.

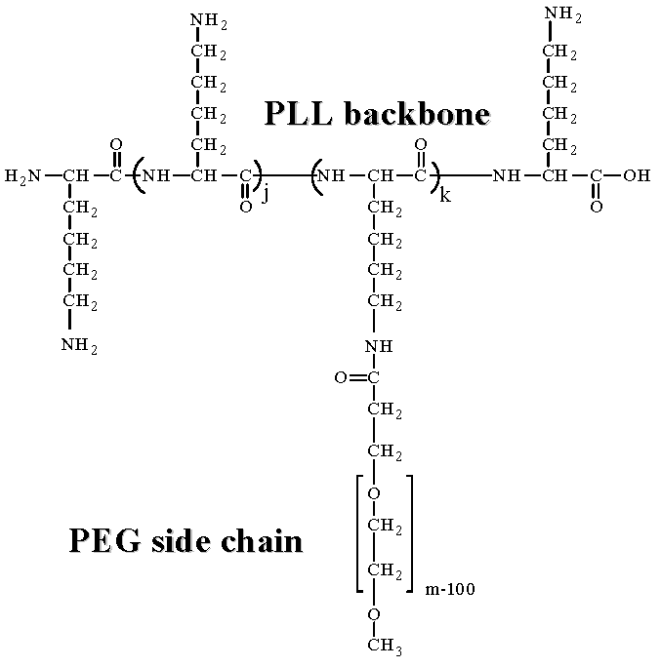

Figure 3.5.: Chemical structure of the poly(L-lysine)-*grafted*-poly(ethylene glycol)(PLL-*g*-PEG). The molecule consists of PEG side-chains which are grafted onto the positively charged PLL backbone chain.

3.7.3. Artificial urine

A concentraded (5x) stock solution was prepared mixing the ingredients listed below, except tryptone soya broth, according to Griffith et. al [93]. The stock solution was autoclaved and stored at room temperature. Before using the urine, the stock solution was diluted in sterile H_2O and the soya broth was added. The pH was corrected to 6.1 by adding 3 M HCl or 3 M NaOH solution, respectively.

The different ingredients and concentrations for the artificial urine (final concentration) are listed below:

- calcium chloride (0,49 g/l)
- magnesium chloride hexahydrate (0,65 g/l)
- sodium chloride (4,6 g/l)
- disodium sulphate (x10 H_2O) (5,2 g/l)
- trisodium citrate dihydrate (0,65 g/l)
- disodium oxalate (0,02 g/l)
- sodium dihydrogen phosphate (2,8 g/l)
- potassium chloride (1,6 g/l)
- ammonium chloride (1,0 g/l)
- urea (25 g/l)
- gelatin (5,0 g/l)
- Tryptone soya broth (Oxoid) (1,0 g/l) (added after sterilization)

3.7.4. pH modelling

Diffusion model

The ITO electrodes used to electrically induce pH change had a length of 8 mm and width of only 30 μm and as such can be considered as a line source in an infinite volume. Hence, the perpendicular cross section of this symmetric system is equivalent to a point source in an infinite plane. Equation 3.3 gives the concentration at a distance r from a point source [99]. In our experiments a constant current was applied producing diffusing substances continuously in a semi-infinite plane due to the perpetual electrochemical reactions on the electrode surface. Such an experimental system can be described by equation 3.4, which is deduced by integrating equation 3.3 with respect to time and replacing the amount of diffusing substance M by a flux F.

$$C(r,t) = \frac{M}{4\pi Dt} e^{(-r^2/4Dt)} + C_0 \tag{3.3}$$

$$C(r,t) = \int_0^t \frac{\phi}{4\pi \mathrm{Dt'}} \mathrm{e}^{(-\mathrm{r}^2/4\mathrm{Dt'})}\, \mathrm{d}t' = \frac{2I}{4\pi DFl} E_1\left(\frac{r^2}{(4Dt)}\right) + C_1 \tag{3.4}$$

- $C(r,t)$: $[molm^{-3}]$ is the concentration of substance
- M: $[molm^{-1}]$ amount of diffusing substance deposited initially at the point source
- D: $[m^2s^{-1}]$ diffusion coefficient of the substance in the solution
- r: $[m]$ distance from the point source
- t: $[s]$ time
- C_0, C_1: $[molm^{-3}]$ is the initial concentration of substance
- ϕ: $[mols^{-1}\ m^{-1}]$ flux of substance per unit length

$$\phi = \frac{2I}{Fl}$$

for a semi-infinite plane

- I: $[A]$ current
- F: $[Cmol^{-1}]$ Faraday constant
- l: $[m]$ length of the electrode
- E_1: exponential integral

$$E_1(x) = \int_1^\infty \frac{e^{-kx}}{k}, \mathrm{d}k$$

The measured pH values (Fig. 4.3) correspond to the concentration $C(r,t)$ in equation 3.4. We fitted all curves with the same parameters I and D at different time points (t) and distances from the electrode (r) by a least squares method to obtain the parameters I_{fit} and D_{fit}. I_{real} is the amount of protons generated if the electrolysis has a yield of 100%. D_{proton}=D_{real}=9.310310·1010^{-9} m^2/s is the value taken from literature [100].

Modelling the pH in the gap between a adhered cell and electrode surface

The pH around an electrode in bulk solution and between cell and electrode was calculated by a 2D finite element method (COMSOL, Multiphysics®) in the gap between a hypothetical surface attached cell and a flat electrode of the same size (Fig. 3.6). The gap between the cell and the electrode was assumed to be 100 nm [101]. The finite element mesh size was refined and the end boundary of the free space was set far enough (1 mm) with diffusive boundary condition so the results did not depend on calculation condition.

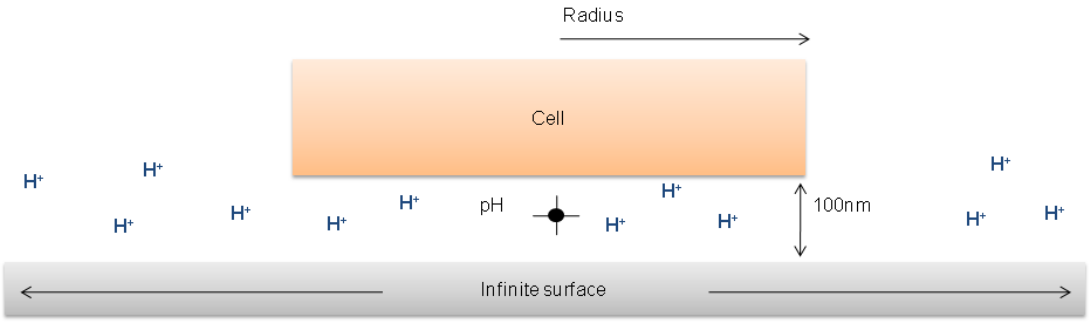

Figure 3.6.: Schematic representation of the hypothetical cell attached on an infinite surface to calculate the range of electrochemically generated pH in the geometric center between cell and surface.

4. Influence of applied constant currents on the viability of cells close to microelectrodes

Electrodes have become more and more popular in biomedical and bioengineering applications, where they are mostly used to apply/measure potentials or currents to/from biological systems. Under such conditions, electrochemical reactions commonly occur at the electrode surface as explained in section 1.5.2. We were interested to measure the turnover of the electrochemical reaction at the electrode interface [61, 102] and applying a model to estimate current densities and their effects on biological samples. In this chapter, we the aim to better describe these processes. We applied constant currents using transparent indium tin oxide microelectrodes to induce a local change in pH, associated with electrolysis. The pH change was monitored optically within the first lateral 170 μm vicinity using microscopy and a pH sensitive fluorescent dye combination as indicator. The data was then fitted with a simple diffusion model [99]. The effect of such an induced pH change was also assessed by measuring the desorption of a cationic polyelectrolyte (poly(L-lysine)-*grafted*-poly(ethylene glycol) as a function of the local pH [96, 103]. Since this polymer interacts electrostatically with surfaces in a pH dependent manner, we could show a strong effect in unbuffered solutions while buffered solutions restricted the electrochemically induced pH change below the optical resolution of the microscope. The effect of applied current on the behavior of cells was also studied on myoblast directly cultured on the microelectrodes. We have found that current densities larger than 0.57 A/m^2 induced cell death within 2 min of exposure. Based on our model we could attribute this to the change in local pH although the effect of other electrochemically created reactive molecules could not be excluded [104–106].

4.1. Direct measurement of electrochemically induced pH change with fluorescent dyes

4.1.1. Experiments on visualizing pH change

NaCl is the most prevalent electrolyte besides other inorganic salts, amino acids and vitamins in cell culture media as well as in animal body fluids. The following experiments were all performed in physiological aqueous solution either with 150 mM NaCl added to lower the ohmic resistance or 107 mM NaCl already contained in the commercially available culture media for cell experiments. The experiment was carried out using the ITO substrates (Fig. 3.4.1, Appendix A.1) in the flow cell under constant current controlled by an Autolab potentiostat PGSTAT302N (Potentiostat) in a 3-electrode set-up.

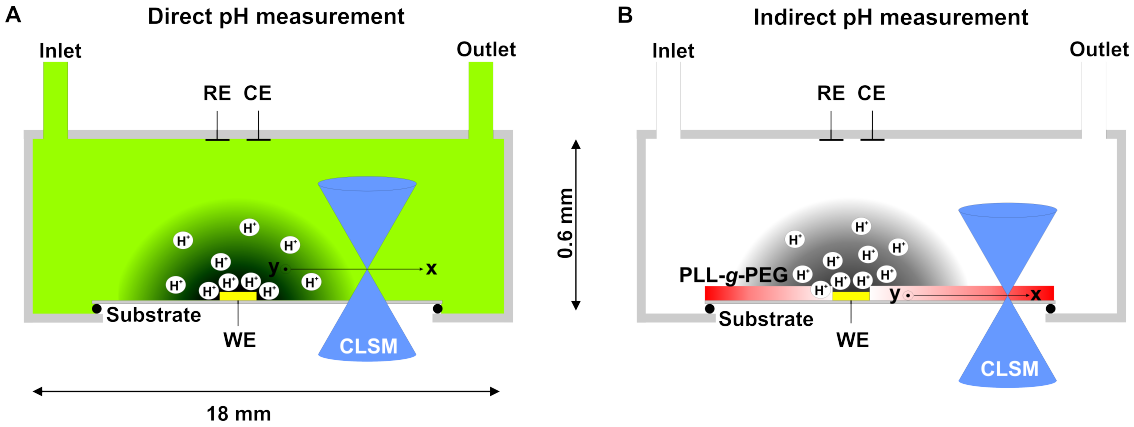

Figure 4.1.: Schematics of the flow cells used for pH and desorption measurements. The transparent substrate contains the indium tin oxide working electrode (WE) while the reference (RE) and counter electrodes (CE) are integrated in the top part. (A) Direct pH measurement: The flow cell is filled with a pH indicator solution and the focus of the CLSM is set to 10 μm above the substrate surface. Changes in fluorescence intensity provide information about the local pH. (B) Indirect pH measurement: the substrate is fully coated with fluorescently labeled PLL-*g*-PEG (red). The CLSM focus is in-plane with the PLL-*g*-PEG monolayer. The measured fluorescent PLL-*g*-PEG desorption is indicating the local pH changes.

A standard curve was made to relate the fluorescence intensity of the indicator dye to the electrochemically induced pH. Therefore phosphate citrate buffered pH standard solutions were made according to the mixing table proposed by McIlvaine (Section 3.7.1) and the indicator dye mixture was added. The flow cell was then

filled with these standard pH solutions and xy-plane images were taken 10 μm above the surface of the substrate (Fig. 4.1). The dyes were excited simultaneously at 488 and 514 nm and their fluorescence emission was detected using a band-pass filter 530-600 nm and confocal microscopy as described (Section 3.1.2). The fluorescent intensity was averaged over the entire image and the resulting fluorescence versus pH plot was fitted by a fifth order polynomial equation to obtain a standard curve (Fig. 4.2). The flow cell was then filled with water containing the indicator mixture and 150 mM NaCl at pH 6.6. Then a current of 4 A/m^2 was applied to the electrode while imaging the xy-plane with the CLSM (Fig. 4.1). The measured fluorescence intensity of the indicator could then be related with a standard curve (Fig. 4.2) to the local pH with a temporal resolution of 250 ms per scanned line.

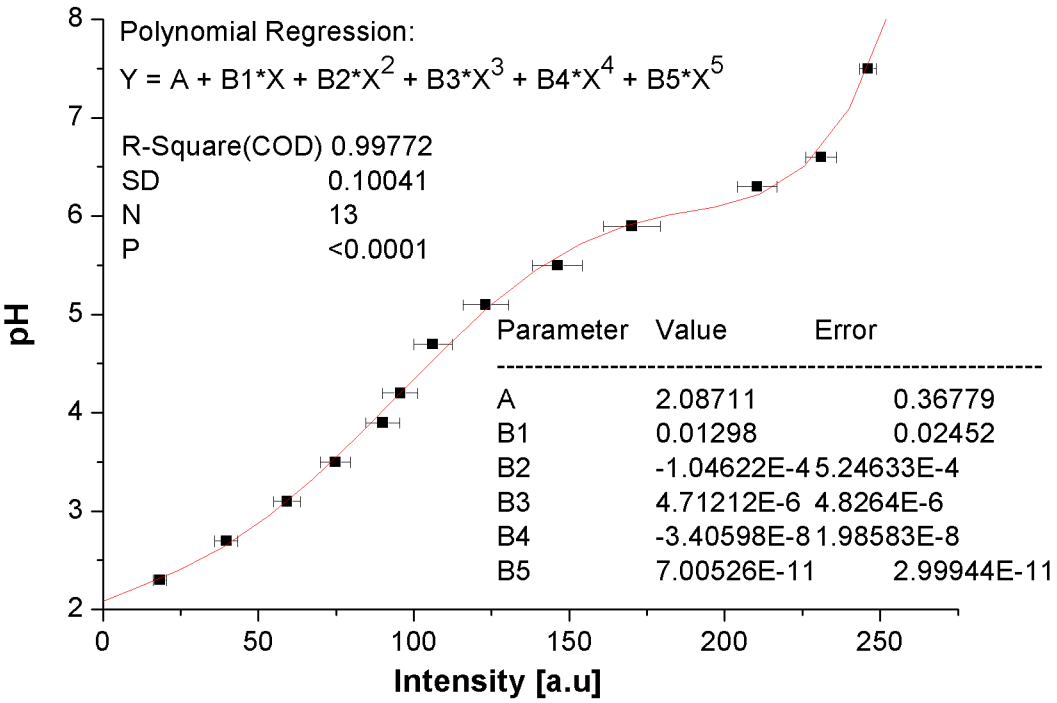

Figure 4.2.: The plot shows the standard curve for the measured fluorescence intensity of the fluorescent dye mixture of 10 μM CE and 10 μM FITC vs. pH. The indicator dye stock solution was therefore pipetted into standard buffered solutions and then all were measured with the same settings on a confocal laser scanning microscope.

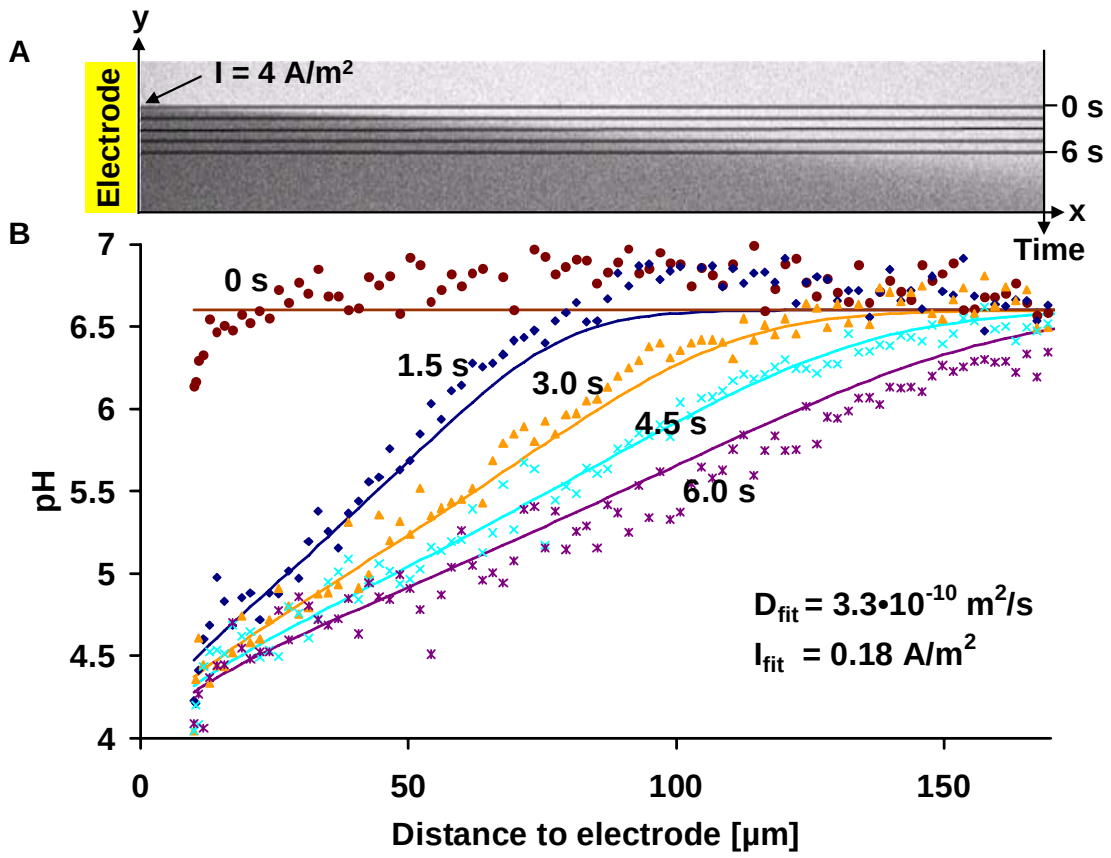

Figure 4.3.: (A) Confocal laser scanning microscopy image of the solution adjacent to the ITO electrode is shown. The focus was set to 10 μm above the surface. About 8 s after the scanning of the xy plane was initiated, a current of 4 A/m^2 was applied and the progression of the electrically induced pH change was monitored by the darkening of the indicator dyes. (B) The corresponding pH progression (symbols) in H_2O vs. electrode distance in steps of 1.5 s along with the fitted data (lines). The scaling along the x-axis is equivalent for (A) and (B).

4.1.2. Results on visualizing pH change

The measured results and the corresponding fits are presented and compared to the theoretically expected pH. Acquiring a typical CLSM image using our settings takes about 20 s by scanning the laser line by line from the top towards the bottom of the image. Thus figure 4.3, A represents the time evolution since our sample is homogenous in the Y direction (note secondary axis of figure 4.3, A). The induced pH progression is then visualized by bright pixels indicating high pH and darker pixels indicating low pH regions. About 8 s after the scanning started (indicated

by the arrow in figure 4.3, A) a current of 4 A/m^2 was applied. The brightness values were converted to the corresponding pH values (Fig. 4.3, B, symbols) using the standard curve (Fig. 4.2). Already 1.5 s after the current is applied the regions close to the electrode became darker immediately indicating a local drop in the pH to 4.5 within 50 μm distance from the electrode due to electrochemical proton generation. The local pH at the electrode becomes stable afterwards and its value depends only on the applied current. Due to the diffusion of the H^+ ions the pH change gradually extends into the solution. The slopes of the pH curves are decreasing with time, reaching after 6 s a quasi stable pH value, at least within a distance of 170 μm from the electrode (Fig. 4.3, B). After 6 s the curves do not change significantly (data not shown). A least squares method was used to fit the presented five pH progression curves using equation 3.4 with two uniform fitting parameters: current I_{fit} and diffusion coefficient D_{fit}. Although a good qualitative agreement was found, the obtained I_{fit} value was about 44 times smaller than the applied current I = 4 A/m^2 and D_{fit} about 27 times smaller than the theoretical value $D_{proton} = 9.310 \cdot 10^{-9}$ m^2/s [100] for protons in water at infinite dilution.

We overcame the difficulties of a fast pH measurement in small scale by using an indicator solution and the detection of its pH dependent fluorescence with confocal laser scanning microscopy. The indicator solution contained carboxyeosin and fluorescein. The two dyes have similar excitation and emission maxima but different pK_a values, so that their change in fluorescent intensity occurs at different pH values. Using both dyes together in the same solution, a broader pH range pH 2-7 could be measured compared to using only a single dye. The experimental setup is visualized in figure 4.1, B and shows the flow cell filled with the indicator solution. The protons diffuse immediately into the solution after the current is applied. The pH curves shown in figure 4.3, B were all fitted with the same parameters at different times and distances with equation 3.4, which delivered a single value for the current I_{fit} that is 44 times smaller than the current applied in the experiment. We attribute this unexpectedly low efficiency of the electrochemical reaction to other reactions occurring at the electrode: Since NaCl is present in the solution, also Cl_2 is produced at the anode (see reaction 1.4 in the section 1.5). The Cl_2 dissociates into protons, chloride ions and hypochloric acid according to reaction 4.1 but is only moderately soluble in H_2O.

$$Cl_2 + H_2O \longleftrightarrow H^+ + Cl^- + HClO \tag{4.1}$$

The equilibrium of reaction 4.1 is pH dependant. At low pH the reaction towards the left side is more pronounced. Gas bubble formation has not been observed in our experiments with current densities I = 4 A/m^2, which is consistent with the reported gas bubble formation at current densities I = 10-50 A/m^2 [102]. Hence, the majority of the Cl_2 might be physically solved in the buffers and only a small amount dissociated to produce detectable protons. Another reason for the low

current efficiency could be the relatively large amount of indicator dyes (40 μM) present in the solution acting itself as a buffer or the buffering effect of the inevitable dissolution of CO_2 from the environment. A 27 times smaller proton diffusion coefficient than expected was found by fitting the pH values in dilute unbuffered solution. The proton current must be therefore restricted by chemical reactions e.g. with the indicator dye. The fitted parameters (D_{fit}, I_{fit}) as well as the theoretical parameters (D_{proton} , I) were used to calculate the prevalent pH value close to the electrode. The calculated pH values only showed a marginal difference and as such we believe our model describes the real pH value at the electrode with reasonably good (i.e. $\sim$0.4 pH unit) accuracy. The slope of the pH curve is slowly decreasing also after the 6 s time interval investigated, a stable pH value is reached due to the effect of OH^- ions diffusing from the counter electrode (Section 1.5, reaction 1.1). The neutralization reaction between H^+ and OH^- ions then leads to a quasi stable pH gradient between the two electrodes.

4.2. Indirect measurement of electrochemically induced pH change with an indicator molecule

4.2.1. Experiments on visualizing indirectly pH change

In this experiment an electrostatically adsorbed polyelectrolyte is used as an indicator for the pH change in the vicinity of the electrode. 0.1 mg/ml rhodamine labeled (PLL-*g*-PEG) was dissolved in different concentrations of McIlvaine buffer solutions pH 6.6 1:1 (145.5 mM Na_2HPO_4, 27.3 mM citric acid, 150 mM NaCl) and 1:10 (14.55 mM Na_2HPO_4, 2.73 mM citric acid, 150 mM NaCl), respectively. The substrate with ITO electrodes was cleaned with pure ethanol, rinsed with H_2O and blow dried with N_2. The flow cell described above was assembled and O_2 plasma treated for 2 min (Harrick Plasma, USA). The labeled polyelectrolyte solution was then injected immediately into the chamber and incubated for 30 min followed by rinsing with the buffer solution selected for the measurement. The rhodamine labeled PLL-*g*-PEG was excited with 561 nm laser and detected using a 575 nm long pass filter. A rectangular reference region was photo-bleached in the rhodamine labeled PLL-*g*-PEG monolayer (Fig. 4.4, A) and an image was taken before applying the current. A second image was taken after the current I = 4 A/m^2 was applied for 30 s. The relative intensity of the PLL-*g*-PEG monolayer was compared between these two images (by subtracting the average intensity value of the bleached area from the average intensity of 100 lines in the y-direction) (Fig. 4.4, B). The experiment was performed with different media: H_2O, McIlvaine buffer 1:10 and McIlvaine buffer 1:1 for testing the influence of the buffer concentration.

4.2.2. Results on visualizing indirectly pH change

The substrate with the ITO electrode was coated with rhodamine labeled PLL-*g*-PEG (Fig. 4.1, B, top) then a background reference area was bleached into the adsorbed monolayer. The same current density I = 4 A/m^2 as in the previous experiment was applied to the electrode. After 30 s a dark region close to the electrode was observed indicating desorption of the electrostatically adsorbed PLL-*g*-PEG (Fig. 4.1, A, bottom) in the darkened region close to the electrode. The amount of PLL-*g*-PEG desorbed within 30 s was gradually decreasing from the electrode: from about 50% observed close to the electrode to no desorption at about 20 μm distance from the electrode in H_2O. 1:10 McIlvaine buffer reduced the extent of pH change to 5-10 μm whereas no change in the image was observed in the undiluted McIlvaine buffer indicating that the extent of detectable pH change is below the resolution of confocal laser scanning microscopy (Fig. 4.4, B). The pH in vicinity to the electrode was calculated with equation 3.4 and also with a finite element method (see section 3.7.4,3.7.4) using the same parameters. Both methods showed a similar pH range in H_2O vs. distance to the electrode, however, only the results of the FEM method are shown in figure 4.4, C. In the previous section, we found a large difference between the expected D_{proton} and the fitted values for I and D. Therefore, we decided to use both parameter pairs to estimate the pH changes in this arrangement. The pH range reached in the time between 10-30 s is shown in figure 4.4 C for the fitted parameters (grey) $D_{fit} = 3.3{\cdot}10^{-10}$ m^2/s $I_{fit} = 0.09$ A/m^2 and the theoretical parameters (turquoise) D = $9.3{\cdot}10^{-9}$ m^2/s, I = 4 A/m^2. Despite the difference between the two parameter sets, the calculated pH values and slopes were very similar (ΔpH $\sim$ 0.4) close to the electrode.

The used polyelectrolyte, PLL-*g*-PEG, is highly cationic at physiological pH and adsorbs electrostatically onto negatively charged surfaces. The strength of its interaction with the surface depends on the pH or the ionic strength of the solution which makes the molecule an indirect indicator for pH changes. The PLL-*g*-PEG adsorption occurs between the isoelectric point of the SiO_2 surface and the pKa of the poly(L-lysine) showing the strongest binding at pH 8 [96]. However, as soon as the local pH is unfavorable, i.e. lower than pH 5 or the local ionic strength is higher than physiological, we expect desorption of PLL-*g*-PEG from the SiO_2 [103]. Thus, the observed loss of PLL-*g*-PEG at the calculated range pH 3.8-4.2 is in accordance to the literature. However, this change in pH and local ionic strength might not be the only explanation for the observed desorption. If we consider the finding from the previous experiment that a large amount of Cl_2 might be produced at the electrode, some hypochloric acid is produced according to reaction 4.1. The produced HClO can react with the amines of the lysine side chains to form monochloramines (-RNHCl derivatives) as described by Grisham et al. (Reaction 4.2 and 4.3) [104, 105].

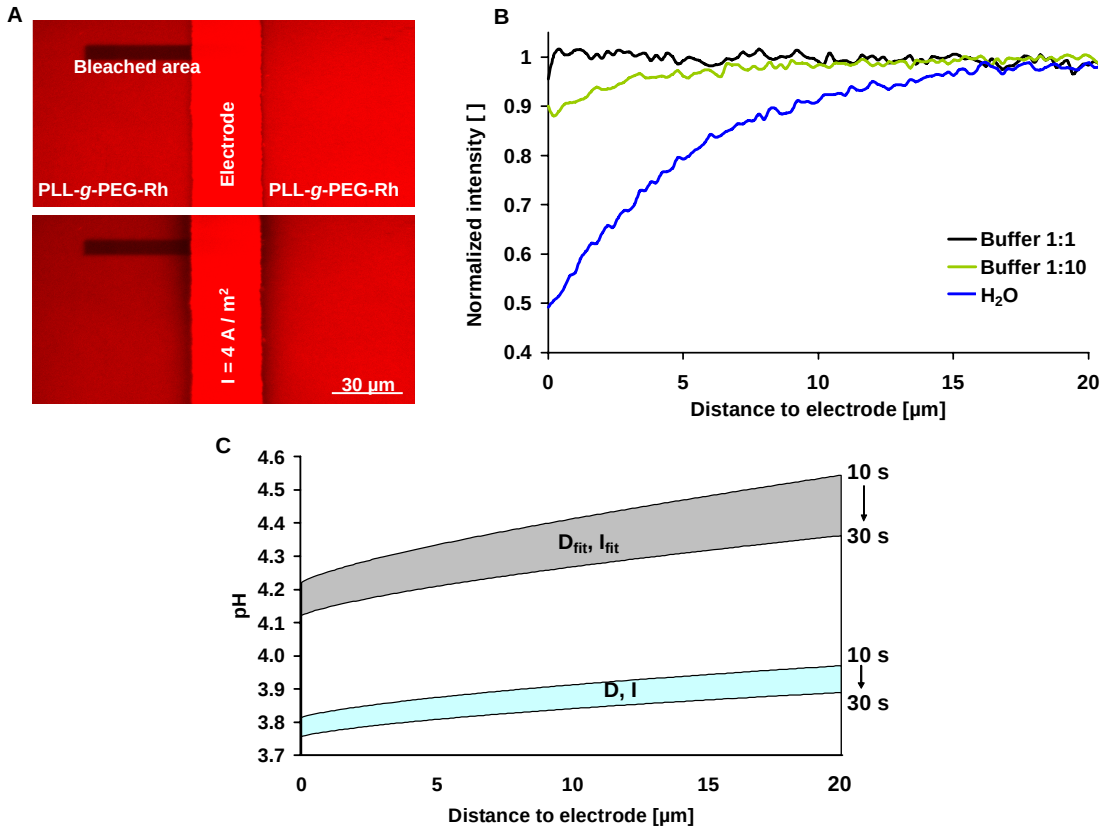

Figure 4.4.: (A) Rhodamine labeled PLL-*g*-PEG monolayer with a bleached region as reference before (top) and after (bottom) a current of 4 A/m^2 was applied to the ITO working electrode (WE) for 30 s. (B) Amount of labeled PLL-*g*-PEG measured by the normalized fluorescent intensity as a function of distance from the electrode in H_2O, McIlvaines buffer 1:10 and McIlvaines buffer 1:1, respectively. (C) Modeled pH in H_2O vs. distance to the electrode with the fitted parameters $D_{fit} = 3.3{\cdot}10^{-10}$ m^2/s, $I_{fit} = 0.18$ A/m^2 and theoretical parameters D = $9{\cdot}10^{-9}$ m^2/s, I = 4 A/m^2 for the time-range between 10 and 30 s.

$$RNH_3^+ \longleftrightarrow RNH_2 + H^+ \tag{4.2}$$

$$HClO + RNH_2 \longleftrightarrow H_2O + RNHCl \tag{4.3}$$

Chloramines decompose to nitrogen-centered radicals or carbonyl groups. The formation of carbonyl groups accounts for $\ll$10% of the added HClO. Such a process may be biologically significant, since carbonyl can crosslink with free amine groups via Schiff-base formation [106] a process that might also account for the recent

finding of Ngankam et al. on the continuous adsorption of poly(L-lysine) under an applied potential [107]. The relevance of this reaction to our system is the following: PLL-*g*-PEG side groups could intra- or inter-molecular crosslink and, therefore, lose their charge. Consequently their ability to electrostatically adsorb on a surface is lost. Therefore, we consider the electrochemically induced pH change and the formation of HClO to be the main reasons for the PLL-*g*-PEG desorption. The effect is not limited to the PLL-*g*-PEG molecule. Other electrostatically adsorbed poly-electrolytes, poly-electrolyte multilayers, or proteins show similar behavior [108, 109].

4.3. Effects of electrochemically induced pH change to viable cells

4.3.1. Experiments on viable cells with induced pH change

The following experiments were conducted to evaluate the effect of an applied current on the behavior of cells grown directly on the electrode: C2C12 myoblasts were therefore cultured on MEA60 200 biochips (Appendix A.6). After cleaning the surface, the chip was coated with 0.1 mg/ml poly-L-lysine ($M_w \geq 300$ kDa, Sigma-Aldrich, Switzerland) in PBS buffer for 30 min and rinsed with PBS. After trypsinizing myoblasts, the suspended cells were transferred to the chip and formed a confluent layer within 24 hours. The culture media was then exchanged to either a phosphate buffered saline (PBS, pH 7.4) (Invitrogen, Switzerland) or PBS with 2.5 μg propidium iodide (PBS-PI) (Promega, Switzerland). The MEA chip was mounted to a MEA1060 interface (Appendix A.5). A simple platinum wire dipped into the solution served as a counter electrode and a chlorinated silver wire as a reference electrode. The whole setup was put in a cell culture incubator and connected to the potentiostat. Different currents up to 2 A/m^2 were then applied for 2 min on 5 individual electrodes to cells in PBS or PBS-PI, respectively. (Currents higher than 8 A/m^2 resulted in electrode break-down in our setup). Cells treated in PBS-PI remained in PBS-PI for totally 20 min before fixation in 4% formaldehyde in PBS. The cells in PBS had the chance to recover from the treatment by incubating in growth media for 30 min, before the growth media was changed to PBS-PI for totally 20 min followed by the fixation. In order to calculate the percentage of PI positive cells, all cells were counterstained with DAPI (Promega, Switzerland). A similar experiment was performed in order to compare the effects on cells of an applied currents and the exposure to different pH solutions. Therefore, different isotonic solutions were made by mixing H_2O and 1 M HCl, both with a physiological amount of NaCl (150 mM), to achieve solutions with pH between 1.2 and 7. M2C12 myoblasts were cultured for 24 h in 24-well polystyrene dishes (NUNC^{TM}) prior to the cell experiment. Then the cells were exposed for 2 min to either the pure pH

solutions or the pH solution containing 2.5 μg/ml propidium iodide. Then the cells were treated the same way as explained in the current experiment. The pH solutions with PI were directly incubated in PBS-PI for 20 min before fixation while the cells in pure pH solution had the chance to recover in growth media for 30 min before the PBS-PI incubation and fixation. After the formaldehyde fixation the cells were also stained with DAPI.

4.3.2. Results on viable cells with induced pH change

The previous sections have shown the possibility to measure and model the pH change close to electrodes. The physiological effects of such a pH change close to viable cells were studied on myoblasts cultured directly on transparent electrodes. Different current densities were therefore applied to the electrodes for 2 min and the amount of dead cells was visualized by propidium iodide (Fig. 3.5.1).

Figures 4.5, A_1-B_2 show differential interference contrast (DIC) microscopy images of a confluent myoblasts layer on the MEA60 ITO 200 chip superimposed on with the corresponding PI fluorescence signal (red). The ITO electrodes appear a bit darker than the underlying glass substrate and are labeled with the applied current density. During the current exposure the cells in figure 4.5, A_1, B_1 were immersed in PBS whereas the cells in figure 4.5, B_1, B_2 were immersed in PBS-PI. The cells immersed in PBS showed no substantial cell death up to the current density of 0.57 A/m^2, while the cells in PBS-PI already showed an increased amount (40 %) of PI positive cells at this current. (See middle electrode in figure 4.5, B_2.) Higher current density increased the amount of PI positive cells in both cases. The percentage of PI positive cells was calculated with respect to the DAPI stained nuclei and is plotted versus the applied current density in figure 4.5, C. A voltammogram of the electrode versus an Ag|AgCl reference electrode is presented in figure 4.5, D. The magnified plot shows the onset of the curve and the red zone indicates the current range where the cells were killed in larger amounts. The whole cyclic voltammogram is provided as an inset.

The PI staining experiment presented at the end of the results section revealed PI positive cells at current densities higher than 0.57 A/m^2 (see figure 4.5, $B_{1,2}$). This either indicates that PI becomes cytotoxic or cell membrane permeant by electrochemical modification or, which is more likely, cell membrane pore formation or membrane rupture occurs due to the change in local pH and the production of reactive molecules in the gap between the electrode and the cells. In order to investigate whether the local pH could be responsible for the observed effect we have modeled the situation by a 2D finite element method described in the methods and materials section. We assumed a hypothetical surface attached cell (rectangular box 30x10 μm) and a flat electrode of the same size (30 μm). The gap between the cell and the electrode was assumed to be the same as the distance (100 nm) (Section 3.7.4). The calculation gave similar pH values for both parameter sets:

pH 2.9 (I_{fit} = 0.032 A/m^2, D_{fit} = 3.3·10^{-10} m^2/s and pH 3.2 (I_{real} = 0.64 A/m^2, D_{Proton} = 9.3·10^{-9} m^2/s). These pH values were reached already after 0.5 s and did not change during the simulated time of 2 min. These calculated values were compared to a control experiment where we checked the pH resistance of myoblasts towards different pH solutions. There, an increasing amount of PI positive cells at pH 4 was observed. All cells were PI positive at pH 2 (see figure 4.6). This means that the electrochemically induced pH change in the gap alone could explain the observed cell killing on the electrode. Besides the local pH the cytotoxic effect of the electrically induced species, such as 50 μM HClO could also account for the observed cell killing [105]. Therefore, although we found a current threshold that induces cell death or the opening of membrane pores which leads to PI uptake within 2 min, the reason (i.e. either pH change or the formation of reactive molecules) remains unclear.

4.4. Summary

In this chapter we have presented two methods that can be used to visualize the electrochemically induced pH changes close to a microelectrode. The first method is based on pH dependant fluorescent dyes in solution, while the second uses the induced desorption of an electrostatically adsorbed polyelectrolyte for the quantification of the process. These methods allowed us to monitor the pH progression close to the electrode and a simple model could be fitted to the data. The effect of a locally applied current on the behavior of myoblasts has also been studied. We have found that currents larger than 0.57 A/m^2 induced cell death or propidium iodide uptake due to membrane pore formation within 2 min of exposure. We could attribute this to the change in local pH although the effect of other electrochemically created reactive molecules could not be excluded. This presented approach could be used in different areas of applications where locally restricted pH change is important. For example, the system can be used for the local synthesis of short peptides [110] or sol-gel thin film deposition [111]. Another advantage of this system is that the extent of the local pH change can be restricted also to the submicrometer range using buffered solutions. This is highly important in applications where cells are cultured close to the electrodes and should not be affected by electrochemically induced pH changes. The same effect could also be used to release drugs from pH sensitive polyelectrolyte multilayers or gels and facilitate the uptake of drugs into cells at the same time [108, 112]. In addition, we could also imagine using this effect for influencing cell growth and motility by providing unfavorable local environments in selected directions around the cells using microelectrode arrays. In the next chapter 5 we present two possibilities to control the cell adhesion, outgrowth and migration using local pH changes.

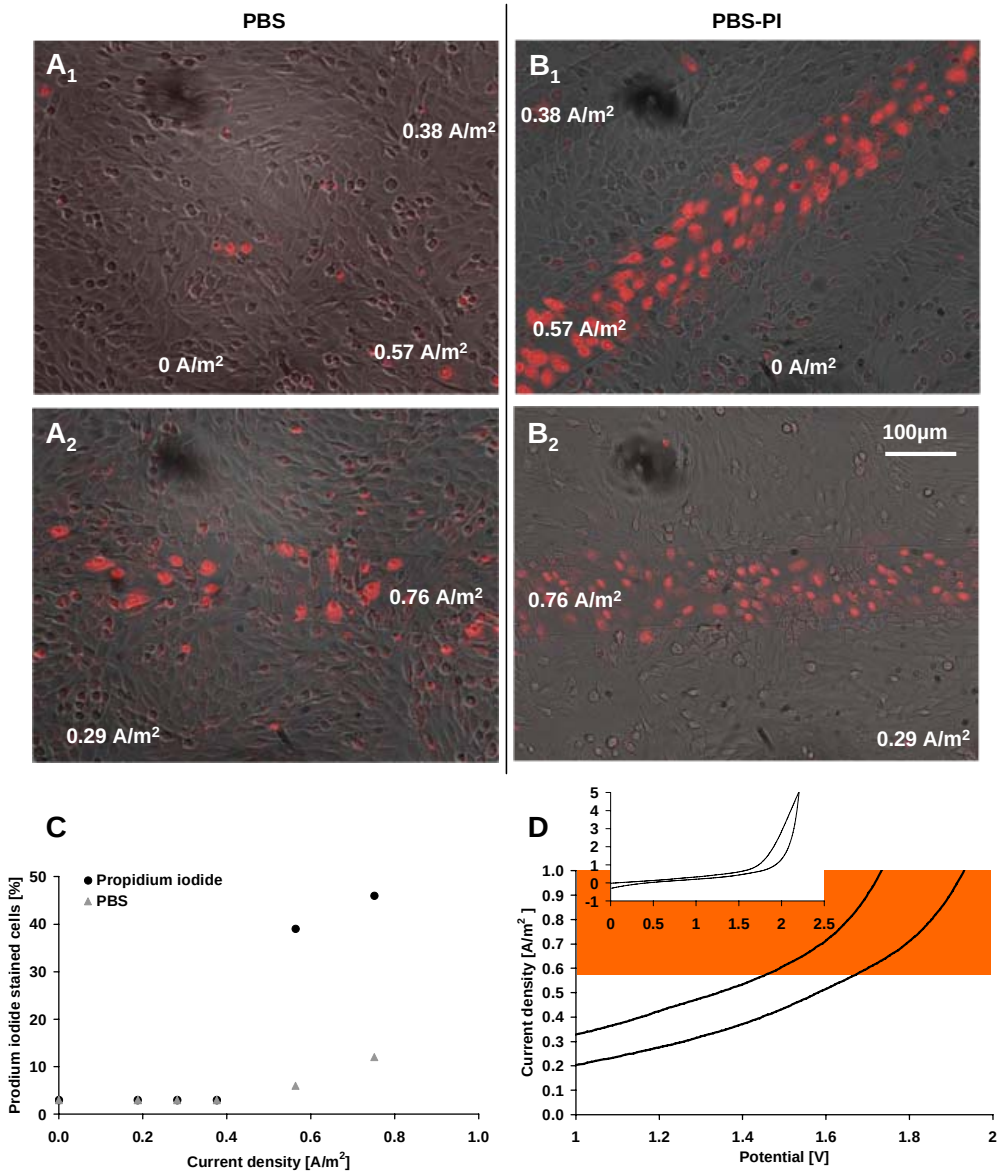

Figure 4.5.: The effect of an applied current on the viability of C2C12 myoblasts. DIC microscopy images superimposed on the corresponding propidium iodide fluorescence signals: 0.57 A/m^2 did not result in substantial cell death in PBS (A_1) while about 40% of the cells stained positive in PBS-PI (B_1). Higher currents resulted in an increase of the PI positive cells in both cases (A_2 and B_2). The quantitative assessment is summarized in plot C. (D) Magnified region of a typical cyclic voltammogram indicating the current range (red zone) where cell death occurs (the inset shows the full CV scan).

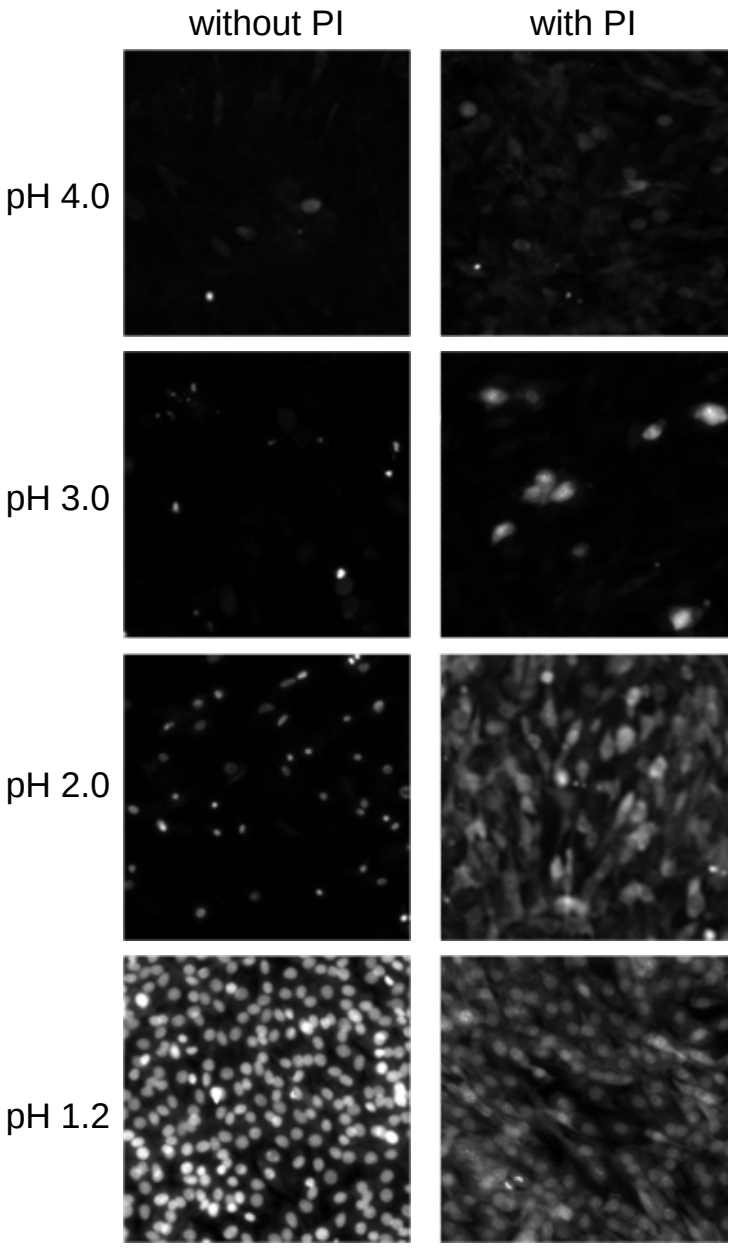

Figure 4.6.: C2C12 myoblast were exposed for 2 min to either the pure pH solutions or the pH solution containing propidium iodide. Afterwards the pH solutions with PI were exchanged to PBS-PI for 20 min before fixation. The cells in pure pH solution had the chance to recover in growth media for 30 min. The growth media was then changed to PBS-PI for 20 min before fixation. All images were taken with the same camera and microscope settings.

5. Electrically controlling cell adhesion, growth and migration

While the previous chapter was focusing on measuring the electrochemically induced pH change and showing the effects on cells directly grown on an electrode, we present in this chapter how to control the cell adhesion, outgrowth and migration using this effect. We present a combined approach by providing a 3D structure [33, 34] and electrical control over the neuron adhesion sites. We were able to control the neurite outgrowth by desorption of the protein resistant coating electrically [97]. To our knowledge it is the only attempt so far to electrically control the outgrowth of single neurons. Furthermore, we show a new technique using only small pulsed currents to actively inhibit the migration of myoblasts onto ITO electrodes. We believe the combination of the two presented patterning techniques described in this chapter is an attractive possibility to engineer topographically controlled neuron networks [101, 113] or to control the built-up of more complex tissues consisting of multiple cell types [27, 114, 115].

5.1. Neurochip for controlled neurite outgrowth

5.1.1. Experiments on controlling neuron adhesion and outgrowth

A neurochip was assembled as described in the materials and methods section 3.4.1 and was disinfected with 70% ethanol for 10 min, rinsed with H_20 and blow dried with N_2. The chip surface was turned hydrophilic in a plasma cleaner (Harrick Plasma, PDC-G32, USA) for 1 min at high power. Then the chip surface was coated with the PLL-*g*-PEG coating solution (Section 3.7.2) for 30 min before rinsing with physiological PBS buffer, pH 7.4 (Invitrogen) to remove unbound PLL-*g*-PEG molecules (Fig. 5.1, A, B). A platinum wire was immersed into the PBS solution as a counter electrode while applying +1.9 V for 5 min to the landing spot ITO electrodes to remove the PLL-*g*-PEG locally (Fig. 5.1, C). This removal process is due to the broken electrostatic interaction between the ITO and the PLL-*g*-PEG at the electrochemically altered local environment (lower pH, higher ionic strength, active radicals) of the selected ITO electrode (see more details elsewhere [90, 98]). After rinsing with PBS, the NG108 neuroblastoma cell suspension was poured onto

the chip and the cells were given 30 min to adhere to the landing spots in the incubator (37°C, 5% CO_2). Then the surface was gently rinsed with growth medium to remove excess cells using a 1 ml pipette (Fig. 5.1, D). The chip was filled with differentiation medium and put in the incubator and given 1 h to equilibrate. Neurite outgrowth was then enabled by applying +1.9 V for 5 min to the outgrowth pathway electrodes (Fig. 5.1, E-F). The narrow pathways (10 μm wide, 14 μm high) did not allow real time phase or interference contrast imaging of the neurite outgrowth, therefore the cells were visualized by actin staining (Section 3.5.2) and confocal microscopy.

5.1.2. Results on controlling neuron adhesion and outgrowth

The neurochip was designed to be completely transparent and built of non-toxic materials (SiO_2, ITO, SU8, PDMS) for cell culturing. The neurochip electrodes were arranged in a way that allows adhesion control over the landing spot and the outgrowth pathways, separately. Besides providing a 3D structure for neuron growth, the SU8 also serves as insulation material for the leads connecting the electrodes to the contacts at the edge of the chip outside the cell culture ring. At the same time, the structure mechanically stabilizes the weakly attached neurons against shear forces occurring while rinsing the chip with culture medium. The diameter of the landing spots (20 μm) and outgrowth pathway dimensions (10 μm wide, 240 μm long) were found empirically to be optimal for the NG108 cells. Larger landing spots led to multiple cell occupancy and smaller landing spots were not occupied by the neurons. The pathway length was adjusted to the neurite extension reached within 24 h in free culture. This cell line grows indefinitely in culture and exhibit stable electrical excitability for a few weeks which is necessary for future investigations of the neuron networks functionality. The experiment started by making the entire surface cell resistant by coating with PLL-*g*-PEG. Then the landing spots were switched cell adhesive by removing the protein resistant PLL-*g*-PEG coating electrically. The NG108 cell suspension was poured onto the chip and individual cells were able to find the adhesive spots by chance. Unfortunately, the occupancy rate of the landing spot was only about 10% using this method. To achieve a higher rate we suggest individual placement of the neurons into the landing spots by cell spotting [116, 117], microfluidic traps [118], optical tweezers [119] or dielectric forces [120]. Excessive cells were rinsed away gently from the cell resistant areas and neurite outgrowth of the adhered cells was initiated by adding differentiation medium. We have observed that the neurite outgrowth in figure 5.2, A stops at the ITO pathway electrode indicating that the PLL-*g*-PEG has not only been removed from the landing spot but also from the SiO_2 area between the landing spot and the pathway electrode. This is in agreement with previous observations, where the pH change close to microelectrodes was measured (Chapter 4). It was shown that protons diffuse away from the electrode depending

on the buffer capacity of the surrounding solution removing also PLL-*g*-PEG in the close vicinity of the electrode. In addition, Kenausis et al. observed differences in the adsorbed amount and pH stability of PLL-*g*-PEG coating depending on the metal oxide substrate [96]: (Nb_20_5 > $Si_{0.4}Ti_{0.6}O_2$ > TiO_2). Therefore, it might be possible that PLL-*g*-PEG interacts stronger with ITO than with SiO_2 and as such the induced local pH change is only sufficient to remove PLL-*g*-PEG from the connecting SiO_2 region while it is unaffected on the pathway electrode. Further tailoring the extent of PLL-*g*-PEG removal from the SiO_2 is possible by adjusting the applied voltage, buffer capacity of the culture medium and the dimensions of the neurochip.

5.2. Electrically inhibited cell migration

The cell adhesion and outgrowth control by electrical PLL-*g*-PEG removal can be used to switch an area once from cell repulsive to cell adhesive. Switching back to cell repulsive is not possible. Previously, in chapter 4 we and others have shown that locally applied currents can generate unfavorable conditions for cell growth resulting in electroporation or even apoptosis of cells [71, 74–80, 121]. In this section we demonstrate how locally applied small currents can be used to prevent cell migration onto selected regions on a chip.

5.2.1. Experiments on electrically controlling cell migration

A chemical pattern was created therefore first with electronic control for patterning C2C12 myoblasts on the SiO_2 background of a commercially available multielectrode array chip (Appendix A). After cleaning the chip accordingly, 1 ml of 0.1 mg/ml PLL coating solution (Section 3.7.2) was added to the surface and given 30 min to adsorb spontaneously onto the chip surface (Fig. 5.3, A). Then the chip was rinsed with PBS to remove any free PLL molecules. The electrical connection to the individual ITO electrodes was made through the MEA 1060 interface (Appendix A.5). A potential of +1.9 V was applied for 5 min to remove the PLL from selected ITO electrodes of the MEA chip (Fig. 5.3, B). The chip was then coated with PLL-*g*-PEG coating solution for 30 min before rinsing with pure DMEM to remove any free PLL-*g*-PEG molecules (Fig. 5.3, C). The myoblast cell suspension was added to the chip and given 15 min for adhesion of the cells. The chip was rinsed gently with culture media using a normal 1 ml pipette to remove excessive cells. In this way a pattern of cells attached to the SiO_2 background could be achieved while having cell free ITO electrodes at the same time (Fig. 5.3, D). The PLL-*g*-PEG was removed from the electrodes by applying again +1.9 V to permit the myoblast migration onto the selected electrodes (Fig. 5.3, E). The chip mounted into the interface was placed in the cell incubator and connected to the outside via SCSI cable

to a custom built pulse generator with 10 individual channels. Differently pulsed current cycles were then applied to selected ITO electrodes to test the minimal current dose necessary to inhibit the myoblast migration onto the ITO electrodes. The applied pulsed current dose was calculated using the average current over time and the exposed ITO surface (A $\sim$ 0.27 mm^2) of the individual electrodes.

The expected deposition of material due to the applied pulsed current was quantified with EC-OWLS (Section 3.2.1) using ITO coated waveguides. After cleaning and mounting the substrate to the probe holder, the chamber was rinsed with culture medium at a continuous flow rate of 10 ml/h. The baseline was set after 30 min equilibration time. Then a pulsed current of 0.48 Am^{-2} (I = 2 s, pause = 5 s) was applied to the waveguide and the deposition of material was quantified using the refractive index increment for proteins dn/dc = 0.18 [89].

5.2.2. Results on electrically controlling cell migration

An MEA chip was coated with cell adhesive PLL solution (Section 3.7.2) on SiO_2 background and cell repulsive PLL-*g*-PEG on the ITO electrodes. The myoblasts adhered well on the PLL while most cells could be rinsed away from the PLL-*g*-PEG coated regions (Fig. 5.4, A). Afterwards, the PLL-*g*-PEG was removed from the individual ITO electrodes by applying +1.9 V now enabling the migration of cells onto these electrodes. Differently pulsed current densities were then applied to electrodes in order to investigate the minimal current dose necessary to prevent the cell migration. In figure 5.4, B, two different current doses 23 and 44 mAs^{-1}m^{-2} were applied for 72 h. The current dose 44 mAs^{-1}m^{-2} inhibited the cell migration onto the ITO electrode, while the control electrodes and the lower current dose of 23 mAs^{-1}m^{-2} had no inhibiting effect.

Several similar experiments were conducted at different pulse lengths and doses. Figure 5.5 lists the applied doses in ascending order and the qualitative effect on cell migration. The cell migration was not affected by current dose = 34 mAs^{-1}m^{-2} (green), whereas dose = 44 mAs^{-1}m^{-2} with current densities = 0.48 mAm^{-2} (red) inhibited effectively the migration of cells onto the ITO surface within the observation time of 72 h. The only exception was at a current density of 0.19 mAm^{-2} (yellow), where the migration of cells was not inhibited completely even though the total dose was as high as 94 mAs^{-1}m^{-2}. The applied potentials were moderate and stable over 72 h to achieve the preset current pulses (+0.5 V for I = 0.38 mAs^{-1} m^{-2}). Cells around, or in close proximity to the electrodes were not affected by the current doses. Upon switching off the current pulses, the cells started to migrate onto the electrode. The effect of the electric current can be therefore characterized as locally and temporally restricted. This is also indicated by the pause length between the currents, which is preferably not longer than 10 s in order to achieve an inhibiting effect (Table 5.5).

At higher currents doses $\geq$ 100 mAs^{-1}m^{-2}, a slight darkening of the ITO elec-

trode was observed in transmission light microscopy suggesting deposition of some material from the culture medium. In order to quantify the amount of this unknown material, the culture medium was injected into an OWLS setup (Section 3.2.1) and current pulse dose of 137 $mAs^{-1}m^{-2}$ (I=0.48 Am^{-2}, +1.3 V, 2 s current, 5 s pause) was applied to an ITO waveguide (Fig. 5.6). The measurement showed a steady mass deposition from the culture medium with a slope of dm/dt= 30 ng $cm^{-2}min^{-1}$ over the measurement time of 2 h.

This result is similar to the observation of Ngankam and Van Tassel [107]. They reported continuous adsorption of polyelectrolytes of $0.6 - 5.41$ ng $cm^{-2}min^{-1}$ upon application of modest anodic potentials ($< +1.5$ V). The inhibiting effect on the cell migration at our current/potential levels could be therefore caused by a steady protein and/or mineral film formation out of the serum containing culture medium. However, it is also possible that electrochemical reactions associated with the Faradaic current directly influenced the cell adhesion. This could also explain, why currents < 38 $mAs^{-1}m^{-2}$ did not have an inhibiting effect on cell migration. The electrodeposited layer was stable in culture medium but could be dissolved in 1 M NaOH within one minute and the MEA chip could be reused for the next experiments.

5.3. Summary

We showed a new approach to control the adhesion of neurons and trigger the outgrowth of their neurites by electrically removing a protein resistant, cell repulsive PLL-*g*-PEG coating from a neurochip architecture. Furthermore the migration and growth of myoblasts on ITO electrodes could be inhibited by simply applying small pulsed currents without the use of any additional surface modifying molecules. We believe the combination of both techniques could be used for active cell guidance e.g. topologically controlled neuron networks, cell co-cultures and cell motility assays. Based on our results, a chip connecting neurons and myoblast could be realized enabling *in vitro* studies related to muscle neuron interactions. Thinkable are also implants using small pulsed currents to avoid any cell growth or even inhibit fibrous encapsulation e.g. towards an active cage for implanted glucose sensors for long term diabetes monitoring. The effects of small pulsed currents were studied *in vivo* in a rat model and are presented in the next chapter 6.

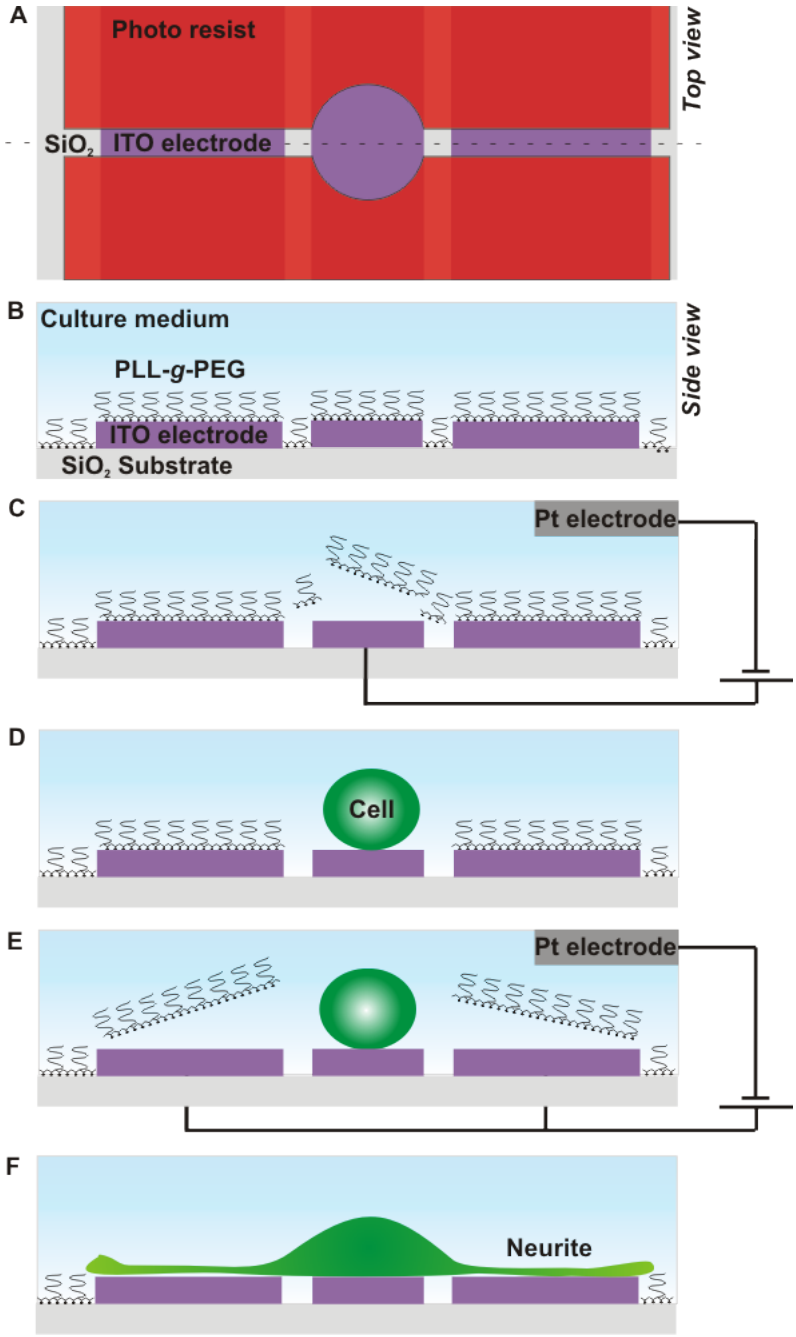

Figure 5.1.: (A) Schematic drawing of the neurochip with ITO electrodes and SU8 photo resist on a SiO_2 substrate. The SU8 structure surrounds the landing spot for the neuron body and lateral outgrowth pathways. (B) The whole chip surface (SU8, ITO, SiO_2) is made protein resistant by coating with PLL-*g*-PEG. (C) PLL-*g*-PEG is removed electrically from the landing spot by applying +1.9 V permitting neuron adhesion. (D) After the neuron adhered to the landing spot, (E) the PLL-*g*-PEG is also removed from the outgrowth pathways and (F) neurites grow along the pathways.

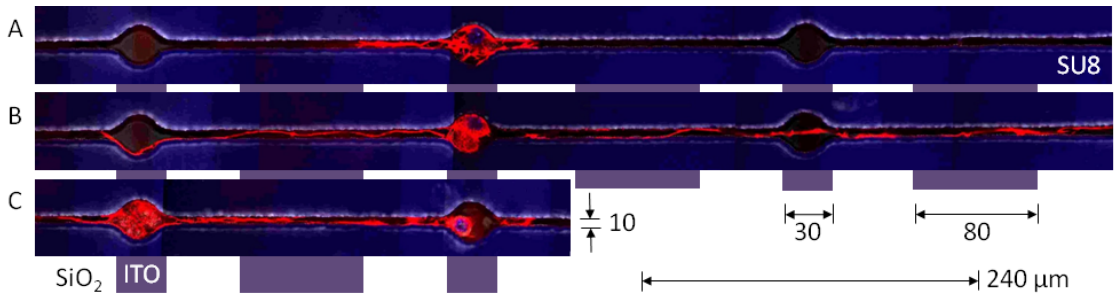

Figure 5.2.: CLSM images showing neurons inside the neurochip architecture after 24 h differentiation with differently controlled neurite outgrowth. The images of actin stained neurons (red) are merged with the signal of the autofluorescent SU8 structure (blue), while the transparent ITO electrodes are illustrated schematically. (A) Neurites grow within the landing spots but the outgrowth is inhibited by the protein resistant PLL-*g*-PEG coating in the connecting pathways. (B) Neurite outgrowth along the pathways is enabled by electrically removing the protein resistant coating also from the connecting regions. (C) Two morphologically interconnected neurons. (Note that the images were made with high resolution and stitched together afterwards.)

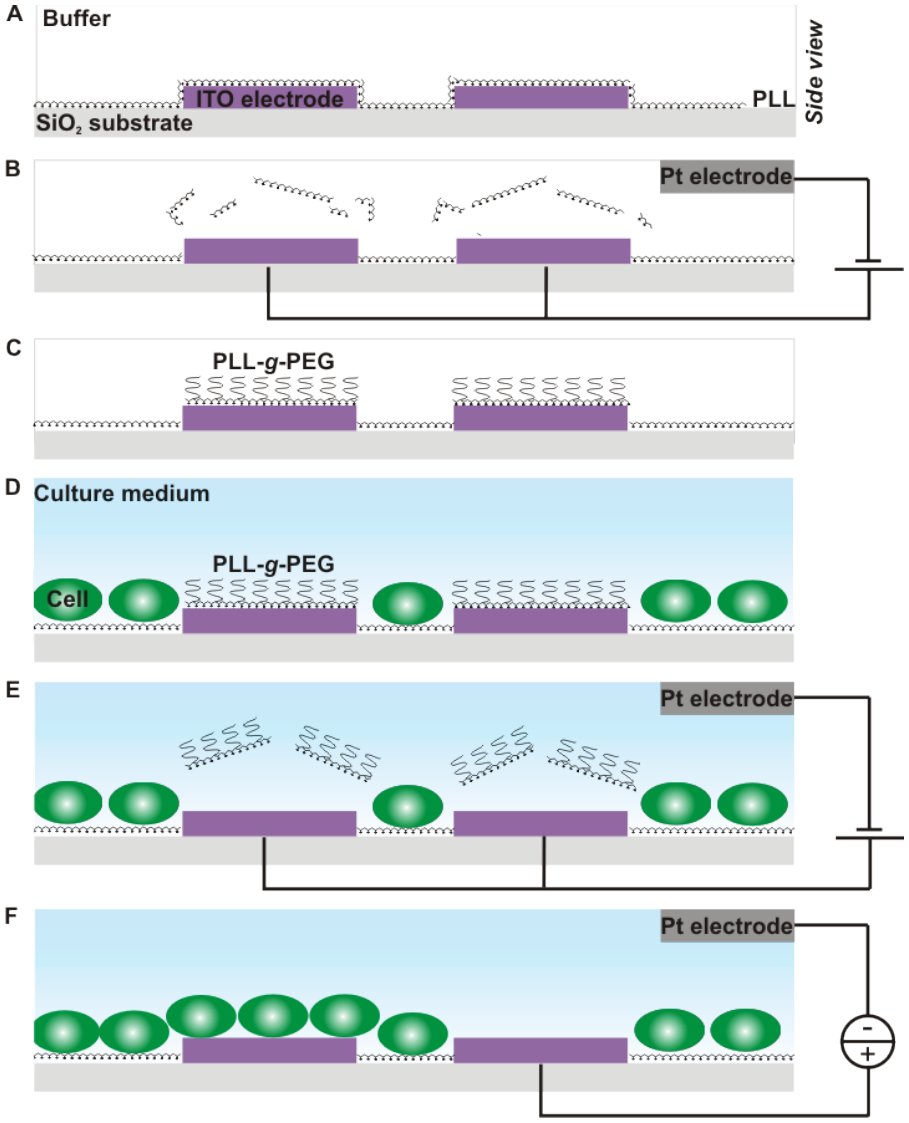

Figure 5.3.: Schematic drawing shows the experimental setup for finding the minimal current dose necessary to inhibit cell migration. (A) The whole chip surface is coated with cell adhesive PLL. (B) The PLL is removed from the selected ITO electrodes by applying +1.9 V and (C) protein repellant PLL-*g*-PEG adsorbs spontaneously onto the bare electrodes. (D) Myoblasts adhere on the PLL coated SiO_2 background, while the PLL-g-PEG coated electrodes remain cell free. (E) After rinsing away excessive cells, PLL-g-PEG is removed by applying +1.9 V. (F, left) Cells start to migrate immediately onto the control electrodes, (F, right) while the cells avoid electrodes with applied pulsed currents.

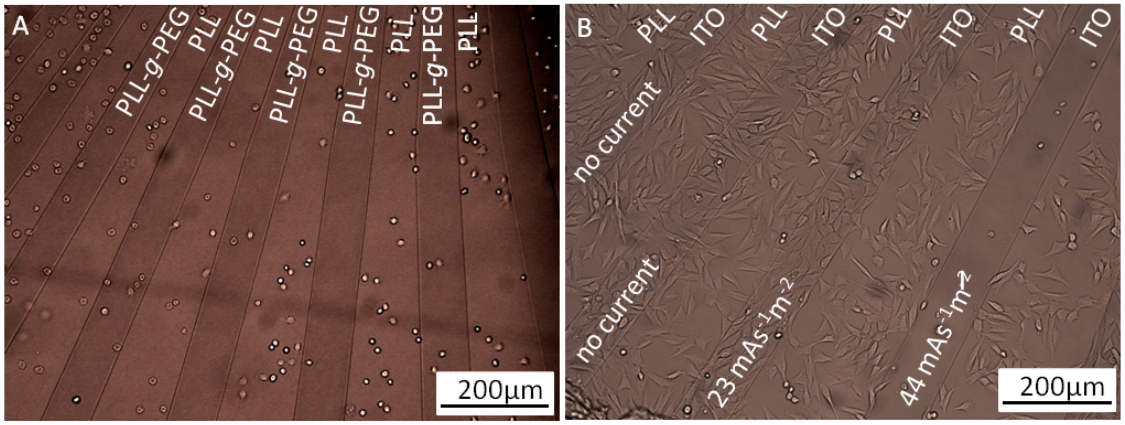

Figure 5.4.: (A) Transmission light microscopy images of C2C12 myoblasts patterned on the MEA chip with PLL coated SiO_2 background and PLL-*g*-PEG coated ITO electrodes. The cells adhered only to the PLL coated background. (B) After electrically removing PLL-*g*-PEG cells started to migrate onto the bare ITO electrodes with no current or low pulsed current dose. Applied pulsed current doses = 44 $mAs^{-1}m^{-2}$ inhibited cell migration onto the electrode within the observation time of 72 h.

Dose [mA s^{-1} m^{-2}]	Current I [A m^{-2}]	I Pulse [s]	Pause [s]	Migration [ ]
9	0.19	1	20	yes
16	0.48	1	30	yes
17	0.19	1	10	yes
18	0.38	1	20	yes
23	0.48	1	20	yes
31	0.19	1	5	yes
31	0.19	1	5	yes
34	0.38	1	10	yes
44	0.48	1	10	no
63	0.38	1	5	no
80	0.48	2	10	no
94	0.19	1	1	some
96	0.48	5	20	no
111	0.48	3	10	no
160	0.48	5	10	no
160	0.48	5	10	no
241	0.48	5	5	no
241	0.48	10	10	no

Figure 5.5.: Ascending list of the current doses that were used to inhibit cell migration onto ITO electrodes. Cells were not affected by pulsed current doses = 34 $mAs^{-1}m^{-2}$ (green), whereas doses = 44 $mAs^{-1}m^{-2}$ with current densities = 0.48 Am^{-2} (red) inhibited the migration of cells onto the ITO surface. The current density 0.19 Am^{-2} (yellow) did not inhibit the migration completely even at a dose as high as 94 $mAs^{-1}m^{-2}$.

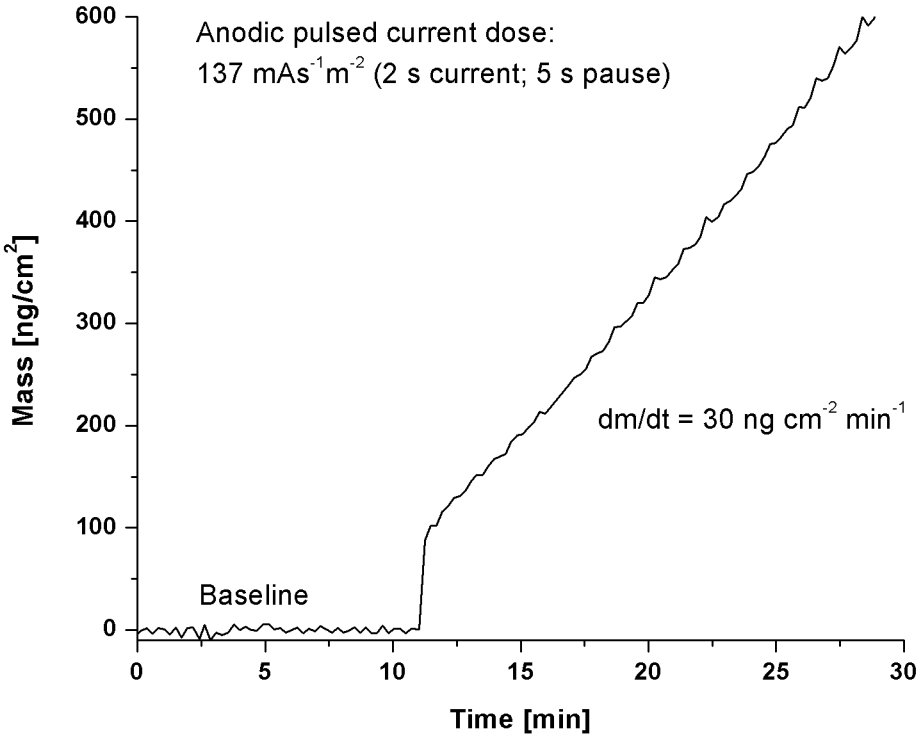

Figure 5.6.: The EC-OWLS measurement shows the steady deposition of material from culture medium onto the ITO surface during an applied current dose of 137 $mAs^{-1}m^{-2}$.

6. Effects of small pulsed currents on the viability of cells, in vitro and in vivo

Previous chapters dealt with *in vitro* cell cultures, and this chapter we built an implantable current pulse generator with platinum electrodes to study the effect of long pulsed, small currents *in vitro* and *in vivo* [70]. Encouraged by the experimental *in vitro* results done by Mr. Michael E. Bullen[1], we believed to have found a new approach for preventing encapsulation around the electrode by producing a constant cell turnover at the electrode interface. Apoptotic cells would be constantly removed by phagocytes without provoking an inflammatory response [122]. At the same time the resistivity of the tissue would not increase. This would open new prospective on future of long-term implants with active electrodes such as glucose sensors or stimulation, recording electrodes. Therefore the pulse generator was implanted into rats to study the effects *in vivo* for up to 21 days.

6.1. In vitro

6.1.1. In vitro experiments with the electric pulse generator

An implantable electric pulse generator and electrodes were built as described in the methods and material sections 3.3.2, 3.4.2 and rat aortic derived cells (RAOC) were prepared as described in section 3.5.3. The electrodes were again sterilized with 70% ethanol and irradiated for 30 minutes with UV light. The cells were detached using 0.25% trypsin/EDTA solution (PAN Biotech GmbH, Aidenbach, Germany) and seeded directly onto the implant lying in a Petri dish (Fig. 6.1). The systems were then incubated for 1, 6, 12 and 24 h at 37°C and 5% CO_2. A cell viability staining was performed according to section 3.5.3 to visualize dead cells with propidium iodide and the total cell number by a Hoechst 33342 dye to measure the effects of the pulsed electric current. To ensure that the different coatings (SiO_2, Pt) had no influence on cell behavior and viability, a control experiment was performed over 24 h with the same method as above, however without the application of current

[1]Regenerative Medicine Program and Cardiovascular Surgery Research, University Hospital Zürich, Raemistrasse 100, 8091 Zürich, Switzerland

(results not shown). The type of cell death and the cell adhesion contact size was investigated with immunochemical staining of cleaved caspase-3 or vinculin, respectively (Section 3.5.3).

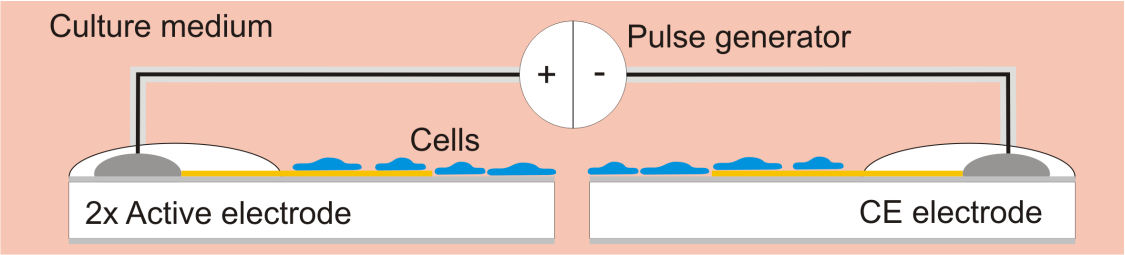

Figure 6.1.: Schematics of the *in vitro* experimental setup using the two working electrodes (anode), the counter electrode and pulse generator in a cell culture dish.

The electrochemically generated pH between cell and electrode was calculated by a 2D finite element method (Section 3.7.4) in the gap between a hypothetical surface attached round shaped cell (radius 2.5 - 3.1 μm, determined by above methods) on an infinite flat electrode where two differently pulsed currents from the pulse generator (I = 2.5 s; pause = 2.5 s) and (I = 5 s; pause 5 s) were applied (Section 3.7.4). The gap between the cell and the electrode was assumed to be 100 nm. Two different parameter sets were used to calculate the range of pH generated in the geometric center between cell and surface: The first parameter was set with the diffusion coefficient for protons from literature $D_{real} = D_{proton} = 9.3{\cdot}10^{-9}$ m^2s^{-1} and the real current applied $I_{real} = 0.37$ A/m^2, the second fitted parameter set $D_{fit} = 3.3{\cdot}10^{-10}$ m^2s^{-1} and $I_{fit} = 0.017$ A/m^2 was adjusted according to previous work (Chapter 4).

6.1.2. In vitro results with the electric pulse generator

The implant and the electrodes were placed in a Petri dish before adding the RAOC cell suspension. Exposed to the pulsed current densities of 0.37 A/m^2, the RAOCs displayed an increase in cell death with time (Fig. 6.2, A). The cell mortality was higher on electrode 2 (5 s current, 5 s pause) for the first hour. After 24 h, the mortality was 96 $\pm$ 3% on electrode 1 (2.5 s current, 2.5 s pause) and 96 $\pm$ 5.0% on electrode 2. In contrast, cells grown on the SiO_2 control on the same electrode had mortality of 3 - 8% throughout the experimental time. The cell death was highly localized to the active Pt* surface (Fig. 6.2, B), with a well defined boundary limited to the active Pt* electrode surface.

To investigate the type of cell death after 24 h, the presence of apoptotic cell death was determined by staining with anti-cleaved caspase 3 antibody which detects endogenous levels of the large fragment (17/19 kDa) of activated caspase-3. The

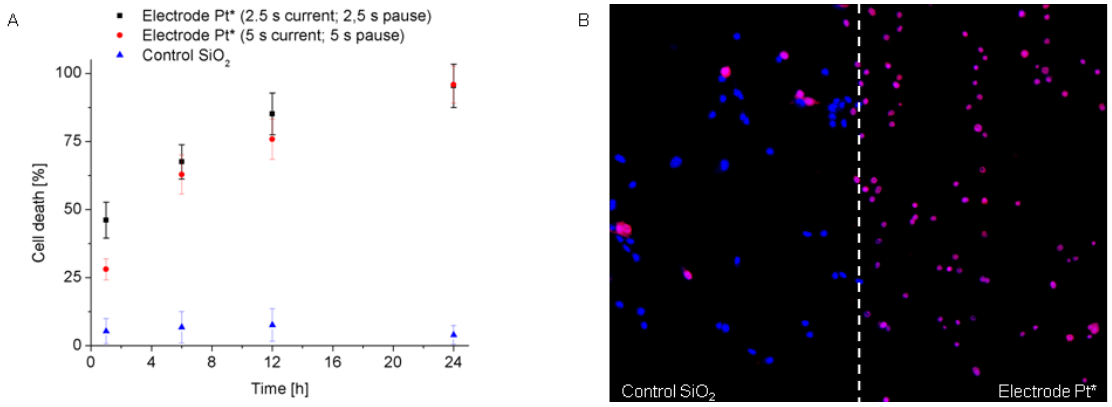

Figure 6.2.: (A) Percentage of dead cells versus time on the active Pt* electrode compared to the passive SiO_2 control surface. Control experiments with no current applied showed no difference in cell death between Pt* and SiO_2 surface. Fluorescence image of the SiO_2/Pt* boarder (dashed line) on the electrode after applying a pulsed current for 24 h and staining for dead cells with propidium iodide (red). (B) The boundary between living cells (blue, Hoechst 33342) and dead cells is well defined to the active Pt* electrode surface.

cells on the SiO_2 control surface showed minimal caspase-3 activity (Fig. 6.3, A), while 95 ± 4 % of RAOCs cell on the active Pt* surface, were stained positive for this apoptotic marker (Fig. 6.3, B). Cells that did not express caspase-3 could not conclusively be identified as either apoptotic or necrotic. Indicative signs of apoptotic bodies such as fragmentation of nuclear chromatin could be detected in many of these cells.

After being seeded on the electrodes for 24 h, a distinct difference in cell morphology could be observed between the RAOCs adhered on the SiO_2 control (Fig. 6.4, A) and the active Pt* electrode surface (Fig. 6.4, B). The cells on the control side attached and spread over the SiO_2 control surface as observed in normal cell culture, while the cells adhered to the active Pt* electrode surface kept their round shape and were not able to spread on the surface. The adhesion size (area of focal contacts) of the cells was visualized by staining with monoclonal mouse anti-human vinculin-1. The adhesion size was of 154 ± 24 μm^2 on the SiO_2 control and 26 ± 6 μm^2 on the active Pt* electrode surface.

The pH change between the cell and the active Pt* electrode due to Faradaic reactions was calculated using the adhesion area size of the apoptotic cells, assuming a circular shaped cells with the measured mean area for apoptotic RAOC cells A = 26 μm^2 and the standard deviation SD = 6 μm^2. The minimal and maximal radius of the model cell are r_{min} = 2.5 or r_{max} = 3 .1 μm ($r^2_{min,max}$ = (A±SD)/π), respectively. The asymptotic mean pH values reached after 1000 s are given in

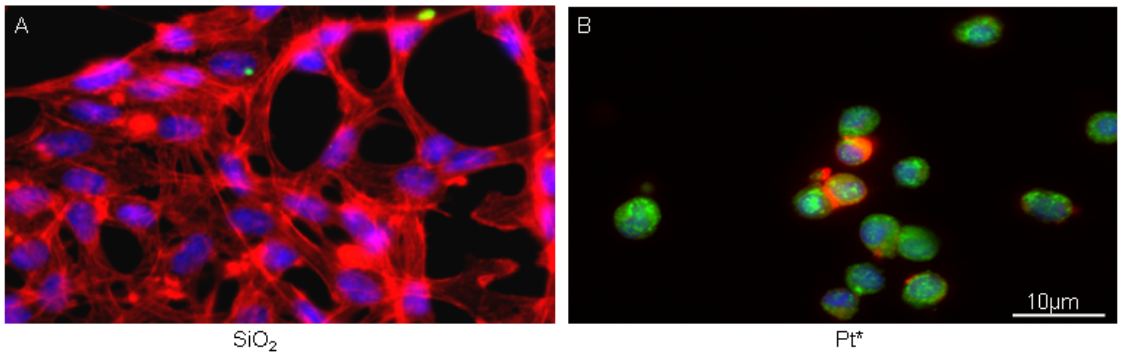

Figure 6.3.: Immunofluorescent images of RAOCs showing cleaved caspase-3 (green), actin stress fibres (red) and nuclei (blue) after 24 h. (A) The RAOCS on the SiO_2 control site of the electrode show normal cell morphology and minimal caspase-3 activity indicative of normal cell turnover. (B) Almost all RAOCs on the active Pt* electrode surface show cleaved caspase-3 activity indicating an apoptotic cell death induced by the applied pulsed current.

figure 6.5. There is a pH difference of 0.1 between the two differently pulsed currents (Electrode 1, 2) for given cell size and parameter set (D_{real}, I_{real}) ; (D_{fit}, I_{fit}). The pH differs for different cell radii (2.5; 3.1 μm) only on electrode 1 for the parameter set (D_{fit}, I_{fit}). A larger difference pH of 0.5 is observed for different parameter sets (D_{real}, I_{real}) ; (D_{fit}, I_{fit}) at given radius and electrode.

The pH change within the cycles is shown in figure 6.6, A for the initial 150 s, assuming the cell attaches to the active Pt* electrode surface having immediately an average adhesion area with r = 2.8 μm. During an electric pulse cycle, the current decreases the pH almost instantly in the gap between cell and electrode. During the pause, the pH increases due to proton diffusion out of the gap. The low peak pH values reached at the end of the current pulse are similar for the short (2.5 s) and long (5 s) pulsed currents, but the average pH is lower for the short pulsed currents at a given electrode. The asymptotic mean pH range dependant on the cell adhesion area is shown in figure 6.6, B, calculated using the parameters reaching the lowest (2.5 s pulse, D_{real}, I_{real}) and the highest pH (5 s pulse, D_{fit}, I_{fit}) for an average cell adhesion area with r = 2.8 μm. The pH variation between the cycles is indicated with the error bars. The larger the cell radius the more variation of the pH within the cycles is observed, while the mean pH value decreases in a steady slope with increasing radius.

Currents applied during cell attachment clearly induced apoptosis of cells that landed on the active electrodes as indicated by their globular shape [122, 123]. In addition, staining the cells after 24 h of current application revealed that most cells died by activation of apoptotic pathways. The activation of caspase-3 is a central

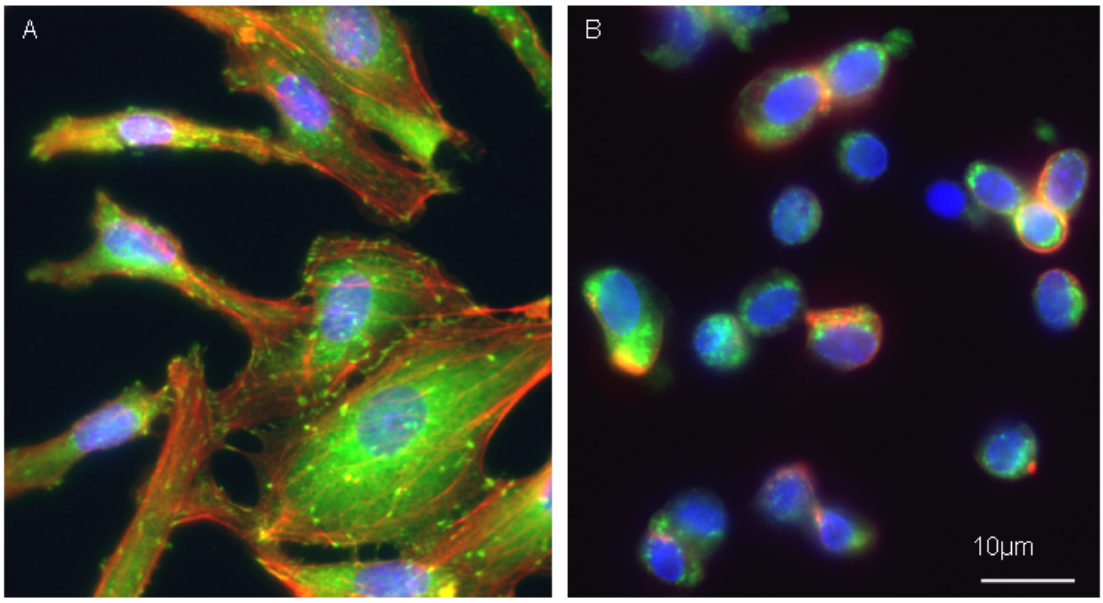

Figure 6.4.: Immunofluorescent images of RAOCs showing vinculin adhesion sites (green), actin stress fibres (red) and nuclei (blue) after 24 h. (A) Cells grown on the SiO_2 control side of the electrode show normal adhesion and spreading behavior, (B) while cells on the active Pt* electrode surface show complete disorganization of the cytoskeleton and lack of actin stress fibers accompanied by cellular rounding with diffuse, globular appearance of vinculin.

Electrode	1	1	2	2
Current [s]	2.5	2.5	5	5
Pause [s]	2.5	2.5	5	5
Radius [µm]	2.5	3.1	2.5	3.1
pH ($D_{real;}$ I_{real})	**3.6**	**3.6**	**3.7**	**3.7**
pH ($D_{fit;}$ I_{fit})	**4**	**4.1**	**4.2**	**4.2**

Figure 6.5.: The calculated, asymptotic mean pH values (bold) reached after 1000 seconds for two differently pulsed currents (Electrode 1,2), the two parameter sets (D_{real}, I_{real}) ; (D_{fit}, I_{fit}), and different radii of the measured cell adhesion area.

event in apoptosis, and is an early marker of apoptosis. It has previously been reported to display either weak or no cytoplasmic staining in later stages of apoptosis, or staining to be localized to the nucleus [124]. Therefore the few cells which stained negative over the active electrodes may have been in the later stages of apoptosis no longer expressing caspase. In addition, as anti caspase-3 does not recognize full length caspase-3 or other cleaved caspases, its detection indicates apoptosis only

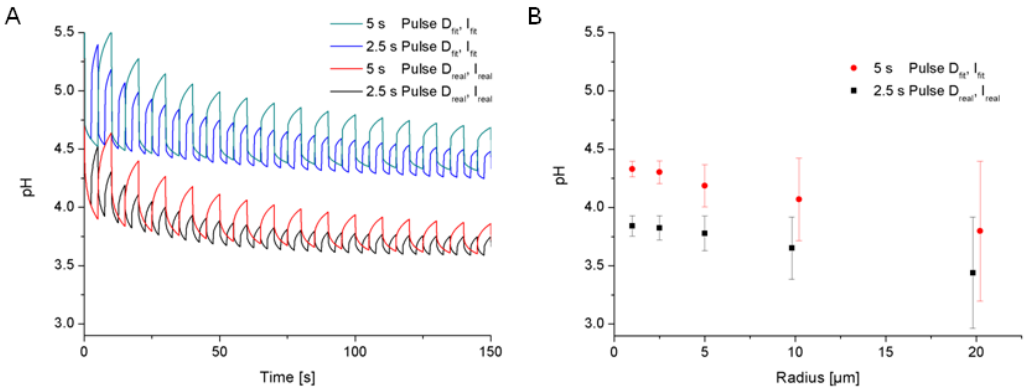

Figure 6.6.: (A) Calculated pH in the gap between a cell with an average adhesion area (r = 2.8 μm) and the active Pt* surface with two different parameter sets and two differently pulsed currents for the initial 150 s. (B) The asymptotic mean pH value dependant on the radius of the cell adhesion area. The pH variation between the pulse cycles is indicated by the error bars.

via the caspase-3 pathway. As a result, although caspase-3 is considered one of the key executioners of apoptosis, the presence of other apoptotic pathways cannot be excluded. While it is possible these cells may have undergone apoptosis via an alternative pathway not utilizing caspase-3, this was not conclusive and as such these cells were not counted as apoptotic. In this study cells were exposed to pulsed currents throughout the experiment, i.e. including some time preceding cell attachment, in order to simulate the conditions during *in vivo* implantation of the electrodes. Although the generated electrochemical species diffuses into the culture medium, this space between cell and electrode becomes a small gap of around 100 nm [125], when a cell attaches to the electrode surface. The products are accumulated within this gap and might reach toxic concentration levels depending on the current applied, adhesion size and the diffusion coefficient of the toxic species. Cells must therefore attach to the electrode before a significantly large area of their membrane gets exposed to the dangerous zone causing cell death. This is a possible explanation of why we observed cell death after increased time in comparison to other studies that exposed cells to electric currents only after they had formed a confluent layer on the electrode (Chapter 4). The adhesion size was optically determined after vinculin (focal contacts) staining [126]. Vinculin represents a key element in the transmembrane linkage of the extracellular matrix to the cytoplasmic microfilament system and is associated with a large number of cytoskeletal and focal adhesion proteins. These multi-protein complexes are further associated with cell adhesion signaling molecules important to rendering cells susceptible or resistant to apoptosis [127]. The apoptotic RAOC cell adhesion size was 26 μm^2, radius

r = 2.8 μm if we assume a circular cell adhesion spot (see section 3.7.4) after 24 h of applying currents. The observed adhesion area was independent of the applied current pulses (1, 2) further supporting our hypothesis that a critical adhesion area over the electrode is required for inducing apoptosis. Modeling the expected pH in the gap, we found that the short pulsed electrode 1 reaches lower mean pH values during the initial phase of cellular attachment (see figure 6.6) but almost the same asymptotic pH. This might explain the observed higher ratio of dead cells on electrode 1 after 1 h. On the other hand, the simulated asymptotic pH vs. cell radius curve shows no special reason for the observed critical adhesion radius of r = 2.8 μm. Another electrochemically generated product is chlorine, which reacts with water to HOCl [26]. HOCl (hypochloric acid) has been reported to cause apoptic cell death due to the formation of chloramines in the culture medium [128]. In addition, a minute amount of chlorine induced de-spreading of adherent cells [87]. As such, if the electrochemical products suppress cell adhesion this itself might induce apoptosis according to Chen et al. [5]. The disruption of focal adhesion complexes weakens the interaction between the cells and the extracellular matrix, rendering them more susceptible to apoptosis [123], even in the presence of sufficient growth factors. Another possible mechanism is related to the corrosion of electrode itself: e.g. platinum chloride compounds from electrode corrosion dissolve at higher potentials and can inhibit cell growth [129], however at lower potentials and in the presence of serum albumin no platinum dissolution was observed [130]. On the other hand, the platinum corrosion can probably be ruled out in this case, since a similar growth inhibiting effect at low currents was also observed on indium tin oxide electrodes (Section 5.2).

6.2. In vivo

6.2.1. In vivo experiments with the electric pulse generator

A single implant, consisting of the pulse generator and three electrodes (Fig. 3.4, A), was implanted into each of the 20 Sprague-Dawley rats according to the procedure described in the methods and materials section 3.6.1. After the experimental time, the impedance spectra of the implanted electrodes were measured right before explantation with an Autolab PGSTAT302N potentiostat with the Frequency Response Analyzer Software v.4.9.007 from Eco Chemie (Utrecht, Netherlands). The spectra were measured with an amplitude of 50 mV between 0.2 Hz and 1 MHz. The pulse generator was therefore taken out of the anaesthetized rat, the wires were cut and dismantled, while the electrodes remained in their position under the skin. The free ends of the cables were then connected to the potentiostat with Kleps clamps. The impedance was measured between the active Pt* electrode and counter electrode. After a lethal dose of carbon dioxide inhalation the rats

were decapitated to keep the electrodes in their position in the tissue. The rat heads with the electrodes still in position were fixated and stained as described in 3.6.2. The implant operational capability was then tested *ex situ* with a voltmeter and implants with no signal where categorized as non working. Impedance measurement control experiments were performed in culture medium and in a freshly sacrificed mouse. After removing the coat, two incisions were made in the hind limb muscles muscle and the electrodes were placed in the pockets to measure the resistance of muscle tissue. Filling the incisions with culture medium simulated the liquid gap between electrode and tissue. The impedance was also measured across fascia|muscle|fascia or fascia|fatty tissue|fascia by adding a small amount of culture medium between electrode the fascia and mechanically attaching the electrode on the surface.

6.2.2. In vivo results with the electric pulse generator

The electrode impedance was measured *in vivo* from 7 electrodes that remained functional for the entire experimental time and from 17 electrodes of implants that stopped working sometime during the experiment. The impedance spectra of all electrodes were measured with an amplitude of 50 mV between 0.2 Hz and 1 MHz. The impedance Z was plotted at selected frequencies 0.2 Hz, 1 kHz, 0.5 MHz in figure 6.7, 6.8, 6.9. For working implants the impedance value remains on a more or less constant the level during the entire experiment, whereas the non working implants showed an increase in impedance at the selected frequencies. Since some of the electrodes showed non-physical impedance values at 0.2 Hz (i.e. much higher than any of the control experiment values), these were considered to be compromised even if their X-ray image showed no obvious signs of cable rupture. As such, 5 electrodes (1 working, 4 non working) were therefore highlighted (*) in figure 6.7 and were not taken into account for the discussions.

The electrodes used for histology worked for up to 21 days in the animal and were fully functional at the time of explanting. The toluidine blue stained cross section of a representative selected electrode (21 days) allows direct comparison between working and control areas on the same electrode (Fig. 6.10, A-D). We did not find any significant difference in the morphology of the surrounding connective tissue between the working platinum electrode Pt* (Fig.6.10, A), control platinum electrode Pt without the current (Fig. 6.10, B) and SiO_2 bulk material (Fig. 6.10, C). No signs of cell necrosis or apoptosis were noted in the cells sheets bordering the electrode surface. Additionally, the images show the absence of the monocyte/macrophage recruitment to the site of implant site, indicating the absence of a stronger immune response either to the control or the active sides of the electrodes.

In vitro, the implantable custom built pulse generators were working in liquid at cell culture condition full workability during repeated, short term experiments.

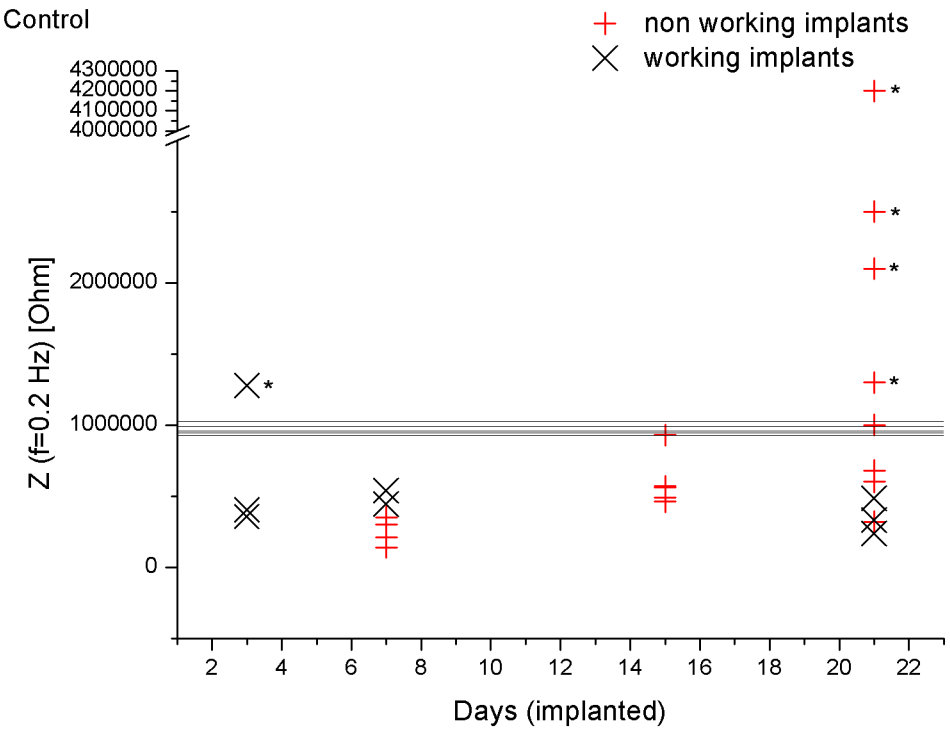

Figure 6.7.: Impedance values at 0.2 Hz of the implants that remained functional for the entire experimental time (x) and the non working implants (+) are plotted versus the implantation time. The black dashed lines are impedance values from control experiments through culture medium, muscle tissue with liquid contact to the electrode, fascia|muscle|fascia, muscle tissue without liquid contact to the electrode, fascia|fat tissue|fascia. Outliers are marked with (*) and were identified by showing non-physical impedance values (i.e. much higher than any of the control experiment values).

There was no leakage or malfunction observed. *In vivo* in contrast, the electronic circuit and battery, embedded in EPOTEK-320M, was compromised by the inflammatory foreign body reactions and some implants stopped producing electric pulses *in vivo*. In these failed implants, a weak point was found in the epoxy casing due to non-uniform embedding, where body fluids could enter and caused failure of the electric circuit while implanted. At the end, 7 electrodes remained functional for the entire time while 17 electrodes stopped working during the experiment. The impedance of all functional electrodes but one remained low at all three measured frequencies compared to the impedance of electrodes that were connected to a pulse generator that stopped working at a certain time point. At low frequencies (0.2 Hz),

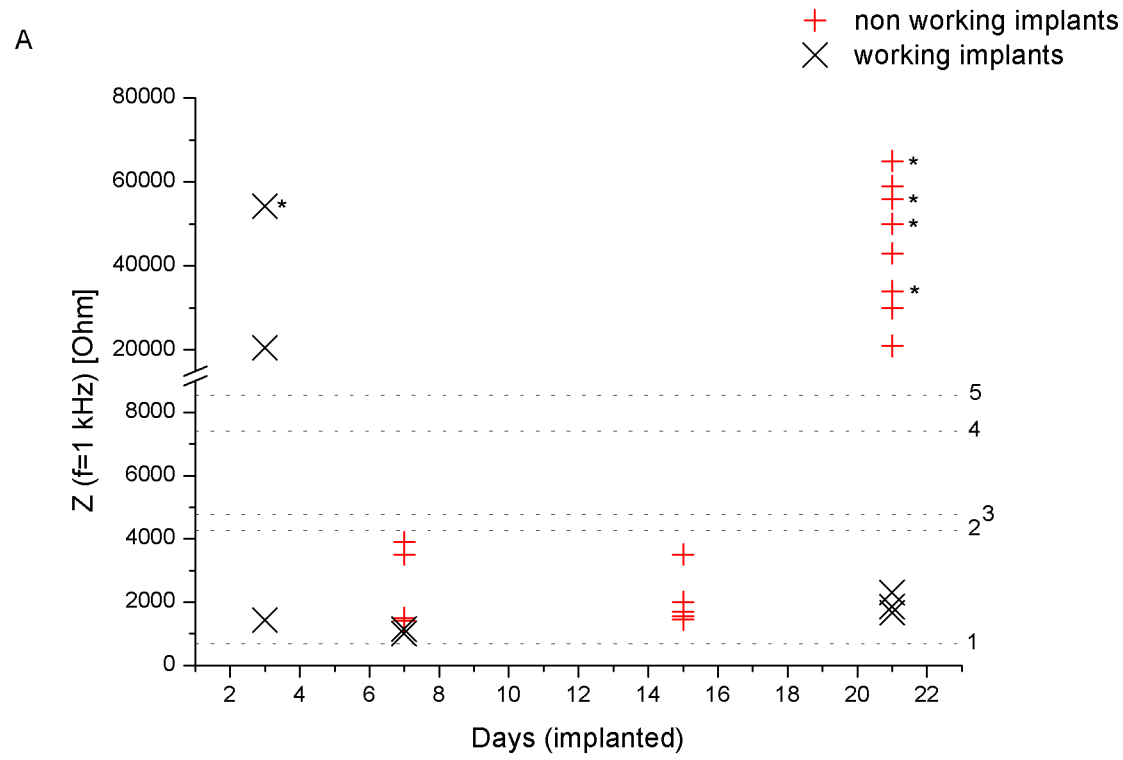

Figure 6.8.: Impedance values at 1 kHz of the implants that remained functional for the entire experimental time (x) and the non working implants (+) are plotted versus the implantation time. The black dashed lines are impedance values from control experiments through culture medium, muscle tissue with liquid contact to the electrode, fascia|muscle|fascia, muscle tissue without liquid contact to the electrode, fascia|fat tissue|fascia. Outliers are marked with (*) and were identified by showing non-physical impedance values (i.e. much higher than any of the control experiment values).

changes in the electric double layer at the interface boundary are measured. The formation of a biological film here could lead to increased impedance as observed on the electrodes that stopped working or their electrical contact was broken (see figure 6.7). The tissue conductivity was measured at higher frequencies. Current is transported by the motion of free ions according to the applied electric field. The initial inflammatory tissue response increased the amount of exudate around the implants and kept impedance low for all electrodes for the first 15 days. After 21 days, the histology samples no longer show a liquid gap between electrode surface and the tissue. The impedance of the non working electrodes showed the expected increase due to the diminished fluid gap and the presence of densely packed cells

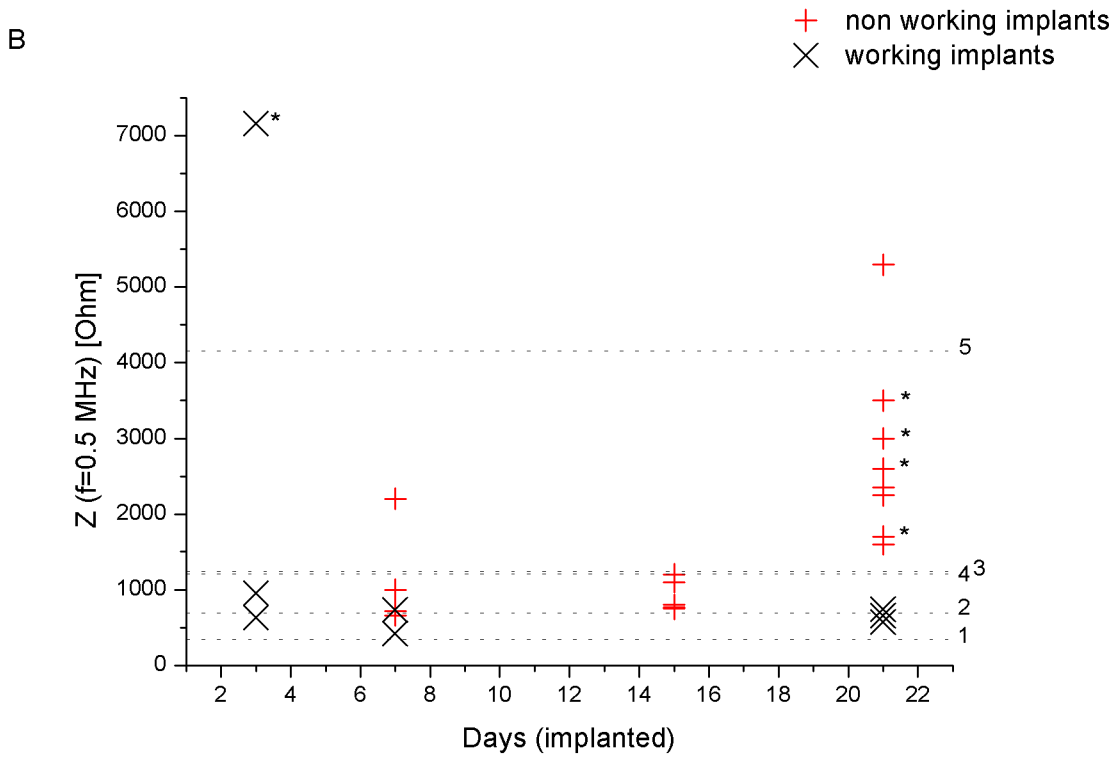

Figure 6.9.: Impedance values of the implants that remained functional for the entire experimental time (x) and the non working implants (+) are plotted at 0.5 MHz versus the implantation time. The black dashed lines are impedance values from control experiments through (1) culture medium, (2) muscle tissue with liquid contact to the electrode, (3) fascia|muscle|fascia, (4) muscle tissue without liquid contact to the electrode, (5) fascia|fat tissue|fascia. Possible outliers are marked with (*). Two pairs of overlaying data points were shifted by 5% for visibility.

on the platinum electrode surface. In the control experiments, the impedance was decreased by $\sim$ 40 % adding culture media to the electrode interface. In contrast, the electrodes with applied pulsed current showed no increase in impedance at 1 kHz and 0.5 MHz even though our histological data has not revealed any changes comparing the tissue surrounding the active electrode surface Pt* with the platinum control surface Pt and the SiO_2 control surface. A similar phenomenon has already been observed by applying 1.5 V for 4 s to iridium electrodes *in vivo* [70]. The authors propose that conductivity pathways are formed through the surrounding tissue (within 100 μm from the electrode surface) during this rejuvenation increasing recording quality and lowering electrode impedance. We applied smaller

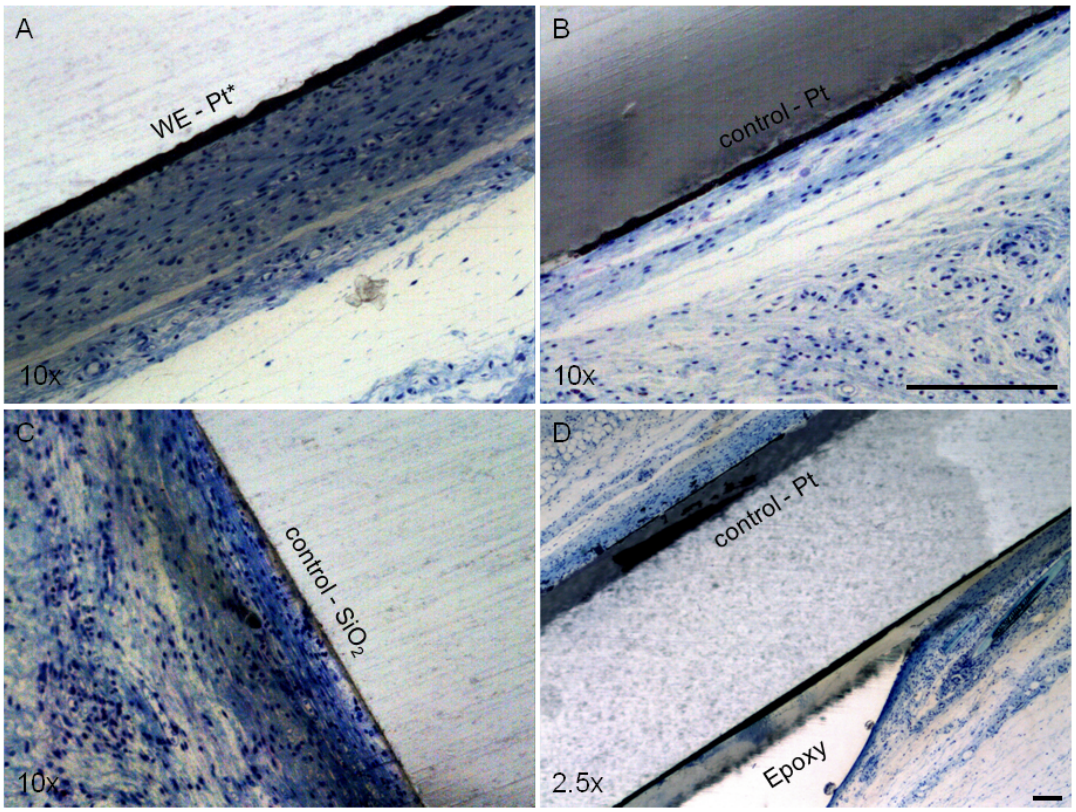

Figure 6.10.: Bright field microphotographs of toluidine blue stained tissue sections across the implanted electrode|connective tissue interface. This representative electrode was explanted after 21 days *in vivo* and remained functional for the entire experimental time. The comparison of the tissue morphology and cell appearance in the vicinity of the interface revealed no significant difference between the platinum working electrode Pt (A), control platinum electrode without the current Pt (B) and SiO_2 bulk material (C). No signs of cell necrosis or apoptosis as well as no signs of inflammation are observed in the cell layers adjacent to electrode surface, suggesting that neither the implanted electrodes nor the applied pulses of current produced any adverse effect in the surrounding tissue. Note that the extensive tissue raptures arranged in parallel to the electrode surface have been provoked by the unfavorable procedure. Scale bar: 0.2 mm

currents/voltages repeatedly and observed a similar effect, but our current density or applied voltage might be too small to produce instant effects on the impedance, but enough to keep the adjacent cells in a constant reorganization either through apoptosis or via disintegration of the adherence junctions. We believe that such

low currents affect only the nearest cell layer. Unfortunately, a live dead staining or the staining for apoptotic cells was not possible, because the tissue sample had to be embedded in epoxy resin for cutting and polishing.

6.3. Summary

In vitro, we have shown that small pulsed currents induce apoptosis within 24 h in almost all the RAOC cells attached to the electrode surface. Apoptosis is induced either directly by toxic concentrations of electrochemically generated species in the gap between the cell and the surface or indirectly by inhibiting cell adhesion, which induces then apoptosis. *In vivo*, application of pulsed currents to the electrodes kept the impedance lower compared to electrodes that stopped working during implantation, but histologically no difference was observed. We believe that integrating all electrodes on a single chip would allow for a better comparison of the impedance and histological data. This would, in addition, enable a more thorough investigation of the nearest cell layer by immunohistochemical staining. Although low level applied currents have been shown to be potent in influencing cell death and behavior *in vitro* and short-term *in vivo* responses, they appear to have little influence on long-term *in vivo* fibrotic reactions, possibly as a result of insufficient interactions between recruited host cells and functional groups on the implants. This interesting difference between *in vivo* and *in vitro* represents a pervasive problem in biomaterials science. The complexities of the wound healing dynamics *in vivo* are difficult to reproduce *in vitro*. We speculate that the relative ineffectiveness of surface functionality on long-term *in vivo* cellular responses may simply reflect insufficient cell surface interactions. Specifically, in an *in vitro* setting, cells are seeded directly on the working electrodes, and thus surface functionality has maximal effect on cellular responses. On the other hand, in an *in vivo* environment, the functional groups on nonporous implants can only interact with the first layer of cells which represent only a small portion of the surrounding cells/tissue. These relatively poor cell functional group interactions thus minimize the effect of surface functionality on cellular responses. In the next chapter we investigate the effects of currents on prokaryotes and how we can inhibit bacterial adhesion to urethral catheters.

7. Electrical current to prevent conditioning film and bacterial adhesion to urological stents

While in previous chapters the effects of electric currents to mammalian cells were presented, we investigate in this chapter the effects to bacteria. In form of a feasibility study we present a novel approach to prevent bacterial adhesion, colonization and encrustation with the *Proteus mirabilis* as a model bacteria for the most common bacteria to colonize urogenital catheters. If used only short term the newer generation catheters offer good comfort with minimal complications. In long-term, such catheters remain a significant clinical problem in urology, due to the high rate of bacterial colonization, infection and encrustation. They are commonly used in patients with obstructive disease to secure urine flow. Upon insertion of a prosthetic device in the urine tract, a conditioning film is formed on the device surface. The film is composed of proteins [131, 132], electrolytes, and other organic molecules [133] changing the devices surface properties and may provide receptor sites for bacterial adhesion [134]. Once the bacteria can adhere to the biofilm, cell division and colonization starts and may lead to large coherent bacterial biofilms [135]. This can then lead to super infection by opportunistic bacteria and to a rapid expanding infection often resistant to common antibiotics, especially if preceding antibiotic treatment has failed [136]. Biofilms offer an optimal environment for bacterial growth since there is no immunologic response and the penetration of antibiotics is poor. Many approaches to prevent biofilm formation and consecutive encrustation of urogenital catheters have been proposed with various outcomes [137–139]. Hydrophilic outer layers or coating with antibacterial agents such as rifampicin/minocycline or silver-ions, have been used to make urethral catheters less attractive to bacterial colonization [140]. While drug eluting catheters were able to reduce bacterial growth the formation of calcium-phosphate encrustation could not be inhibited [138, 139]. Further, the use of long term antibiotic agents is associated with the development of resistant microorganisms. Besides material research, other approaches tested were electric current to increase the efficacy of antibiotics against bacterial biofilms using high-frequency electric fields [141]. In 1969 Pareilleux and coworkers have first demonstrated the bactericidal effect of electric current [142]. An electrified drain to sterilize the field

of postoperative wound drainage were reported in 1993 [143,144]. A newer catheter device that would resist encrustation by *Proteus mirabilis* biofilms required relatively high current that could only be provided at the tip of the catheter where the fast corroding silver electrodes were located. This catheter increased the amount of silver ions in the urine and was able to decrease the rate of encrustation significantly [145]. In this research, another electricity based strategy was applied to overcome the problem of bacterial adherence and biofilm formation. We have shown in chapter 5 that eukaryotic cell migration and attachment can be prevented by applying small electric currents on metal and conductive metal oxide electrodes. Either local electrochemical reactions increasing H^+, HClO concentration and/or continuous altered layer deposition from culture medium have inhibited the adhesion and migration of eukaryotic cells. By applying alternating small current density on platinum electrodes, we could produce a self regenerative surface which actively removed the conditioning film significantly reducing bacterial adherence.

7.1. Quantification of film formation on platinum surfaces with applied currents

7.1.1. Experiments in artificial urine without bacteria

The film formation was studied and quantified under an applied current using EC-QCM-D technique (Section 3.2.2). The crystals were cleaned in 2% sodium dodecyl sulfate (SDS) for 30 min, rinsed with H_2O and blow dried with N_2. The surface was cleaned in a final step with UV/O_3 treatment (UVO Cleaner, Jelight Inc., USA) for 30 min. After mounting the crystal in the electrochemical cell (EC) of the QCM-D, artificial urine was pumped through the heated EC cell (37°C) and the selected current was applied by an Autolab potentiostat (Section 3.3.1). The formed layers from the QCM experiment were investigated in dry state with atomic force microscopy contact mode with the set point = 0.2 V (Section 3.2.3). The surface roughness was measured on 5 different areas with the dimension 2x2 μm, the R_{RMS} value was calculated and given with standard deviation in the corresponding AFM scan images. After the AFM measurement the crystals were immersed subsequently in 1 M HCl and 1 M NaOH to test the dissolution behavior of the formed films.

7.1.2. Results in artificial urine without bacteria

Different current densities were applied on the platinum coated QCM crystals and the amount of deposited material from artificial urine was monitored by the shift in the resonance frequency. Using the approximate values for the density (1000 kg/m^3) and the viscosity (0.001 kgm^{-1}s^{-1}) of artificial urine a fitting procedure based on the Voigt model was applied (Section 3.2.2) and the wet mass increment

of the adsorption process (0.1368 μgHz^{-1}cm^{-2}) was determined. Using this value the adsorbed wet mass of the formed layer was calculated from the observed changes in the resonance frequencies (Fig. 7.1, A). The same fitting procedure was used to estimate the layer formation for both, anodic and cathodic currents in figure 7.1, B, C. We applied an alternating current (period 4 s) density of I = 75 nA/mm^2 for 1 hour and observed a slightly decreasing baseline (to Δ_{max}wet mass = -6 μg/cm^2). Applying a current density of I = 320 nA/mm^2 (Δ_{max}wet mass $\leq$ 0.1 μg/cm^2), we did not see any significant adsorption. However, if a current density of I = 750 nA/mm^2 was applied the formation of a transient film with a peak wet mass Δ_{max}wet mass= 74 μg/cm^2 was observed after 18 min. Then, the film desorbed with the same rate constant as observed during formation. Applying a constant anodic current of I = 75 nA/mm^2 showed a continuous film formation reaching a plateau at a wet mass Δ_{max}wet mass= 27 μg/cm^2. Switching off the current (I = 0) did not change the layer thickness. Increasing the current density to I = 750 nA/mm^2 resulted in a continuous film formation with no plateau within the course of the experiment. Applying a cathodic current density of I = -75 nA/mm^2 showed no film formation, whereas a ten times higher current density displayed a slight film formation in the range of 6 μg/cm^2.

The platinum coated QCM crystals were gently rinsed with H_2O and blow dried with N_2 after the measurements. Macroscopically, the surfaces from the alternating and cathodic current experiment were clean, whereas the surface from the anodic current was covered with a bluish, oil-like film. Atomic force microscopy revealed the lack of deposited residues on the surface with applied alternating current densities I = 320 nA/mm^2 and I = 750 nA/mm^2, respectively (Fig. 7.2 B, C). The surface roughness after current became even lower than that of the new untreated, platinum coated crystals (Fig.7.2, A). In contrast, the platinum surface after anodic current treatment clearly showed the presence of a film that started to delaminate from the surface (Fig. 7.2, E) and wile scanning, a small fragment of the film was removed (Fig. 7.2, E, square insert) indicating weak film adhesion. The surface exposed after the film removal had a surface roughness of R_{RMS} = 1.9 nm. Due to the small delaminated area, only one 2x2 μm^2 region could be measured inside the hole. Therefore, no standard deviation is given. The roughness of the surrounding was also R_{RMS} = 1.9 nm $\pm$ 0.5. The film thickness was around (Fig. 7.2, F) 50 nm in dry state (cross-section, Fig. 7.2, G). After cathodic treatment, the surface showed an increase in surface roughness to R_{RMS}= 2.8 nm $\pm$ 1.4 nm (Fig. 7.2, D). After the AFM measurement, the QCM crystals were immersed in an acidic and a basic solution to test their dissolution behavior. Surprisingly, a very thin film seemed to tear off from the surface of the QCM crystal treated with alternating current I = 750 nA/mm^2 when immersed in acidic solution, while I = 320 nA/mm^2 did not show any delamination of a layer. The anodic bluish, oil-like film remained present in acidic solutions, while it was immediately dissolved in basic solutions. The cathodic QCM crystal showed no change in either of the solutions.

Among the different noble or non-corrosive materials that could be used as electrode, stainless steel, gold, silver and platinum are most common [146, 147]. For this feasibility study we decided to employ platinum electrodes because of their inert chemical characteristics [129]. The current density, rather than the potential, was kept constant to achieve a constant electrochemical product turnover and at different low current densities, where no cytotoxic effects are expected through the mucosa of the urinary tract. Applying an alternating current to Pt surfaces showed three different reactions on the adsorption of material leading to desorption of material at low current densities and no significant change at moderate current densities. Most surprising was to see that in artificial urine after an initial film formation, the film started to disappear without changing any parameters. It is difficult to find an explanation for the desorption behavior but weak interaction of the film with the surface might lead to partial delamination which is then averaged by the QCM and could be not observed in the AFM analysis due to the limited scanning area (100x100 μm^2). Tests with anodic currents showed a continuous layer formation on the platinum electrodes. Similar findings were made on indium tin oxide electrodes showing increased adsorption of a polymer under an applied positive potential as reported by Bearinger et al. [90]. Even continuous adsorption of poly-(L-Lysine) under positive potential was reported previously [107]. These results were counterintuitive since the molecule and the surface were both positively charged and the reason for this observation is not yet clear. They suggested that the molecules interact less strong with the surface when a potential is applied and therefore are more loosely structured, resulting in a higher mass per area adsorption. In addition, the production of HClO, due to Faradaic reactions might crosslink lysine side chains of proteins leading to film formation on the electrode surface and explain the observed continuous adsorption [148]. The AFM analysis of the platinum QCM crystals showed a slight increase of the surface roughness on the formed film and inside the delaminated area. But the highest surface roughness was measured after applying cathodic currents, which electrochemically induced high pH and might have caused precipitation of a smooth layer of calcium- and magnesium phosphate as indicated by the mass uptake in the QCM data at the higher current density The dissolution behavior was tested by dipping the formed layer on the QCM crystal in acidic or base solution, respectively. Surprisingly, a macroscopic barely visible film was delaminating from the alternating high current density QCM crystal when soaked in acidic solution but no delamination was observed in basic solution. The interaction force is weaker in the presence of protons, indicating that films must have been formed at basic conditions. This can be explained by the different standard reduction potentials necessary for the electrolysis of water at the anode (1.23 V vs. NHE) and cathode (-0.83 V vs. NHE) [100] and the symmetric current pulse applied. More hydroxide was formed at lower potentials than protons. As expected, the layer formed at anodic current was removed in basic solution.

7.2. Bacterial adhesion to platinum surfaces with applied currents

7.2.1. Experiments in artificial urine with bacteria

The substrate was designed to contain six equal electrodes inside the flow chamber (Fig. A.1) and produced as described in the methods and materials section 3.4.2. The flow chamber was custom-built, made of PMMA and designed for hosting the chip substrate (Fig. A.2) with the dimensions width = 10 mm, length = 15 mm and height = 0.1 mm. A peristaltic pump (IPC, ISMATEC, Switzerland) was used to maintain a constant flow rate of 200 μl / min. The flow chamber was placed in an incubator at 37°C during the experiment, while the artificial urine reservoir was placed outside of the incubator at room temperature. Selected currents were applied by the Autolab potentiostat (Section 3.3.1). Before the flow cell experiment, an aliquot of *Proteus mirabilis* was diluted in 500 ml sterile artificial urine (Section 3.7.3). The aliquot was made by scratching the bacteria from the culture media and suspending in 10 ml phosphate buffered saline (PBS) pH 7.4 and store in portions of 0.5 ml at -20°C. The cell viability and substrates were simultaneously stained and imaged as described in methods and materials section 3.5.4.

7.2.2. Results in artificial urine with bacteria

The experiment with *Proteus mirabilis* containing artificial urine was performed in a custom built flow cell (Fig. A.2) sealed onto a glass substrate with 6 equal platinum electrodes (Fig. A.1). Different currents (alternating current of I = 320 nA/mm^2, anodic currents of I = 75 nA/mm^2 and I = 750 nA/mm^2) were applied under continuous urine flow. After 6 days the substrate surface was stained for viable and dead cells (Fig. 7.3). *Proteus mirabilis* adhered to the control electrode with no current applied (Fig. 7.3, A). Most of the cells were found alive (green, FDA positive) and only a small fraction was dead (red, PI positive). On the electrode with alternating current of I = 320 nA/mm^2 only few dead bacteria and some impurities were observed. (Fig. 7.3, B) On the electrode with a small anodic current of I = 75 nA/mm^2 also only a few bacteria but a stronger green background signal was observed (Fig. 7.3, C). At higher current density (i.e. I = 750 nA/mm^2) a thick film started to delaminate from the electrode (Fig. 7.3, D). The presence of spots in the image indicates that some bacteria might be incorporated in the film but it was not possible to evaluate their vital status due to the strong fluorescence of the film. The platinum electrodes were not compromised by the applied currents after 6 days, since no corrosion artifacts were observed in transmission light microscopy (images not shown).

These findings led to the idea of using electric currents to prevent bacterial adhesion to urinary catheters either by the electrochemical products due to Faradaic

reactions and/or presenting a different surface to the bacteria than a conditioning film formed under normal conditions e.g. electrically formed film. We used *Proteus mirabilis* as a model because it is the most common bacteria to colonize catheter surfaces, to form extensive biofilms leading to encrustation [145,149]. Furthermore, *Proteus mirabilis* produces urease, which significantly increases the local pH levels by metabolizing urea to ammonia, inducing a precipitation of calcium- and magnesium-phosphate. The idea was tested in our custom built flow cell with constant artificial urine flow containing *Proteus mirabilis*. The results showed significantly decreased bacterial adhesion after 6 days in the case of applying alternating current (I = 320 nA/mm^2) and the expected layer formation at anodic currents, which started to delaminate at the highest current density. The film formation under applied electric currents is different compared to conditioning films formed under normal conditions. The likelihood of bacterial adhesion to such an altered surface might be much lower than under normal conditions and the electrochemical products H^+, OH^- generated on the electrode surface create unfavorable chemical gradient for bacterial colonization.Moreover, HClO is a strong oxidizer with bactericide properties in the vicinity of the electrode, where antibiotics usually cannot be applied in high enough concentrations [134] and H^+ is changing the urines pH to low values preventing calcium- and magnesium phosphate precipitation. We did not observe any microscopic crystals on the electrodes throughout the experimental time.

7.3. Summary

In conclusion, we were able to show that micro current applied to a conducting surface is effective in reducing bacterial growth in two ways. First, it can reduce the formation of the conditioning layer making bacterial adherence more difficult and secondly, by changing the microenvironment preventing bacterial adherence and growth. This research can lead a next generation of catheters with lower rates of biofim formation, infection and encrustation.

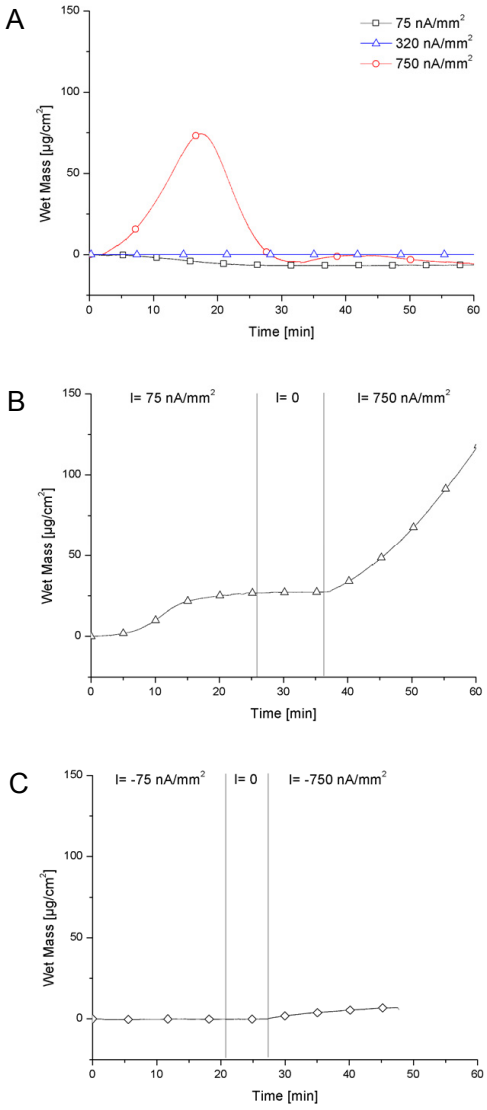

Figure 7.1.: Layer formation measured with QCM-D at different current densities applied to a platinum electrode in artificial urine. (A) An alternating current with a period of 4 s at I = 75 nA/mm^2 led to desorption of material. No significant adsorption/desorption was observed at I = 320 nA/mm^2 whereas I = 750 nA/mm^2 showed a film formation of a transient film with a peak at 18 min before the film desorbed with almost the same rate as it has been formed. (B) A constant anodic current of I = 75 nA/mm^2 showed a film formation reaching a plateau, while I = 750 nA/mm^2 showed a steeper and continuous film formation. (C) A constant cathodic current resulted in a slight film formation only at the higher current density of I = -750 nA/mm^2.

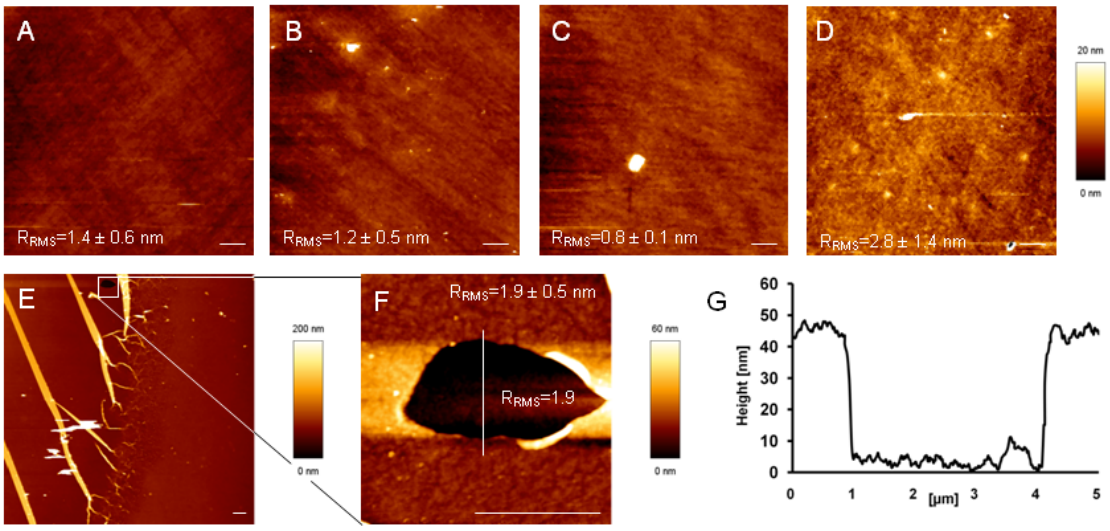

Figure 7.2.: Atomic force microscopy images of the platinum coated QCM crystal surface after applying different currents in artificial urine with the corresponding R_{RMS} value and dimension bar of 5 μm. (A) Surface of an untreated bare platinum crystal. (B) Surface after applying an alternating anodic current of I = 320 nA/mm^2, (C) of I = 75 and 750 nA/mm^2, (D) cathodic current I = 75 and 750 nA/mm^2. (E) The anodic current I = 75 and 750 nA/mm^2 induced film formation, which already started to delaminate, clearly visible in the image of the magnified square area. (F) The crack surface has the same R_{RMS} value as measured on the formed film. (G) The cross-section height profile of the crack inside the 50 nm thick film.

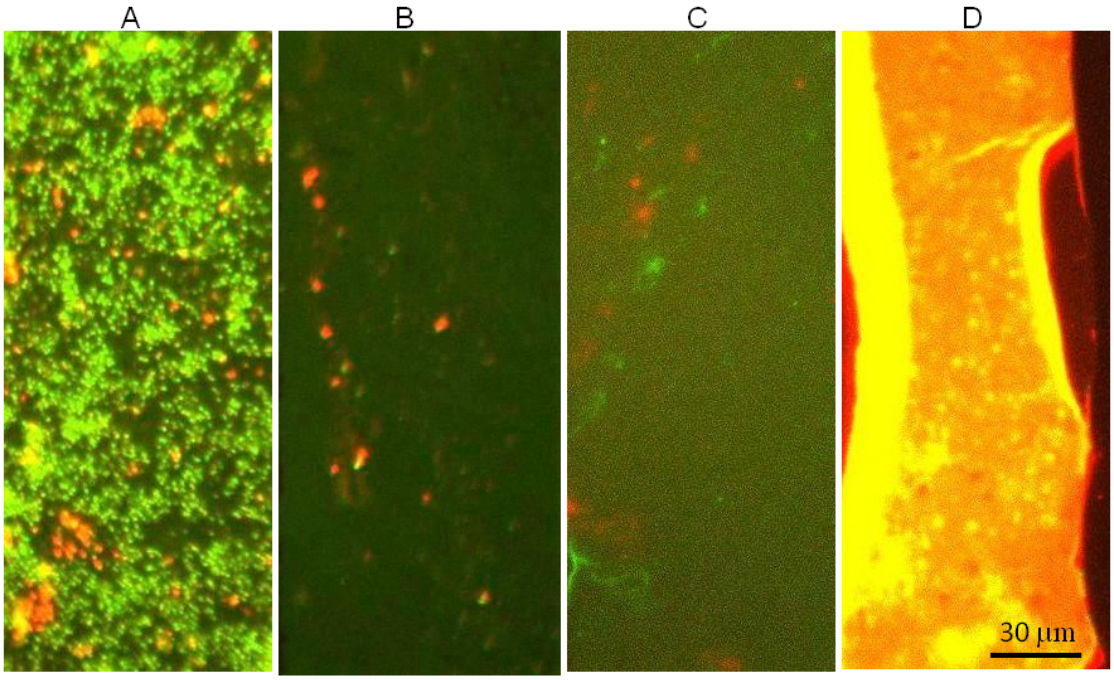

Figure 7.3.: Fluorescence microscopy images of 4 different platinum electrodes are shown after staining with FDA and PI to distinguish between viable (green) and dead (red) bacteria. Different current densities were applied to the platinum electrodes exposed for 6 days to artificial urine containing *Proteus mirabilis*. (A) No current I = 0 applied, (B) alternating current I = 320 nA/mm^2, (C) anodic current I = 75 nA/mm^2 (C) anodic current I = 750 nA/mm^2.

8. Conclusion and outlook

Almost everyone felt accidentally, the more or less painful effects of an electric shock and knows that electric currents are used in modern medicine to stimulate e.g heart muscles or brain, little is known about the effects on living cells at the electrode interface. In this thesis, we tried to understand and model the electrochemically induced reactions at an electrode and the found current density threshold value, which is needed to open pores in cells (Chapter 4) and could attribute this to local pH changes in the immediate vicinity of the electrodes. Such pH changes could be used to release drugs from pH sensitive polymers in sub micrometer drug delivery systems to address single cells or to control the adsorption / desorption of electrolytically adsorbed molecules. For example, in chapter 5, we controlled the adhesion and outgrowth of single neurons by the selective removal of a protein resistant polymer that inhibits cell adhesion when adsorbed to a surface. In the other experiment, the applied electric currents created locally an unfavorable conditions and inhibited cell migration onto electrodes, whereas the cells even in closed distance to the electrode were not harmed. We believe, that both approaches are key techniques for active cell guidance and the bottom-up engineering of of small neuron networks with well-defined topology providing an essential step towards understanding how the brain performs functions such as memory and learning. Moreover the techniques would allow the construction of cell co-cultures to study cell-cell interactions in a controlled environment or cell motility.

Experimental results in cell cultures can give only an idea how the tested currents will influence cells *in vivo*, so it was most interesting to see if the currents applied in our experiments will could also inhibit the cell adhesion in a rat model or not. We assumed that long pulsed currents might prevent the electrode from the host reaction of building a fibrous capsule around the electrode, since *in vitro* the cells formed only small adhesion patch and underwent apoptosis within 24 h (Chapter 6). *In vivo*, such apoptotic cells are removed by macrophages and subsequent intracellular digestion without provoking an inflammatory response. We observed no histological changes compared to control surfaces after 21 days of implantation. On the other hand, the impedance at high frequencies remained lower upon applying pulsed currents compared to electrodes that stopped working during implantation. Suggesting that our current density or applied voltage might be too small to produce instant effects, but enough to keep the adjacent cells in a constant reorganization either through apoptosis or via disintegration of the adherence junctions. Still, the question remains if the impedance could be kept low for far longer times, as needed

for permanent implants.

We have also studied the effects of currents on bacteria with the aim to develop a new type of urethral catheter that withstands conditioning film formation and bacterial colonization. Our feasibility study showed that by electrochemically changing the micro environment, the adhesion of the model bacteria *Proteus mirabilis* showed significantly decreased after 6 days in the case of applying alternating current. The findings were promising and could lead to the next generation of catheters with lower rates of biofilm formation, infection and encrustation in long-term use.

What sounds like science-fiction today and was the topic of literature and mainstream movies might become reality one day, when researcher can realize a permanent connection between an electric circuit and excitable living tissue without provoking a host reactions and prevent the electric interface from fibrous encapsulation. Only when long-term compatibility and functionality of the implant are guaranteed, brain and nerve implants to control robotic prosthesis or paralyzed limbs become reality. A first temporary, self-experiment was risked by Kevin Warwick [56] by implanting a microelectrode array into the median nerve of his left arm, allowing him the perception and the operation of an instrumented prosthetic hand remotely via internet or controlling the movement of a wheelchair. During his study, most of the electrodes became high impedance and therefore were not longer functional. Based on our results, the application of small pulsed currents could increase the lifetime of such electrode implants.

Another unsolved mystery is how the brain performs its basic tasks. Some researchers try to understand the brain from top-down approach and study the entire brain with functional Magnetic Resonance Imaging (fMRI). The brain is confronted with different tasks e.g. memorizing numbers, while the blood-oxygen level is measured as an indirect indicator for locally increased brain activity. Others, try the bottom-up approach by studying small neuron networks with random topology and try to deduce to the working principle of large neuron networks. The best approach might lie somewhere in between, the study of neuron networks with dozens of cells, but with controlled topology. Therefore it is crucial to have an active control over the cell adhesion, outgrowth and migration to create such networks, which leads us back to the topic of this thesis.

Curriculum vitae

Name:	Michael Gabi
Date of Birth:	July 1, 1976
Nationality:	Swiss, Citizen of Niederbipp (BE)
Present Address:	Hofwiesenstrasse 303 CH-8050 Zürich Switzerland

Education

02/2006 – 03/2010	PhD student at the Laboratory Biosensors and Bioelectronics, Swiss Federal Institute of Technology Zürich (ETH) .
05/2005 – 01/2006	Start PhD "Co-Extrusion of PZT Ceramic Materials", EMPA Dübendorf
10/2000 – 03/2005	Student of Material Science at ETH Zürich. Graduation with the degree Dipl. Werkstoff-Ing. ETH
08/1997 – 07/2000	Feusi Gymnasium in Bern (BE), half-day course, Matura Typus C (Mathematics and Nature Sciences)
08/1993 – 07/1996	Medical Laboratory Assistent, University Hospital Bern

Professional Experience

06/2009	Co-founder of Cytosurge, LLC
07/2003 – 10/2003	Internship, Yantai Wanhua Polyurethane Co.,Ltd., Beijing, China
01/2001 – 07/2002	Assistent, Metallic High Performance Materials, ETH Zurich
07/2000 – 09/2001	Laboratory Assistent, Phoenix International (former Anawa AG), Wangen bei Dübendorf
01/1997 – 04/2000	Laboratory Assistent part time (40%), Lindenhofspital Bern

Publications

"Force-controlled spatial manipulation of viable mammalian cells and microorganisms," Dörig P., Stiefel P., Behr P., Sarajlic E., Bijl D., **Gabi M.**, Vörös J., Vorholt J.A., Zambelli T. *in press, Applied Physics Letters*

"Electrical micro current to prevent conditioning film and bacterial adhesion to urological stents," **Gabi M.**, Hefermehl L., Lukic D., Eberli D., Vörös J. *accepted in Urological Research*

"Effects of small pulsed nano-currents on cell viability, in vitro and in vivo: Implications for biomedical electrodes," **Gabi M.**, Bullen M.E., Agarkova I., Schmidt D., Schoenauer R., Brokopp C., Emmert M.Y., Larmagnac A., Sannomiya T., Weber B., Wilhelm M.J., Vörös J., Hoerstrup S. P. *accepted in Biomaterials*

"Electrically controlling cell adhesion, growth and migration," **Gabi M.**, Larmagnac A., Schulte P., Vörös J. *Colloids and Surfaces B: Biointerfaces*, DOI: 10.1016 / j.colsurfb.2010.04.019

"FluidFM: Combining Atomic Force Microscopy and Nanofluidics in a Universal Liquid Delivery System for Single Cell Applications and Beyond," Meister, A; **Gabi M.**, Behr, P., Studer, P., Vörös, J., Niedermann, P., Bitterli, J., Polesel-Maris, J., Liley, M., Heinzelmann, H., Zambelli, T. *Nano Letters* , 2009, 9 (6), pp 25012507

"Nanoscale dispensing in liquid environment of streptavidin on a biotin-functionalized surface using hollow atomic force microscopy probes," Meister A., Polesel-Maris J., Niedermann P., Przybylskaa J., Studer P., **Gabi M.**, Behr P., Zambelli T., Liley M., Vörös J., Heinzelmann H. *Microelectronic Engineering* , Volume 86, Issues 4-6, April-June 2009, Pages 1481-1484

"Influence of applied currents on the viability of cells close to microelectrodes," **Gabi M.**, Sannomiya T., Larmagnac A., Puttaswamy M., Vörös J., *Integrative Biology* , 2009, 1, 108 - 115

"Enhanced optical waveguide light mode spectroscopy via detection of fluorophore absorbance," Halter M., **Gabi M.**, M. Textor, J. Vörös, H. M. Grandin, *Review of scientific instruments* , 77, 2006

Patents

"Method for spatially manipulating a microscopic object and device for conducting said method," **2010 Gabi M.**, Behr P., Dörig P., Zambelli T., Vorholt J., Stiefel P., Vörös J., Nr. 00249/10

"Device consisting of a channeled cantilever and a channeled probe holder," **2009**, **Gabi M.**, Zambelli T., Behr P. Vörös J., PCT/EP2009/005393

"Probe arrangement for electrophysiological analysis in an AFM," **2008**, Meister A., Polesel-Maris J., **Gabi M.**, Zambelli T., Vörös J., EP1990626 (A1), US20070928904P

Bibliography

[1] Colin D. McCaig, Ann M. Rajnicek, Bing Song, and Min Zhao. Controlling cell behavior electrically: Current views and future potential. *Physiological Reviews*, 85(3):943, 2005.

[2] Vladimir Hlady and Jos Buijs. Protein adsorption on solid surfaces. *Current Opinion in Biotechnology*, 7(1):72, 1996.

[3] Jort Robertus, Wesley R. Browne, and Ben L. Feringa. Dynamic control over cell adhesive properties using molecular-based surface engineering strategies. *Chemical Society Reviews*, 39(1):354.

[4] P. Harder, M. Grunze, R. Dahint, G. M. Whitesides, and P. E. Laibinis. Molecular conformation in oligo(ethylene glycol)-terminated self-assembled monolayers on gold and silver surfaces determines their ability to resist protein adsorption. *The Journal of Physical Chemistry B*, 102(2):426, 1998.

[5] C. S. Chen, M. Mrksich, S. Huang, G. M. Whitesides, and D. E. Ingber. Geometric control of cell life and death. *Science*, 276(5317):1425, 1997.

[6] K. J. Clemetson. Introduction: integrins, dynamic cell receptors. *Cellular and Molecular Life Sciences*, 54(6):499, 1998.

[7] R. O. Hynes. Integrins: versatility, modulation, and signaling in cell adhesion. *Cell*, 69(1):11, 1992.

[8] Ulrich Hersel, Claudia Dahmen, and Horst Kessler. Rgd modified polymers: biomaterials for stimulated cell adhesion and beyond. *Biomaterials*, 24(24):4385, 2003.

[9] K. Tashiro, G. C. Sephel, B. Weeks, M. Sasaki, G. R. Martin, H. K. Kleinman, and Y. Yamada. A synthetic peptide containing the ikvav sequence from the a chain of laminin mediates cell attachment, migration, and neurite outgrowth, 1989.

[10] Gabriel A. Silva, Catherine Czeisler, Krista L. Niece, Elia Beniash, Daniel A. Harrington, John A. Kessler, and Samuel I. Stupp. Selective differentiation of neural progenitor cells by high-epitope density nanofibers. *Science*, 303(5662):1352, 2004.

[11] S. M. Jacobsen, D. J. Stickler, H. L. T. Mobley, and M. E. Shirtliff. Complicated catheter-associated urinary tract infections due to escherichia coli and proteus mirabilis. *Clinical Microbiology Reviews*, 21(1):26, 2008.

[12] D. Falconnet, G. Csucs, M. H. Grandin, and M. Textor. Surface engineering approaches to micropattern surfaces for cell-based assays. *Biomaterials*, 27(16):3044, 2006.

[13] D. Kleinfeld, K. H. Kahler, and P. E. Hockberger. Controlled outgrowth of dissociated neurons on patterned substrates, 1988.

[14] S. Withers Ginger, D. James Conrad, E. Kingman Caroline, G. Craighead Harold, and A. Banker Gary. Effects of substrate geometry on growth cone behavior and axon branching, 2006.

[15] Jean-Francois Clemence, John P. Ranieri, Patrick Aebischer, and Hans Sigrist. Photoimmobilization of a bioactive laminin fragment and pattern-guided selective neuronal cell attachment. *Bioconjugate Chemistry*, 6(4):411, 1995.

[16] Mieko Matsuzawa, Paivi Liesi, and Wolfgang Knoll. Chemically modifying glass surfaces to study substratum-guided neurite outgrowth in culture. *Journal of Neuroscience Methods*, 69(2):189, 1996.

[17] Hsiu-Wen Chien, Tsung-Yao Chang, and Wei-Bor Tsai. Spatial control of cellular adhesion using photo-crosslinked micropatterned polyelectrolyte multilayer films. *Biomaterials*, 30(12):2209, 2009.

[18] J. Shaikh Mohammed, M. A. DeCoster, and M. J. McShane. Micropatterning of nanoengineered surfaces to study neuronal cell attachment in vitro. *Biomacromolecules*, 5(5):1745, 2004.

[19] O. Palyvoda, C. C. Chen, and G. W. Auner. Culturing neuron cells on electrode with self-assembly monolayer. *Biosensors and Bioelectronics*, 22(9-10):2346, 2007.

[20] T. W. Schneider, H. M. Schessler, K. M. Shaffer, J. M. Dumm, and L. A. Yonce. Surface patterning and adhesion of neuroblastoma x glioma (ng108-15) cells, 2001.

[21] J. M. Corey, B. C. Wheeler, and G. J. Brewer. Compliance of hippocampal neurons to patterned substrate networks, 1991.

[22] George M. Whitesides, Emanuele Ostuni, Shuichi Takayama, Xingyu Jiang, and Donald E. Ingber. Soft lithography in biology and biochemistry, 2001.

[23] A. Offenhausser, S. Bocker-Meffert, T. Decker, R. Helpenstein, P. Gasteier, J. Groll, M. Moller, A. Reska, S. Schafer, P. Schulte, and A. Vogt-Eisele. Microcontact printing of proteins for neuronal cell guidance. *Soft Matter*, 3(3):290, 2007.

[24] R. Sorkin, T. Gabay, P. Blinder, D. Baranes, E. Ben-Jacob, and Y. Hanein. Compact self-wiring in cultured neural networks. *Journal of Neural Engineering*, 3(2):95, 2006.

[25] C. D. James, A. J. H. Spence, N. M. Dowell-Mesfin, R. J. Hussain, K. L. Smith, H. G. Craighead, M. S. Isaacson, W. Shain, and J. N. Turner. Extracellular recordings from patterned neuronal networks using planar microelectrode arrays. *Biomedical Engineering, IEEE Transactions on*, 51(9):1640, 2004.

[26] Sang Beom Jun, Matthew R. Hynd, Natalie Dowell-Mesfin, Karen L. Smith, James N. Turner, William Shain, and Sung June Kim. Low-density neuronal networks cultured using patterned poly-l-lysine on microelectrode arrays. *Journal of Neuroscience Methods*, 160(2):317, 2007.

[27] I. H. Yang, C. C. Co, and C. C. Ho. Spatially controlled co-culture of neurons and glial cells. *Journal of Biomedical Materials Research Part A*, 75A(4):976, 2005.

[28] D. W. Branch, J. M. Corey, J. A. Weyhenmeyer, G. J. Brewer, and B. C. Wheeler. Microstamp patterns of biomolecules for high-resolution neuronal networks. *Medical Biological Engineering Computing*, 36(1):135, 1998.

[29] Daniel A. Heller, Veronika Garga, Keith J. Kelleher, Tai-Chou Lee, Sunil Mahbubani, Laura A. Sigworth, T. Randall Lee, and Michael A. Rea. Patterned networks of mouse hippocampal neurons on peptide-coated gold surfaces. *Biomaterials*, 26(8):883, 2005.

[30] B. F. Liu, J. Ma, E. J. Gao, Y. He, F. H. Cui, and Q. Y. Xu. Development of an artificial neuronal network with post-mitotic rat fetal hippocampal cells by polyethylenimine. *Biosensors and Bioelectronics*, 23(8):1221, 2008.

[31] A. Bernard, D. Fitzli, P. Sonderegger, E. Delamarche, B. Michel, H. R. Bosshard, and H. Biebuyck. Affinity capture of proteins from solution and their dissociation by contact printing. *Nature Biotechnology*, 19(9):866, 2001.

[32] M. Merz and P. Fromherz. Polyester microstructures for topographical control of outgrowth and synapse formation of snail neurons. *Advanced Materials*, 14(2):141, 2002.

[33] M. Merz and P. Fromherz. Silicon chip interfaced with a geometrically defined net of snail neurons. *Advanced Functional Materials*, 15(5):739, 2005.

[34] Jonathan Erickson, Angela Tooker, Y. C. Tai, and Jerome Pine. Caged neuron mea: A system for long-term investigation of cultured neural network connectivity. *Journal of Neuroscience Methods*, 175(1):1, 2008.

[35] A. M. P. Turner, N. Dowell, S. W. P. Turner, L. Kam, M. Isaacson, J. N. Turner, H. G. Craighead, and W. Shain. Attachment of astroglial cells to microfabricated pillar arrays of different geometries. *Journal of Biomedical Materials Research*, 51(3):430, 2000.

[36] N. M. Dowell-Mesfin, M. A. Abdul-Karim, A. M. P. Turner, S. Schanz, H. G. Craighead, B. Roysam, J. N. Turner, and W. Shain. Topographically modified surfaces affect orientation and growth of hippocampal neurons. *Journal of Neural Engineering*, 1(2):78, 2004.

[37] Anne M. Taylor, Mathew Blurton-Jones, Seog Woo Rhee, David H. Cribbs, Carl W. Cotman, and Noo Li Jeon. A microfluidic culture platform for cns axonal injury, regeneration and transport. *Nat Meth*, 2(8):599, 2005.

[38] L. J. Millet, M. E. Stewart, J. V. Sweedler, R. G. Nuzzo, and M. U. Gillette. Microfluidic devices for culturing primary mammalian neurons at low densities, 2007.

[39] L. E. Cheran, P. Benvenuto, and M. Thompson. Coupling of neurons with biosensor devices for detection of the properties of neuronal populations. *Chemical Society Reviews*, 37(6):1229, 2008.

[40] P. M. Mendes. Stimuli-responsive surfaces for bio-applications. *Chemical Society Reviews*, 37(11):2512, 2008.

[41] Offra Sarig-Nadir, Noga Livnat, Ruthy Zajdman, Shy Shoham, and Dror Seliktar. Laser photoablation of guidance microchannels into hydrogels directs cell growth in three dimensions. *Biophysical Journal*, 96(11):4743, 2009.

[42] Woon-Seok Yeo and Milan Mrksich. Electroactive self-assembled monolayers that permit orthogonal control over the adhesion of cells to patterned substrates. *Langmuir*, 22(25):10816, 2006.

[43] H. Kaji, T. Kawashima, and M. Nishizawa. Patterning cellular motility using an electrochemical technique and a geometrically confined environment. *Langmuir*, 22(25):10784, 2006.

[44] H. Kaji, M. Kanada, D. Oyamatsu, T. Matsue, and M. Nishizawa. Microelectrochemical approach to induce local cell adhesion and growth on substrates. *Langmuir*, 20(1):16, 2004.

[45] C. Zhao, I. Zawisza, M. Nullmeier, M. Burchardt, M. Taduble, I. Witte, and G. Wittstock. Microelectrochemical modulation of micropatterned cellular environments. *Langmuir*, 24(14):7605, 2008.

[46] C. Y. Fan, Y. C. Tung, S. Takayama, E. Meyhofer, and K. Kurabayashi. Electrically programmable surfaces for configurable patterning of cells. *Advanced Materials*, 20(8):1418, 2008.

[47] Y. Li, B. Yuan, H. Ji, D. Han, S. Q. Chen, F. Tian, and X. Y. Jiang. A method for patterning multiple types of cells by using electrochemical desorption of self-assembled monolayers within microfluidic channels. *Angewandte Chemie-International Edition*, 46(7):1094, 2007.

[48] Xingyu Jiang, Rosaria Ferrigno, Milan Mrksich, and George M. Whitesides. Electrochemical desorption of self-assembled monolayers noninvasively releases patterned cells from geometrical confinements. *Journal of the American Chemical Society*, 125(9):2366, 2003.

[49] Sunny S. Shah, Ji Youn Lee, Stanislav Verkhoturov, Nazgul Tuleuova, Emile A. Schweikert, Erlan Ramanculov, and Alexander Revzin. Exercising spatiotemporal control of cell attachment with optically transparent microelectrodes. *Langmuir*, 24(13):6837, 2008.

[50] Miriam Focaccia and Raffaella Simili. Luigi galvani, physician, surgeon, physicist: From animal electricity to electro-physiology. In *Brain, Mind and Medicine: Essays in Eighteenth-Century Neuroscience*, page 145. 2007.

[51] Rick McVenes and Ken Stokes. Implantable cardiac electrostimulation devices. In *Implantable Neural Prostheses 1*, page 221. 2009.

[52] P. Heiduschka and S. Thanos. Implantable bioelectronic interfaces for lost nerve functions. *Progress in Neurobiology*, 55(5):433, 1998.

[53] G. Miller. Neuropsychiatry. rewiring faulty circuits in the brain. *Science*, 323(5921):1554, 2009.

[54] D. D. Zhou and R. J. Greenberg. Microsensors and microbiosensors for retinal implants. *Frontiers in Bioscience*, 10:166, 2005.

[55] Mikhail A. Lebedev and Miguel A. L. Nicolelis. Brain-machine interfaces: past, present and future. *Trends in Neurosciences*, 29(9):536, 2006.

[56] Kevin Warwick, Mark Gasson, Benjamin Hutt, Iain Goodhew, Peter Kyberd, Brian Andrews, Peter Teddy, and Amjad Shad. The application of implant technology for cybernetic systems. *Archives of Neurology*, 60(10):1369, 2003.

[57] A. Branner, R. B. Stein, E. Fernandez, Y. Aoyagi, and R. A. Normann. Long-term stimulation and recording with a penetrating microelectrode array in cat sciatic nerve. *IEEE Transactions on Biomedical Engineering*, 51(1):146, 2004.

[58] R. V. Shannon. A model of safe levels for electrical stimulation. *Biomedical Engineering, IEEE Transactions on*, 39(4):424, 1992.

[59] D. B. McCreery, W. F. Agnew, T. G. H. Yuen, and L. Bullara. Charge density and charge per phase as cofactors in neural injury induced by electrical stimulation. *Biomedical Engineering, IEEE Transactions on*, 37(10):996, 1990.

[60] D. McCreery, W. Agnew, T. Yuen, and L. Bullara. Damage in peripheral nerve from continuous electrical stimulation: Comparison of two stimulus waveforms. *Medical and Biological Engineering and Computing*, 30(1):109, 1992.

[61] Daniel R. Merrill, Marom Bikson, and John G. R. Jefferys. Electrical stimulation of excitable tissue: design of efficacious and safe protocols. *Journal of Neuroscience Methods*, 141(2):171, 2005.

[62] D. T. Luttikhuizen, M. C. Harmsen, and M. J. Van Luyn. Cellular and molecular dynamics in the foreign body reaction. *Tissue Engineering*, 12(7):1955, 2006.

[63] B. D. Ratner and S. J. Bryant. Biomaterials: where we have been and where we are going. *Annu Rev Biomed Eng*, 6:41, 2004.

[64] Young-Tae Kim, Robert W. Hitchcock, Michael J. Bridge, and Patrick A. Tresco. Chronic response of adult rat brain tissue to implants anchored to the skull. *Biomaterials*, 25(12):2229, 2004.

[65] Y. Wickramasinghe, Y. Yang, and S. A. Spencer. Current problems and potential techniques in in vivo glucose monitoring. *Journal of Fluorescence*, 14(5):513, 2004.

[66] W. M. Grill and J. T. Mortimer. Electrical properties of implant encapsulation tissue. *Annals of Biomedical Engineering*, 22(1):23, 1994.

[67] A. S. Widge, M. Jeffries-El, X. Cui, C. F. Lagenaur, and Y. Matsuoka. Self-assembled monolayers of polythiophene conductive polymers improve biocompatibility and electrical impedance of neural electrodes. *Biosensors and Bioelectronics*, 22(8):1723, 2007.

[68] R. A. Green, N. H. Lovell, G. G. Wallace, and L. A. Poole-Warren. Conducting polymers for neural interfaces: challenges in developing an effective long-term implant. *Biomaterials*, 29(24-25):3393, 2008.

[69] V. S. Polikov, P. A. Tresco, and W. M. Reichert. Response of brain tissue to chronically implanted neural electrodes. *Journal of Neuroscience Methods*, 148(1):1, 2005.

[70] M. D. Johnson, K. J. Otto, and D. R. Kipke. Repeated voltage biasing improves unit recordings by reducing resistive tissue impedances. *IEEE Transactions on Neural Systems and Rehabilitation Engineering*, 13(2):160, 2005.

[71] Charles R. Keese, Joachim Wegener, Sarah R. Walker, and Ivar Giaever. Electrical wound-healing assay for cells in vitro. *Proceedings of the National Academy of Sciences of the United States of America*, 101(6):1554, 2004.

[72] M. O. Hengartner. The biochemistry of apoptosis. *Chemistry*, 101(102):145, 2002.

[73] J. Savill and V. Fadok. Corpse clearance defines the meaning of cell death. *NATURE-LONDON-*, page 784, 2000.

[74] A. Russo, M. Terrasi, V. Agnese, D. Santini, and V. Bazan. Apoptosis: a relevant tool for anticancer therapy. *Annals of Oncology*, 17(7), 2006.

[75] E. Nilsson, H. von Euler, J. Berendson, A. Thorne, P. Wersall, I. Naslund, A. S. Lagerstedt, K. Narfstrom, and J. M. Olsson. Electrochemical treatment of tumours. *Bioelectrochemistry*, 51(1):1, 2000.

[76] James C. Weaver and Yu A. Chizmadzhev. Theory of electroporation: A review. *Bioelectrochemistry and Bioenergetics*, 41(2):135, 1996.

[77] Anne-Rose Denet, Rita Vanbever, and Veronique Preat. Skin electroporation for transdermal and topical delivery. *Advanced Drug Delivery Reviews*, 56(5):659, 2004.

[78] F. Hofmann, H. Ohnimus, C. Scheller, W. Strupp, U. Zimmermann, and C. Jassoy. Electric field pulses can induce apoptosis. *Journal of Membrane Biology*, 169(2):103, 1999.

[79] J. Pinero, M. Lopez-Baena, T. Ortiz, and F. Cortes. Apoptotic and necrotic cell death are both induced by electroporation in hl60 human promyeloid leukaemia cells. *Apoptosis*, 2(3):330, 1997.

[80] N. Matsuki, T. Ishikawa, Y. Imai, and T. Yamaguchi. Low voltage pulses can induce apoptosis. *Cancer Letters*, 269(1):93, 2008.

[81] J. C. Ojingwa and R. R. Isseroff. Electrical stimulation of wound healing. *Journal of Investigative Dermatology*, 121(1):1, 2003.

[82] M. Kurokawa, H. Sakagami, F. Kokubu, H. Noda, M. Takeda, and M. Adachi. Induction of apoptotic cell death by direct-current treatment in human leukemic cell lines. *Journal of Cancer Research and Clinical Oncology*, 123(7):370, 1997.

[83] M. Wartenberg, N. Wirtz, A. Grob, W. Niedermeier, J. Hescheler, S. C. Peters, and H. Sauer. Direct current electrical fields induce apoptosis in oral mucosa cancer cells by nadph oxidase-derived reactive oxygen species. *Bioelectromagnetics*, 29(1):47, 2008.

[84] A. J. Bard and L. R. Faulkner. Electrochemical methods: fundamentals and applications, 2001. *Publisher: John Wiley Sons, Inc., Published in: New York*, page 15.

[85] T.W Swaddle. Inorganic chemistry an industrial and environmental perspective, 1997.

[86] F. Hook, J. Voros, M. Rodahl, R. Kurrat, P. Boni, J. J. Ramsden, M. Textor, N. D. Spencer, P. Tengvall, J. Gold, and B. Kasemo. A comparative study of protein adsorption on titanium oxide surfaces using in situ ellipsometry, optical waveguide lightmode spectroscopy, and quartz crystal microbalance/dissipation. *Colloids and Surfaces B: Biointerfaces*, 24(2):155, 2002.

[87] J. Voros, R. Graf, G. L. Kenausis, A. Bruinink, J. Mayer, M. Textor, E. Wintermantel, and N. D. Spencer. Feasibility study of an online toxicological sensor based on the optical waveguide technique. *Biosensors and Bioelectronics*, 15(9-10):423, 2000.

[88] J. Voros, J. J. Ramsden, G. Cscs, I. Szendro, S. M. De Paul, M. Textor, and N. D. Spencer. Optical grating coupler biosensors. *Biomaterials*, 23(17):3699, 2002.

[89] J. Benjamins, J. A. Feijter, M. T. A. Evans, D. E. Graham, and M. C. Phillips. Dynamic and static properties of proteins adsorbed at the air/water interface, 1975.

[90] J. P. Bearinger, J. Voros, J. A. Hubbell, and M. Textor. Electrochemical optical waveguide lightmode spectroscopy (ec-owls): A pilot study using evanescent-field optical sensing under voltage control to monitor polycationic polymer adsorption onto indium tin oxide (ito)-coated waveguide chips. *Biotechnology and Bioengineering*, 82(4):465, 2003.

[91] G. Sauerbrey. The use of quartz oscillators for weighing thin layers and for microweighing. *Z. Phys*, 155:206, 1959.

[92] M. V. Voinova, M. Rodahl, M. Jonson, and B. Kasemo. Viscoelastic acoustic response of layered polymer films at fluid-solid interfaces: Continuum mechanics approach. *Physica Scripta*, (5):391, 1999.

[93] Donald P. Griffith. Urease, the primary cause of infection-induced urinary stones. *Investigate Urology*, 13(5), 1976.

[94] H. E. Posch, M. J. P. Leiner, and O. S. Wolfbeis. Towards a gastric ph-sensor - an optrode for the ph 0-7 range. *Fresenius Zeitschrift Fur Analytische Chemie*, 334(2):162, 1989.

[95] T. C. McIlvaine. A buffer solution for colorimetric comparison. *Journal of Biological Chemistry*, 49(1):183, 1921.

[96] G. L. Kenausis, J. Voros, D. L. Elbert, N. P. Huang, R. Hofer, L. Ruiz-Taylor, M. Textor, J. A. Hubbell, and N. D. Spencer. Poly(l-lysine)-g-poly(ethylene glycol) layers on metal oxide surfaces: Attachment mechanism and effects of polymer architecture on resistance to protein adsorption. *Journal of Physical Chemistry B*, 104(14):3298, 2000.

[97] C. S. Tang, M. Dusseiller, S. Makohliso, M. Heuschkel, S. Sharma, B. Keller, and J. Voros. Dynamic, electronically switchable surfaces for membrane protein microarrays. *Analytical Chemistry*, 78(3):711, 2006.

[98] O. Guillaume-Gentil, Y. Akiyama, M. Schuler, C. Tang, M. Textor, M. Yamato, T. Okano, and J. Voros. Polyelectrolyte coatings with a potential for electronic control and cell sheet engineering. *Advanced Materials*, 20(3):560, 2008.

[99] John Crank. *The mathematics of diffusion*. Clarendon Press, Oxford, second edition, 1998.

[100] David R. Lide. *CRC handbook of chemistry and physics a ready-reference book of chemical and physical data*. CRC, Boca Raton, 88th edition, 2007.

[101] Peter Fromherz. Neuroelectronic interfacing: Semiconductor chips with ion channels, nerve cells, and brain. In Rainer Waser, editor, *Nanoelectronics and Information Technology*, page 781. 2003.

[102] A. T. Kuhn and C. Y. Chan. ph changes at near-electrode surfaces. *Journal of Applied Electrochemistry*, 13(2):189, 1983.

[103] T. M. Blattler, S. Pasche, M. Textor, and H. J. Griesser. High salt stability and protein resistance of poly(l-lysine)-g-poly(ethylene glycol) copolymers covalently immobilized via aldehyde plasma polymer interlayers on inorganic and polymeric substrates. *Langmuir*, 22(13):5760, 2006.

[104] F. Yamauchi, K. Kato, and H. Iwata. Spatially and temporally controlled gene transfer by electroporation into adherent cells on plasmid dna-loaded electrodes. *Nucleic Acids Res*, 32(22):e187, 2004.

[105] M. B. Grisham, M. M. Jefferson, D. F. Melton, and E. L. Thomas. Chlorination of endogenous amines by isolated neutrophils - ammonia-dependent bactericidal, cyto-toxic, and cytolytic activities of the chloramines. *Journal of Biological Chemistry*, 259(16):404, 1984.

[106] C. L. Hawkins, D. I. Pattison, and M. J. Davies. Hypochlorite-induced oxidation of amino acids, peptides and proteins. *Amino Acids*, 25(3):259, 2003.

[107] A. P. Ngankam and P. R. Van Tassel. Continuous polyelectrolyte adsorption under an applied electric potential. *Proceedings of the National Academy of Sciences of the United States of America*, 104(4):1140, 2007.

[108] F. Boulmedais, C. S. Tang, B. Keller, and J. Voros. Controlled electrodissolution of polyelectrolyte multilayers: A platform technology towards the surface-initiated delivery of drugs. *Advanced Functional Materials*, 16(1):63, 2006.

[109] Michelle A. Brusatori and Paul R. Van Tassel. Biosensing under an applied voltage using optical waveguide lightmode spectroscopy. *Biosensors and Bioelectronics*, 18(10):1269, 2003.

[110] K. Maurer, A. McShea, M. Strathmann, and K. Dill. The removal of the t-boc group by electrochemically generated acid and use of an addressable electrode array for peptide synthesis. *Journal of Combinatorial Chemistry*, 7(5):637, 2005.

[111] R. Shacham, D. Mandler, and D. Avnir. Electrochemically induced sol-gel deposition of zirconia thin films. *Chemistry-a European Journal*, 10(8):1936, 2004.

[112] F. Yamauchi, K. Kato, and H. Iwata. Layer-by-layer assembly of poly(ethyleneimine) and plasmid dna onto transparent indium-tin oxide electrodes for temporally and spatially specific gene transfer. *Langmuir*, 21(18):8360, 2005.

[113] Astrid A. Prinz and Peter Fromherz. Electrical synapses by guided growth of cultured neurons from the snail ¡small¿lymnaea stagnalis¡/small¿. *Biological Cybernetics*, 82(4):L1, 2000.

[114] Junji Fukuda, Ali Khademhosseini, Judy Yeh, George Eng, Jianjun Cheng, Omid C. Farokhzad, and Robert Langer. Micropatterned cell co-cultures using layer-by-layer deposition of extracellular matrix components. *Biomaterials*, 27(8):1479, 2006.

[115] A. Khademhosseini, L. Ferreira, J. Blumling, J. Yeh, J. M. Karp, J. Fukuda, and R. Langer. Co-culture of human embryonic stem cells with murine embryonic fibroblasts on microwell-patterned substrates. *Biomaterials*, 27(36):5968, 2006.

[116] Tao Xu, Joyce Jin, Cassie Gregory, James J. Hickman, and Thomas Boland. Inkjet printing of viable mammalian cells. *Biomaterials*, 26(1):93, 2005.

[117] Tao Xu, Cassie A. Gregory, Peter Molnar, Xiaofeng Cui, Sahil Jalota, Sarit B. Bhaduri, and Thomas Boland. Viability and electrophysiology of neural cell structures generated by the inkjet printing method. *Biomaterials*, 27(19):3580, 2006.

[118] J. Nilsson, M. Evander, B. Hammarstrom, and T. Laurell. Review of cell and particle trapping in microfluidic systems. *Analytica Chimica Acta*, 649(2):141, 2009.

[119] Hu Zhang and Kuo-Kang Liu. Optical tweezers for single cells. *Journal of The Royal Society Interface*, 5(24):671, 2008.

[120] Yasuhiro Tanaka, Tatsuro Endo, Yasuko Yanagida, and Takeshi Hatsuzawa. Design and fabrication of a dielectrophoresis-based cell-positioning and cell-culture device for construction of cell networks. *Microchemical Journal*, 91(2):232, 2009.

[121] J. Tanner Nevill, Ryan Cooper, Megan Dueck, David N. Breslauer, and Luke P. Lee. Integrated microfluidic cell culture and lysis on a chip. *Lab on a Chip*, 7(12):1689, 2007.

[122] G. Hacker. The morphology of apoptosis. *Cell and Tissue Research*, 301(1):5, 2000.

[123] A. M. Magro, A. D. Magro, C. Cunningham, and M. R. Miller. Down-regulation of vinculin upon mk886-induced apoptosis in ln18 glioblastoma cells. *Neoplasma*, 54(6):517, 2007.

[124] J. O. Gjorret, D. Fabian, B. Avery, and P. Maddox-Hyttel. Active caspase-3 and ultrastructural evidence of apoptosis in spontaneous and induced cell death in bovine in vitro produced pre-implantation embryos. *Molecular Reproduction and Development*, 74(8):961, 2007.

[125] Dieter Braun and Peter Fromherz. Fluorescence interferometry of neuronal cell adhesion on microstructured silicon. *Physical Review Letters*, 81(23):5241, 1998.

[126] K. Burridge and P. Mangeat. An interaction between vinculin and talin. *Nature*, 308(5961):744, 1984.

[127] E. Ruoslahti and B. Obrink. Common principles in cell adhesion. *Experimental Cell Research*, 227(1):1, 1996.

[128] R. P. Englert and E. Shacter. Distinct modes of cell death induced by different reactive oxygen species: amino acyl chloramines mediate hypochlorous acid-induced apoptosis. *Journal of Biological Chemistry*, 277(23):20518, 2002.

[129] Brge Thing Mortensen and Jrgen Bojsen. Evidence for growth inhibition by platinum electrodes at low current levels. *Journal of Biomedical Engineering*, 4(2):103, 1982.

[130] D. Brynn Hibbert, Karyn Weitzner, Bruce Tabor, and Paul Carter. Mass changes and dissolution of platinum during electrical stimulation in artificial perilymph solution. *Biomaterials*, 21(21):2177, 2000.

[131] B. K. Canales, L. A. Higgins, T. Markowski, L. Anderson, Q. A. Li, and M. Monga. Presence of five conditioning film proteins are highly associated with early stent encrustation. *Journal of Endourology*.

[132] M. Santin, A. Motta, S. P. Denyer, and M. Cannas. Effect of the urine conditioning film on ureteral stent encrustation and characterization of its protein composition. *Biomaterials*, 20(13):1245, 1999.

[133] A. G. Gristina. Biomaterial-centered infection: microbial adhesion versus tissue integration. *Science*, 237(4822):1588, 1987.

[134] Peter Tenke, Claus R. Riedl, Gwennan Ll Jones, Gareth J. Williams, David Stickler, and Elisabeth Nagy. Bacterial biofilm formation on urologic devices and heparin coating as preventive strategy. *International Journal of Antimicrobial Agents*, 23(Supplement 1):67, 2004.

[135] J. D. Denstedt, Tima Wollin, and G. Reid. Biomaterials used in urology: Current issues of biocompatibility, infection, and encrustation*. *Journal of Endourology*, 12(6):493, 1998.

[136] J. D. Denstedt and P. A. Cadieux. Eliminating biofilm from ureteral stents: the holy grail. *Current opinion in urology*, 19(2):205, 2009.

[137] G. J. Williams and D. J. Stickler. Some observations on the diffusion of antimicrobial agents through the retention balloons of foley catheters. *The Journal of Urology*, 178(2):697, 2007.

[138] Jorg Michael Schierholz, Nedim Yucel, A. F. E. Rump, Joseph Beuth, and Gerhard Pulverer. Antiinfective and encrustation-inhibiting materials–myth and facts. *International Journal of Antimicrobial Agents*, 19(6):511, 2002.

[139] D. J. Stickler and S. D. Morgan. Observations on the development of the crystalline bacterial biofilms that encrust and block foley catheters. *Journal of Hospital Infection*, 69(4):350, 2008.

[140] C. P. Davis, S. Weinberg, M. D. Anderson, G. M. Rao, and M. M. Warren. Effects of microamperage, medium, and bacterial concentration on iontophoretic killing of bacteria in fluid. *Antimicrobial Agents Chemotherapy*, 33(4):442, 1989.

[141] M. Giladi, Y. Porat, A. Blatt, Y. Wasserman, E. D. Kirson, E. Dekel, and Y. Palti. Microbial growth inhibition by alternating electric fields. *Antimicrobial Agents and Chemotherapy*, 52(10):3517, 2008.

[142] A. Pareilleux and N. Sicard. Lethal effects of electric current on escherichia coli. *Applied and Environmental Microbiology*, 19(3):421, 1970.

[143] A. Shafik. The electrified catheter. *World Journal of Urology*, 11(3):183, 1993.

[144] A. Shafik. The electrified drain. a new device for sterilizing the field of drainage. *International Surgery*, 78(4):357, 1993.

[145] A. Chakravarti, S. Gangodawila, M. J. Long, N. S. Morris, A. R. E. Blacklock, and D. J. Stickler. An electrified catheter to resist encrustation by proteus mirabilis biofilm. *Journal of Urology*, 174(3):1129, 2005.

[146] C. P. Davis, M. D. Anderson, S. Hoskins, and M. M. Warren. Electrode and bacterial survival with iontophoresis in synthetic urine. *The Journal of urology*, 147(5):1310, 1992.

[147] J. A. Spadaro, T. J. Berger, S. D. Barranco, S. E. Chapin, and R. O. Becker. Antibacterial effects of silver electrodes with weak direct-current. *Antimicrobial Agents and Chemotherapy*, 6(5):637, 1974.

[148] Michael Gabi, Takumi Sannomiya, Alexandre Larmagnac, Manjunath Puttaswamy, and Janos Voros. Influence of applied currents on the viability of cells close to microelectrodes. *Integrative Biology*, 1(1):108, 2009.

[149] D. J. Stickler. Bacterial biofilms in patients with indwelling urinary catheters. *Nature Clinical Practice Urology*, 5(11):598, 2008.

Appendices

A. Constructions and designs

In this section the different poylmer mask layout are schematically shown for the substrate used for pH measurement and bacterial adhesion experiments after applying different currents (A.1) as well as the schematics of the used flow cell (A.2). The neurochip was assembled of different parts, all produced using photolithograpic methods. Illustrated are the polymer mask design for the printed circuit board (A.3), the chromium mask designs for the ITO electrode etching and 3D SU8 structure (A.4). The indium tin oxide microelectrode arrays (MEA) MEA60 ITO 200 without SU8 were purchased from Ayanda Biosystem (Switzerland) (A.6). The ITO MEA consisted of a glass substrate with a 8 x 8 matrix array of 60 indium tin oxide electrodes (minus four corner electrodes) (A.7). The chip was rinsed with pure ethanol and MilliQ water, blow dried with N_2 and plasma treated for 2 min prior to the experiment. The chip was mounted into a MEA interface 1060 without amplifiers purchased from Multi Channel Systems (Germany). The interface was modified in a way that a platinum wire is always in contact with the solution in the chip and a PMMA disc covers the top part of the MEA chip interface to avoid contamination and drying out of the cell culture media

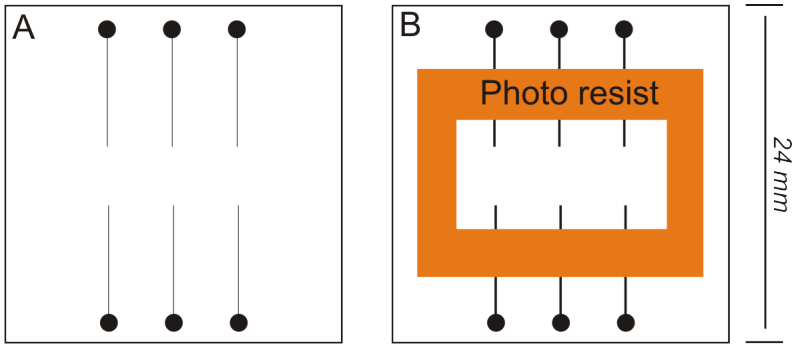

Figure A.1.: The glass substrate with 6 equal electrodes on a microscopy cover slide(A) Indium tin oxide electrodes width=30μm. (B) Platinum electrodes for bacterial adhesion experiment width=1 mm with an insulating photo resist structure to present a defined 0.2 x 1 mm Pt surface to the artificial urine.

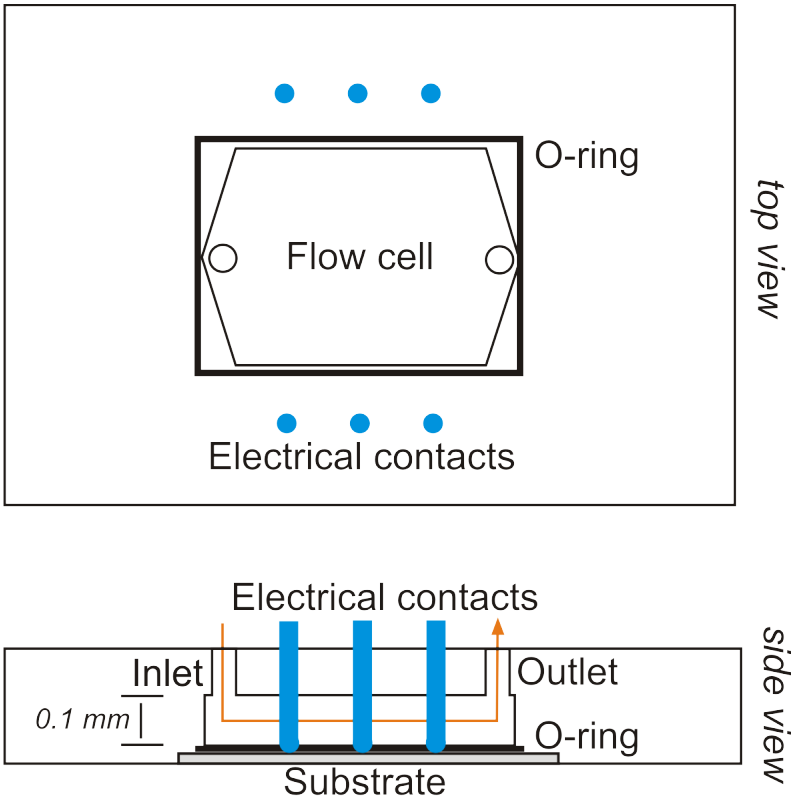

Figure A.2.: Schematics of the custom made flow cell used for pH measurement and bacterial adhesion tests. Electrical spring contacts allow a simple and reliable connection to the substrate electrodes. Silicone o-ring prevents any leakage and short-circuit between the electrodes. The flow of the pH indicator solution or the artificial urine, respectively is indicated by the red arrow.

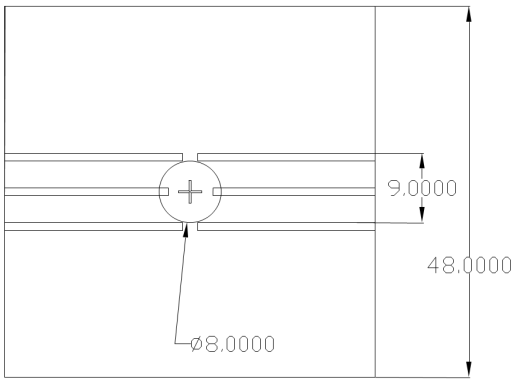

Figure A.3.: Schematics of the printed circuit board used as a stable base for the neurochip, including copper leads connecting the ITO electrodes on the neurochip

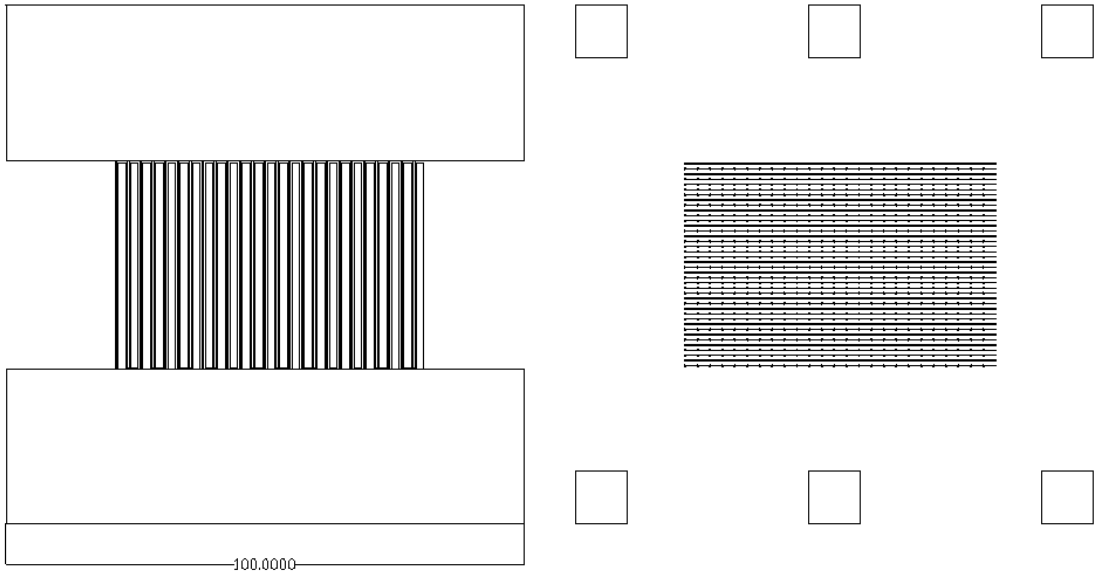

Figure A.4.: Schematics of the chromium mask to microfabricate the ITO electrodes (left) and the supporting SU8 photo resist structure with landing spot and lateral neurite outgrowth channels (right).

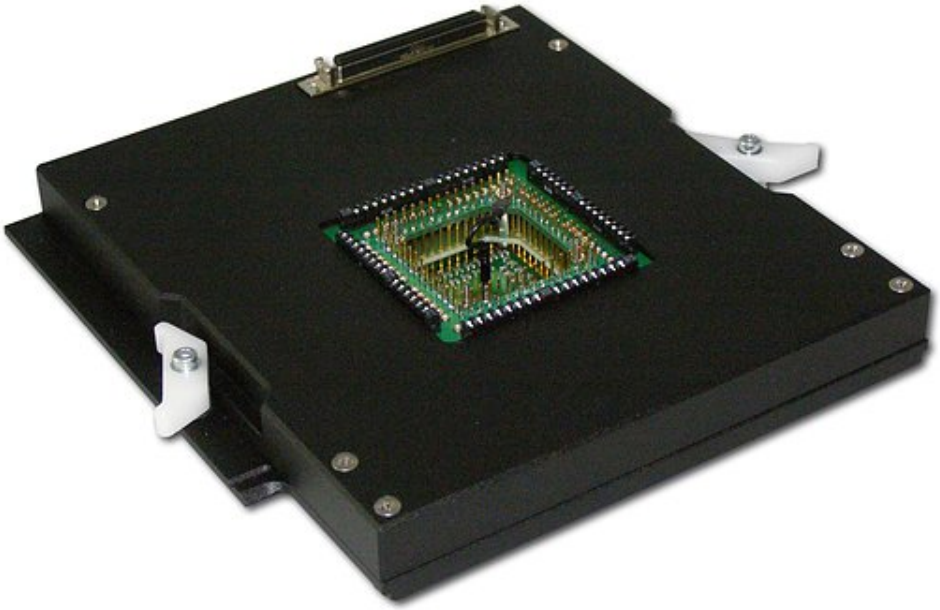

Figure A.5.: MEA chip interface 1060 without amplifiers. A SCSI interface enables the connection of single electrodes on a MEA60 chip.

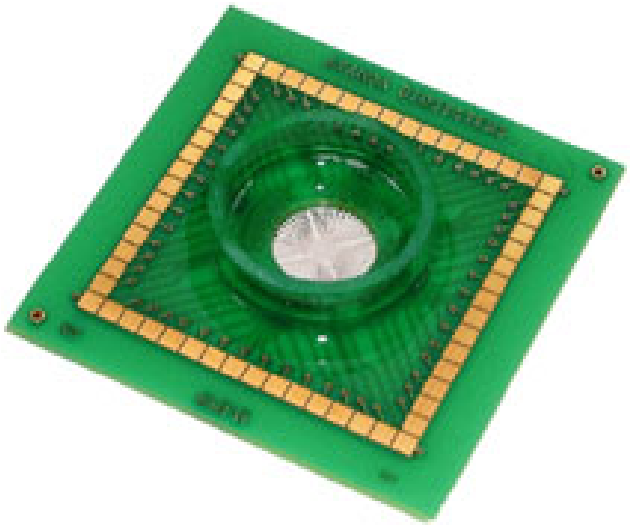

Figure A.6.: The Ayanda biochip was attached onto the printed circuit board by means of screen-printing. The gold contacts surrounding the petri-dish enabled electronic addressing of the individual ITO microelectrodes.

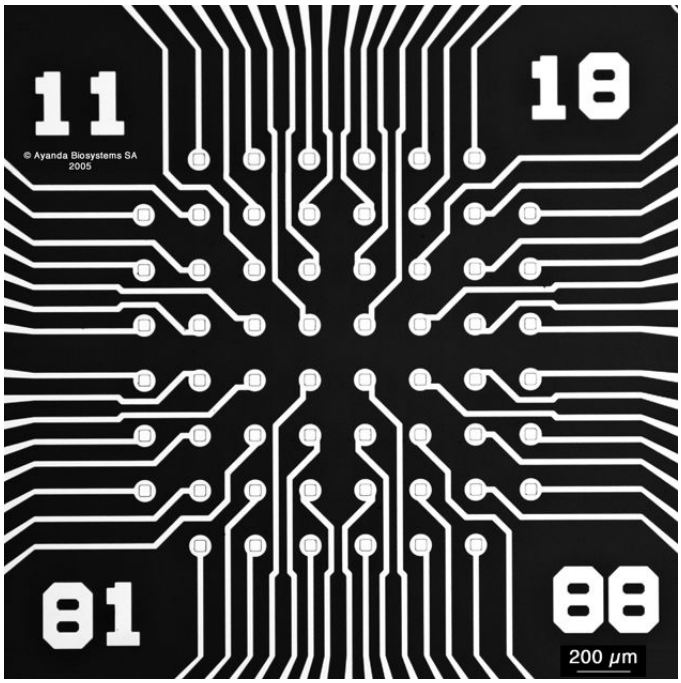

Figure A.7.: The indium tin oxide microarray consists of 60 ITO microelectrodes (8 x 8 matrix without corner electrodes) with 40 μm x 40 μm square electrodes with an interspacing of 200 μm (centre to centre).